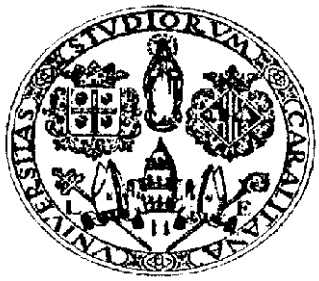

Università degli Studi di Cagliari

# DOTTORATO DI RICERCA

FISICA DELLA MATERIA

Ciclo XXV

# TITOLO TESI

ATOMISTIC INVESTIGATION OF STRUCTURE AND OPTOELECTRONIC PROPERTIES OF HYBRID POLYMER/ZnO INTERFACES

Settore scientifico disciplinare di afferenza

FIS 03 / FISICA DELLA MATERIA


Presentata da: MARIA ILENIA SABA

Coordinatore Dottorato Prof. PAOLO RUGGERONE

Tutor/Relatori Prof. LUCIANO COLOMBO
Dr. ALESSANDRO MATTONI


Esame finale anno accademico 2011 – 2012

Maria Ilenia Saba: *Atomistic investigation of structure and optoelectronic properties of hybrid polymer/ZnO interfaces*

SUPERVISORS:
Prof. Luciano Colombo
Dr. Alessandro Mattoni

LOCATION:
Cagliari

# ACKNOWLEDGMENTS

I would like to thank my supervisors, Prof. Luciano Colombo and Dr. Alessandro Mattoni, for their patient guidance, advice and encouragement during these three years.

I thank Claudio Melis and Giuliano Malloci, for the help and support they have given me, and Claudia Caddeo for all the useful scientific discussions.

Furthermore, I am indebted with Claudio for his work on P3HT and with Giuseppe Mattioli for his DFT calculations on ZnPcs.

A special thank goes also to Matteo Dessalvi and Giovanna Masala for the technical and administrative support, respectively.

An important acknowledgment is due to the Italian Institute of Technology (IIT), under Seed Project "POLYPHEMO" for funding my thesis work, to Regione Autonoma della Sardegna under Project "Nanomateriali ecocompatibili per celle fotovoltaiche a stato solido di nuova generazione" (CRP-24978) L.R.7/2007 and to CASPUR (now incorporated into CINECA) for the computing resources.

Grazie ai miei genitori, che mi hanno permesso di arrivare fin qui, e a mio marito Stefano, che mi ha aiutato a riprendere coraggio lungo il cammino.

Infine, un sentito ringraziamento a tutti gli amici e colleghi che mi hanno supportato (e sopportato) in questi anni, primo fra tutti l'indispensabile Gigi, ai colleghi di ufficio passati e presenti e alle mie compagne di viaggio Gabriella, Sara e Arianna.

# ABSTRACT

Hybrid interfaces are attracting increasing interest for photovoltaic applications due to their low cost of production compared to traditional silicon-based systems and easy processability. This is the case of polymer/metal oxide systems. In particular, hybrid P3HT/ZnO can be considered as a possible alternative to organic solar cells because, by replacing the organic electron acceptor with the inorganic metal oxide it is, in principle, possible to improve the stability as well as the durability of the system.

In this thesis, by means of a combination of large scale molecular dynamics simulations and *ab initio* methods, we study at the atomic scale the interface between the polymer P3HT and the ZnO crystalline surface.

We investigate the structure and morphology of the polymer at the interface at low and room temperature, we characterize in detail the polymer disorder close to the ZnO surface and we discuss the implications of this disorder on transport properties. Furthermore, we investigate the possible presence of residual molecules of solvent at the interface after the synthesis process, that can affect the properties of the interface.

A novel strategy to improve the polymer/metal oxide interface is proposed and investigated. Specifically, we study the deposition and assembling of zinc phthalocyanine molecules on ZnO and we investigate the modification of the P3HT/ZnO interface, induced by the use of a ZnPc optically active molecular interlayer. The structure and morphology of the ZnO/ZnPc/P3HT system, studied by molecular dynamics simulations, are used as starting point for DFT calculations. We discuss the electronic and optical properties of this ternary system reporting indications of an improvement in hybrid photovoltaic devices due to the hindering of the charge recombination and a better exploitation of the solar spectrum.

This kind of architecture, theoretically designed by a multiscale predictive modeling in the present thesis, is an

example of a novel class of systems whose performances are currently under experimental investigation.

## SOMMARIO


Attualmente le interfacce ibride richiamano un notevole interesse per applicazioni fotovoltaiche grazie al loro minore costo di produzione rispetto alla tradizionale tecnologia a base-silicio e alla loro facilità di produzione. Questo è il caso dei sistemi polimero/metalossido. In particolare, l'interfaccia ibrida P3HT/ZnO può a tutti gli effetti essere considerata come una possibile alternativa alle celle solari organiche, poiché permette di utilizzare il componente inorganico al posto dell'accettore di elettroni organico, migliorando la stabilità e la durata del sistema.

In questo lavoro studiamo alla scala atomica l'interfaccia tra il polimero P3HT e la superficie cristallina di ZnO, utilizzando una combinazione di simulazioni di dinamica molecolare e metodi da principi primi.

Studieremo la morfologia e la struttura del polimero all'interfaccia a bassa temperatura e a temperatura ambiente, e caratterizzeremo in dettaglio il disordine del polimero vicino alla superficie. Le implicazioni di tale disordine sulle proprietà di trasporto del polimero verranno discusse, così come la possibile presenza all'interfaccia, dopo la sintesi, di molecole residue di solvente, che possono avere un ruolo nelle proprietà dell'interfaccia.

Una nuova strategia atta a migliorare le prestazioni dell'interfaccia polimero/metalossido verrà proposta e investigata. Nello specifico, studieremo la deposizione e l'aggregazione di zinco ftalocianine sullo ZnO e investigheremo le modificazioni all'interfaccia con il P3HT indotte dall'uso di un tale layer molecolare otticamente attivo. Le informazioni sulla struttura e morfologia del sistema ZnO/ZnPc/P3HT, ottenute tramite la dinamica moleculare, verranno utilizzate come punto di partenza per calcoli DFT. In particolare, discuteremo le proprietà elettroniche e ottiche di questo sistema ternario, e vedremo come la presenza di tale interlayer può risultare utile nel migliorare le interfacce ibride fotovoltaiche poiché può ostacolare la ricombinazione tra le cariche ed è in grado di sfruttare meglio lo spettro solare.

Questo tipo di architettura, progettata tramite una modellizzazione teorica, è un esempio di una nuova classe di sistemi, le cui prestazioni sono al momento studiate sperimentalmente.

# CONTENTS

# LIST OF FIGURES

## LIST OF TABLES

# 1 INTRODUCTION

## Contents



### 1.1 HYBRID INTERFACES FOR PHOTOVOLTAICS

Photovoltaics represents a promising and challenging field of inquiry in the area of renewable and sustainable energies and the search of new and more efficient photovoltaics materials is a constant stimulus for materials science.

The photovoltaic market is currently dominated by the silicon based materials, that provide high power conversion efficiencies (PCE) (up to 25% [7]) due to the excellent charge transport properties and stability of high pure silicon [8]. The drawback of this trend consists in the high costs and in the environmental impact needed to produce high quality material.

An alternative to the conventional silicon systems are the organic solar cells [9, 10]. Organic materials have been taken into account as possible candidates in replacement of silicon due to the discovery of organic molecules and polymers having both conducting and semiconductor properties [8]. Polymer conductivity is due to conjugation, that is the alternation of single and double bonds between the carbon atoms [11]. Every bond contains a localised $\sigma$ bond which forms a strong chemical bond and every double bond contains a less strongly localised and weaker $\pi$ bond. In these conditions two delocalized energy bands are formed, the bonding $\pi$ and the antibonding $\pi^*$ orbitals, also called the highest occupied molecular orbital (HOMO) and the lowest unoccupied molecular orbital (LUMO), respectively. HOMO and LUMO are separated by a bandgap (typically

1-3 eV) and the transition between these two levels can be excited by light in the visible spectrum [12]. These properties make conjugated organics very interesting for photovoltaic applications.

Furthermore organic semiconductors, having very high absorption coefficients and quite good charge carrier mobility (0.1 $cm^2\ V^{-1}\ s^{-1}$ for the P3HT polymer [13]) allow the use of very thin films but still absorbing a sufficient portion of the solar spectrum [8]. The reduction in material used, the low cost manufacturing techniques and the possibility to produce devices using solution phase methods, such as ink jet printing or various roll to roll techniques [14, 15], make organic materials very attractive to the photovoltaic market [8] . Moreover their properties and designs can be finely tuned and optimized based on materials versatility, solution-based processing, and mechanical flexibility [16].

Bilayer solar cells are composed by two layers of materials; the one with higher electron affinity and ionization potential has the role of electron acceptor, while the other material is the electron donor and acts also as light absorber (see Figure 1.1). An important example of electron acceptor material is the buckminsterfullerene ($C_{60}$) [17], while the semiconductor polymer most used as donor is the poly(3-hexylthiophene) (P3HT). The device is completed by two electrodes, a semi-transparent anode (e.g. the indium-tin-oxide, ITO) and a metallic cathod having a low work function value (e.g. aluminum, lithium) [18]. Special contact layers have been developed to obtain better performance, in particular the PEDOT:PSS polymer [19] has shown good results used as anode due to its high transparency in the visible range, high mechanical flexibility, and excellent thermal stability [20].

Unlike the silicon case, where the light absorption results in the formation of free electrons and holes, in organic systems electrons are promoted from the HOMO to the LUMO, resulting in the formation of excitons composed by a hole and an electron strongly bound together (usually with a binding energy between 0.5 and 1 eV [12]); a large potential gradient is then necessary to drive the charge carriers away from the dissociating interface [21], resulting in a lower efficiency of the system. For an ef-

ficient electron-hole separation, the junction between the two materials must be of the type-II (staggered), for which the HOMO and LUMO positions decrease in energy when moving from the donor to the acceptor (see Figure 1.1). Excitons can recombine efficiently unless they diffuse and separate at the interface within their lifetime. In order to achieve high performance bilayers, trasport must be efficient in comparison to recombination mechanisms, such as luminescence or non-radiative recombination. For the majority of molecules, the exciton lifetime is in the order of nanoseconds while the distance that an exciton can cross is limited to about 10 nm [10]. This means that only the excitons formed within this distance from the interface can contribute to charge separation.

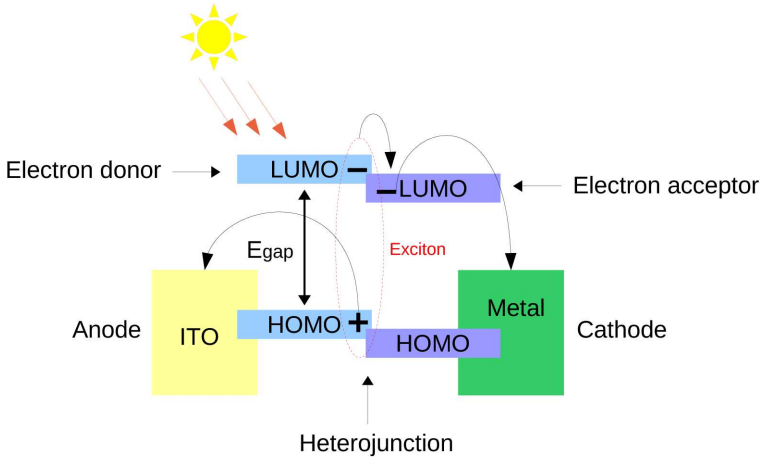


HOMO: Highest Occupied Molecular Orbital (valence band)

LUMO: Lowest Unccupied Molecular Orbital (conduction band)

**Figure 1.1.:** *Working principle of an organic bilayer solar cell.*

The simple bilayer can be replaced by a more complex bulk heterojunction architecture. In this kind of solar cell the donor and acceptor components interpenetrate one another, giving an interface not planar but spatially distributed [12]. This feature makes possible to partially overcome the limitation due to the diffusion length of excitons since the large surface-to-volume ratio makes possible to collect at the interface a larger fraction of excitons.

Unfortunately, the disadvantages are represented by the difficult separation of the charges due to the increased dis-

order in such a complicated morphology and by the possibility for the trapped charge carriers to recombine with the mobile ones before proceeding to the contacts [12].

The generation and collection of carriers contribute to the short-circuit current ($I_{SC}$), that is the maximum current from a solar cell, occurring at zero voltage. This parameter, together with the open-circuit voltage ($V_{OC}$) and the fill factor, determines the energy conversion efficiency of a solar cell [10]. $I_{SC}$ depends on the area of the solar cell, the number of photons, the spectrum of the incident light and the optical properties of the solar cell. The open-circuit voltage is the maximum voltage available from a solar cell, and this occurs at zero current. For ohmic contacts $V_{OC}$ is governed by the energy levels of HOMO and LUMO of donor and acceptor [10], therefore, it can be raised by carefully positioning these levels [10]. Obviously, when the device works at either open circuit or short circuit conditions the power $P = VI$ is zero.

Another important quantity is the fill factor (FF), defined as the ratio between the maximum output power ($P_{max}$) and $V_{OC}I_{SC}$ (see Figure 1.2). Since the efficiency is given by the ratio between the power output $P_{out}$ and the solar power input $P_{in}$, it can be expressed in terms of FF by the relation $\eta = \frac{V_{OC} I_{SC} FF}{P_{in}}$.

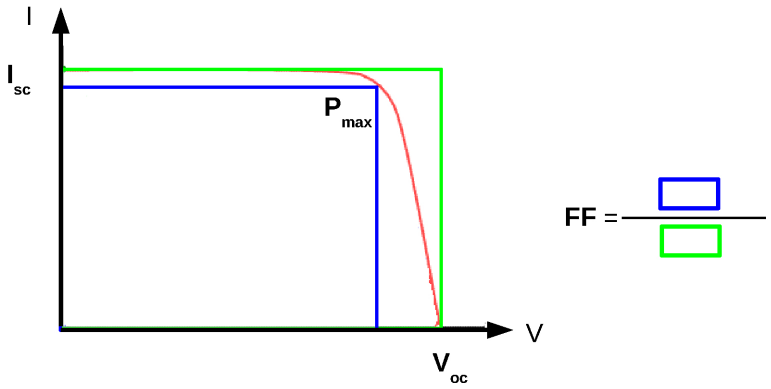


**Figure 1.2.:** *Characteristic voltage-current of a solar cell.*

An important problem limiting the efficiency of the organic solar cell is related to the collection of the photons over the whole solar spectrum. To obtain good efficiencies the absorption spectrum of the photoactive material must match the solar emission spectrum and it must be suffi-

ciently thick to absorb all the incident light [21]. By lowering the band gap of the organic material it is possible to harvest a greater part of the sunlight increasing, in principle, the photocurrent. To this aim, in these last years the scientific community began to investigate organic solar cells composed by a new type of low band gap organic polymers, such as the poly-thienothiophene-benzodithiophene (PTB) that have the same sequence of alternating thieno[3,4-b] thiophene (TT) and benzodithiophene (BDT) monomer units attached with different side groups [22]. In particular PTB7 in combination with the $PC_{71}BM$ fullerene had produced efficiencies as high as 8% [23].

The record efficiency for the organic solar cells (12%) is currently held by a type of multi-junction solar cell (tandem cell), that provide an effective way to harvest a broader spectrum of solar radiation by combining several p-n junctions tuned to a different wavelength of light [24]. In Figure 1.3 are reported the conversion efficiency for the different kind of solar cells, and it can be observed the considerable improvement obtained by the organic photovoltaic (OPV) in the last ten years.

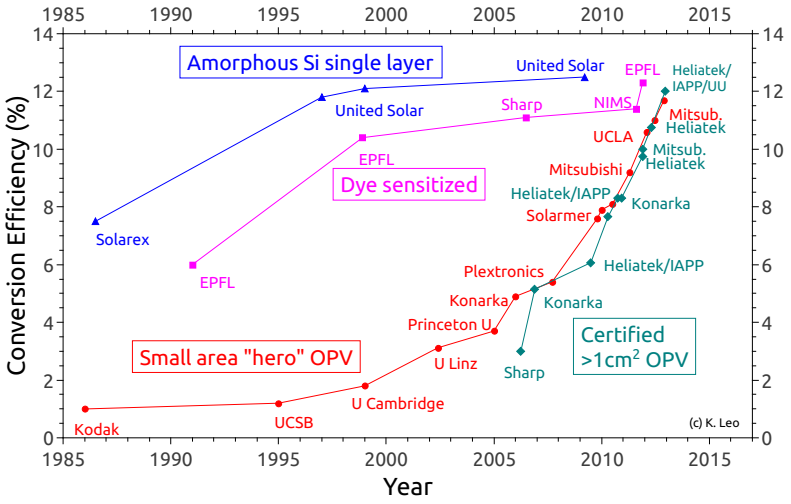


**Figure 1.3.:** *Organic photovoltaic efficiencies from* 1986 *to* 2013 *(figure from [1]).*

As for the lifetime of the organic solar cells, the principal problem is related to the degradation of active layer and electrode materials due to water and oxygen. Even with the most accurate protection there are several degradation

processes that need to be eliminated to ensure stability [21, 25].

A possible and widely studied alternative to the organic solar cells are the hybrid organic-inorganic systems, composed by an organic conductive polymer and a cheap and environmental friendly inorganic semiconductor, such as a metal oxide. These systems are of great interest since they combine the peculiar properties of the two kinds of materials involved at a relatively low cost of production. In particular, they allow to join the tailorable properties and the flexibility of the organic polymers with the thermal and mechanical stability and the good transport properties of the inorganic materials [26].

In hybrid solar cells the role of the acceptor is played by the inorganic material, such as $TiO_2$ or ZnO, while the conductive polymer (tipically the P3HT) has the role of electron donor. Such systems are promising for their technological impact though, until now, the highest achieved efficiency for a ZnO/P3HT binary system is as low as 2% [27]. This result is not comparable with that obtained by fully organic devices and a clear motivation for this poor behavior is still missing.

However, not all hybrid technologies have poor efficiencies. The most competitive hybrid systems are represented by the liquid-solid dye sensitized solar cell (DSSC), where an organic dye is used for absorption of light and injection of the photoexcited electron into a $TiO_2$ mesoporous substrate. In 1991, Grätzel proposed a DSSC with 7% efficiency using a Ru-complex dye, a nanocrystalline $TiO_2$ mesoporous film [28] and liquid redox electrolyte (usually the $I_3^-/I^-$ system) acting as hole transporting layer [29].

In the solid state dye-sensitized solar cell (SDSSC) [30, 31], the holes are transferred to a solid organic hole transporter material (HTM) infiltrated within the substrate[32]. High efficiency for the SDDSC systems has been obtained using as HTM the spiro-OMETAD[30], a small optically inactive molecule forming a solid amorphous network. Also in this case the principal limit in the improvement of the solid state DSSC efficiencies is the high rate of recombination between photogenerated electrons and the holes [32]. By replacing the HTM with a polarisable liquid electrolyte, the screening of the holes makes possible to reach efficien-

cies as high as 12%[33], though reducing the long-term stability of the cell[34, 31]. Novel strategies are to use inorganic interlayers (e.g. $ZrO_2$ [35]) to separate the HTM and the metal oxide. The recombination can be reduced but in this case the charge injection to the semiconductor is affected too.

Hybrid polymer/metal oxide systems can be seen as a particular case of SDSSC, where the polymer combines the functions of light-absorption and charge transport in the same material so replacing both the dye and the hole transporting material [21]. Although, in principle, there are no reasons for which the solid state technology should have poorer efficiencies than in DSSCs, however polymer/metal oxide efficiencies are still well below DSSC.

The above scenario and the technological potential of polymer/metal oxide systems require the optimization of the polymer, a better fundamental understanding and accurate theoretical investigations.

## 1.2 PHYSICAL FACTORS RELEVANT FOR PHOTOCONVERSION AT HYBRID INTERFACES

Hybrid interfaces belong to the class of excitonic solar cells where the photoconversion is controlled by three main processes:

1. Absorption of light and exciton generation,
2. charge separation by exciton dissociation at the interface,
3. charge transport and collection.

All the above physical mechanisms are rooted on the atomic scale of the active layer of the solar cells and their efficient operation require to control the molecular features of the system (such as the position of HOMO and LUMO, the band alignment and so on).

The technological overview of the previous section suggests that there are many open problems in hybrid systems that require a better theoretical investigation. These are overview below.

The importance of the polymer morphology and organization at the hybrid interfaces has been discussed in several recent studies. For example the low efficiency of the ZnO/polymer hybrids has been attributed to the formation of an amorphous area of polymer within the first nanometers from the ZnO surface [36, 37]. The polymer disorder is expected to be detrimental for the efficiency of the system. Firstly, it is known that in the amorphous polymer the lifetime of the carriers is shorter [36] than in the crystalline phase. Secondly, the electronic orbital levels of P3HT and, in turn, the charge transfer efficiency depend on the polymer crystallinity [38, 36]. Finally, better light absorption [39, 40] and transport properties are found in crystalline polymer phase.

A second fundamental issue of the hybrid interface is related to the electronic energy level alignment at the interface, that controls electronic properties such as charge injection, separation and so on. Specifically they depend on the position of components HOMO and LUMO, which also define their band gap [10]. In particular the LUMO level of the acceptor must be located below the LUMO level of the donor and the same for the HOMOs, in the type-II (staggered) configuration described above. However the LUMO level of the acceptor should not be too low because, for example, the open circuit voltage of a photovoltaic cell is proportional to the energy difference between the LUMO level of the acceptor and the HOMO level of the donor [41]. The tuning of these level is a key issue and the determination of the HOMO and LUMO position is very important. Typically, a compromise between $V_{OC}$ and charge injection must be reached, since $\eta \sim V_{OC} I_{SC}$.

The possibility of a large interface area and an effective contact, critically depends on the adhesion between the organic and inorganic components at the interface. Adhesion is the result of several interatomic force actions including covalent, electrostatic, and dispersive ones, the relevance of each contribution depending both on the chemistry and on the atomic-scale structural properties [42]. In the case of hybrid polymer/metal oxide systems, strong electrostatic interactions occur between the ions of the surface and the partially charged atoms in the polymers due to the ionicity of the metal oxide. However, in general, the polymer does

not form covalent bonds with the inorganic material. In addition, when the surface is nanostructured, the adhesion of the polymer is affected furthermore by the local morphology and a dependence on the surface curvature is possible [42].

As for the optical absorption of the hybrid systems, it is totally due to the optically active polymer, being the metal oxide wide band gap materials (3.4 eV in the case of ZnO [43]) optically transparent.

There is a strong dependence of the polymer absorption on the substrate where the polymer is deposited. For example, Lloyd et al. [36] found a different behavior for the P3HT on glass, on ZnO or on hexadecanethiol ($C_{16}SH$) modified ZnO. When deposited on glass, P3HT displays two intrachain $\pi\pi^*$ absorption peaks and a low energy shoulder associated with interchain interactions that are typical of highly crystalline polymers. Conversely, P3HT deposited on ZnO loses its crystalline organization showing a blue shift in the peak of the UV-Vis absorption spectrum and no long wavelength absorption shoulder. The blue shift of P3HT can be reduced and the low-energy shoulder can be recovered by the introduction of a $C_{16}SH$ layer at the interface between the polymer and the ZnO [36].

In the direction of better controlling the polymer at the interface, the use of interlayers between the polymer and the metal oxide has been recently investigated [44, 45, 46, 47]. The motivations for using interlayers are the increase of the polymer/substrate compatibility, the better charge transport, the reduced charge recombination, the tunability of the work function of the substrate obtained by the introduction of molecular dipoles and the enlargment of the light absorbed spectrum.

For example, surface modifications of $TiO_2$ nanorods by pyridine derivatives before mixing with the polymer, can be used to improve the device performance by enhancing charge separation, improving compatibility, and strongly suppressing back recombination [44].

It has been observed that the external quantum efficiency of a P3HT/ZnO solar cell can be tripled by inserting a monolayer of PCBA between the two components [45]. In fact, the presence of PCBA induces an interfacial dipole

and shifts up the LUMO level of P3HT relative to the conduction band edge of ZnO [45] .

Molecular dipoles have been found to modify also the titania surface in $TiO_2$/P3HT interfaces [46]. In fact, a series of para-substituted benzoic acids with varying dipoles and a series of multiply substituted benzene carboxylic acids can be used to cause a band edge shift in titania, resulting in a change in the open-circuit voltage [46].

Recently also small molecules, such as catechol or isonicotinic acid, have attracted attention as interface modifiers in hybrid systems [48, 49, 50]. In particular, catechol is used as an anchoring group for organic and organometallic dyes due its efficient adsorption onto $TiO_2$ via formation of a strong adsorbate-substrate complex [48, 49, 50] and for the type II hybrid junction that forms in combination with $TiO_2$ [48, 51, 52].

Again, an ordered molecular layer composed by the 4-mercaptopyridine (4-MP) molecules between a $TiO_2$ surface and a polymer, has produced an overall efficiency of the device which overcomes the 1% limit [47]. The presence of the oriented molecular layer, triggered by selective interactions with the $TiO_2$ surface, drives local ordering smoothing the otherwise abrupt interface. This result shows the importance of molecular interactions and local morphology in hybrid interfaces and their implications on charge separation and recombination [47].

High-efficient solid-state hybrid polymer/metal oxide solar cells have been obtained by depositing $Sb_2S_3$ as sensitizer and P3HT as hole conductor and light absorber on a titania surface [53]. This cells exhibit good conversion efficiency and it is highly stable in air, even without encapsulation [53].

The most important modification of the hybrid polymer/metal oxide interface is obtained by inserting optically active interlayers that can contribute to light absorption and injection. This is possible by using dyes and sensitizers to load the metal oxide surface. Most of the information in this approach comes from the research on DSSCs. Among the most widely used sensitizers there are the porphyrins, partly because the their structure synthetically analogue of chlorophyll [54]. Porphyrins have extensively conjugated $\pi$ systems, are favourable to fast electron transfer to an ac-

ceptor and absorb light well in the blue and moderately in the green regions of the visible spectrum with high molar absorption coefficients [54]. In particular, one of the most notable efficiency improvements in hybrid devices (3%) has been obtained by using porphyrins as dyes in a P3HT/$TiO_2$ system [55].

A cheap and environmentally friendly alternative are phthalocyanines (Pcs) [4, 54]. They are characterized by an intensive absorption in the far-red IR region, by an excellent chemical, light, and thermal stability, a long exciton diffusion length (8-68 nm for CuPc) and a high hole conductivity ($2 \times 10^{-5}$ to $5 \times 10^{-4}$ $cm^2$ $V^{-1}$ $s^{-1}$) [54]. Furthermore, phthalocyanines offer flexibility in their optical and electronic properties through synthetic modifications, including the addition of functional groups to the molecule perimeter [54]. The structure of these molecules is characterized by one or more macrocyclic ligands carrying clouds of delocalized electrons and by a central metal or group [4]. Since Pc aggregates have electrochemical, spectroscopic, photophysical, and conductive properties different from those of the corresponding monomers [4], the abilty to understand and drive their assembling is crucial in order to obtain interlayers that really improve the hybrid interfaces.

Finally, another problem to deal with in the hybrid systems production is the influence of the solvent used for spin coating. It was found that the change of solvent (from chloroform to xylene) yields one to two orders of magnitude improvement in a photovoltaic $TiO_2$/P3HT cell efficiency [56]. Furthermore, fabrication conditions, as well as the inorganic nanoparticles concentration, can significantly affect the morphology of the interface and the device performance [56]. The presence of residual solvent at the interface can affect the polymer deposition, acting as an interface modifiers just as in the cases discusses above [6].

## 1.3 THEORETICAL MODELING OF HYBRID INTERFACES

The previous discussion clearly shows the need of a thorough theoretical study of hybrid interfaces in order to clarify their properties and the effects of interlayers in improving their photoconversion performances.

To this aim, in this work we adopt a combination of atomic scale methods including Model Potential Molecular Dynamics (MPMD) and Density Functional Theory (DFT) calculations.

MPMD [57, 58, 59] is a computational technique that consists in calculating the classical trajectories of a set of interacting atoms representing the material of interest by solving the Newton's Equation of motions ($\mathbf{F} = m\mathbf{a}$). Forces are derived from a suitable model potential of the atomic positions that is calibrated in such a way to reproduce a set of physical properties of the material (see Appendix A).

The relatively low computational workload associated to MPMD, allows to obtain predictive informations regarding thermodinamics and microcrystalline evolution over the 10 ns timescale of systems as large as 10 nm.

Furthermore, the molecular dynamics approach makes possible to easily take into account long range dispersive interactions, by using simple Lennard-Jones type potential.

The accurate description of interatomic forces in hybrids is however challenging. A general model potential for the hybrid system is not available, but there are reliable potentials for the organic and inorganic phases separately. Organic polymers can be described by means of the "tried and true" Amber force field [60], while in the case of metal oxide the modeling is slightly more complicated. In particular, the ZnO description must take into account its partially ionic and partially covalent nature [61]. A simple and succesfull solution is the use of pair interactions consisting of a short-range part (usually a Buckingham interaction [62]) and long-range Coulombic terms employing fixed charges. This method, however, does not take into account the charge redistribution around a defect or at the surface [61]. In the more advanced shell-model description [61, 63, 64], the electronic polarizability is included adding an additional charged site to each ion connected via a spring [65]. The shell models however do not properly describe the covalent character of ZnO [61], problem that can be aided by using higher-order terms in the many-body expansion [66], or by neglecting also the ionic character and using a bond-order potential [67], but these solutions have also several drawbacks [61], including larger computational costs. Finally, the reactive force field (ReaxFF)

[61, 68, 69] is also a bond-order interaction model consisting of the two-body, three-body and four-body short-range interaction terms. It allows the redistribution of charges, can simulate the breaking and reforming of bonds and can reproduce the structures and mechanical properties of condensed phases [61, 68, 69] but requires an high computational cost and a very large number of fitting parameters.

In the present work, we focus on a planar ideally perfect metal oxide surface (ZnO), so that the role of defects and its evolution is not critical. Furthermore, at room temperature most of the microstructure evolution is expected in the softer organic part of the system. For these reasons we adopt the simple combination of Buckingham plus long range Coulombic interatomic potentials, that represents a compromise between computational cost and accuracy, the reliability of this description being confirmed by several works [70, 71].

As for the electronic properties of PV interfaces, the DFT approach provides very good choice but its heavier computational cost limits the analysis to small portions of the MPMD generated system. The DFT method require some care in the choice of exchange-correlation functional used. In particular, both the LDA [72] and the GGA [73] functionals suffer from the problem of the underestimation of the band gap for the semiconductors (including the ZnO) [74]. This problem can be partially overcome by using the LDA+U approach [75, 76] or hybrid funcionals (such as the B3LYP [77, 78]). This latter, however, severely increases the computational cost.

## 1.4 AIMS AND OUTLINE OF THIS THESIS

The aim of this thesis work is to generate realistic atomistic model for hybrid interfaces and supply informations for their design and optimization.

In particular, a major emphasis will be given to the morphological aspects of the investigated systems, while the electronic properties will be addressed mainly as a review contribution framed in a more general discussion.

The understanding of the hybrid interface requires first of all the study of the polymer alone, its structure and mechanisms of aggregation. Therefore, the first chapter of

this work concerns the P3HT polymer studied as single molecule (dimer and oligomer) and aggregated bulk including crystalline and nanocrystalline phases. Its crystalline properties and self assembling mechanism are investigated, as well as the structure of polymer nanoclusters.

Hybrid interfaces between the polymer and the ZnO metal oxide are studied in detail in the second chapter. The P3HT/ZnO system is investigated by using different models, depending on the deposition kinetics of the polymer on the surface. The polymer order at the interface is analyzed by a structural analysis based on the calculated structure factor and the charges mobility is estimated by using an effective method based on the Marcus theory giving effective transport properties of the generated models.

In the third chapter, in order to investigate the effects of optically active and self assembled interlayers, we study the ternary system P3HT/ZnPc/ZnO composed by the double interface ZnPc/ZnO and ZnPc/P3HT. This model of ternary interface, created by MPMD methods, is the starting point for an ab initio study of its optical and electronic properties. These P3HT/ZnPc/ZnO interface turns out to be very promising in the design of new systems able to operate in the whole extent of the solar light and allowing a direct anchoring of the dye to the substrate.

Finally, the fourth chapter takes into account the presence of optically inactive layers on ZnO. In particular we consider the case of the solvent tetrahydrofuran (THF) and we study the possible effects due to the presence of such an organic interlayer in polymer/metal oxide systems. The interaction between the THF molecule and the ZnO is studied, as well as the formation of a wetting layer from the liquid phase at room temperature.

A brief introduction to the methods used in this work is done in the section section A.3.

# 2

# P3HT - POLY(3-HEXYLTHIOPHENE)

## Contents



## 2.1 MECHANISM OF ASSEMBLING AND MORPHOLOGY OF CRYSTALLINE P3HT

The understanding of the polymer/metal oxide hybrid interface, final aim of this thesis, requires first of all the study of the polymeric phase alone. In particular we investigate the polymer assembling and the mechanisms of molecular aggregation, in order to eventually characterize both infinite periodic bulks (perfectly crystalline or quasi-ordered) and finite size nanocrystalline structures.

One of the most commonly used conjugated polymer in photovoltaics is the Poly-3-hexylthiophene (P3HT) since its unique combination of high carrier mobility (0.1 $cm^2\ V^{-1}\ s^{-1}$), high environmental/thermal stability, electrical conductivity, processability, and synthetic versatility [79].

When cast from solvents into thin films, P3HT self-assembles into oriented microcrystalline domains (10-60 nm) and amorphous regions [80, 81, 2]. The crystallinity of P3HT thin films has considerable impact on the charge-carrier mobility [82] but it is still under debate. The detailed knowledge of the polymer structure is therefore fundamental and requires an in-depth investigation.

A single P3HT is formed by a $\pi$-conjugated thiophene backbone and alkyl side chains (Figure 2.1). The unit cell of dimension (7.75 Å) contains two consecutive thiophenes rings and two hexyl side chains each formed by six $sp^3$

carbon atoms. Its regioregular form is the most used variant of the polymer in optolectronic applications [83].

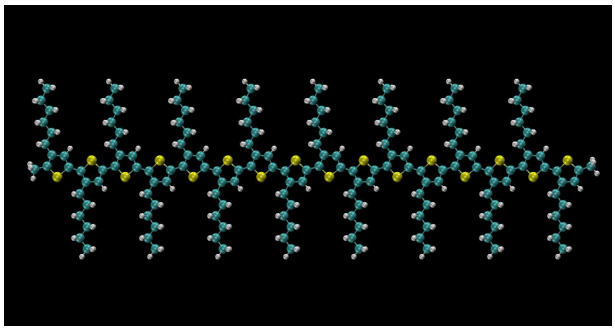

**Figure 2.1.:** *P3HT molecule composed by* 16 *thiophenes.*

The first step in the study of P3HT is to validate the model interaction. Specifically, we focus on the $\pi - \pi$ interaction that is dominated by long-range van der Waals dispersive forces and we adopt as a test case a pair of simple thiophene rings for which accurate first-principles calculations beyond Hartree-Fock theory are available (CCSD(T) and MP2 [84]). In Figure 2.2 the calculated MPMD results (symbols) are reported together with ab initio results (continous and dotted lines for CCSD(T) and MP2, respectively). Our model potential reproduce quite well the first-principles results being in between the CCSD(T) and MP2 curves, in particular for the dispersive $R^{-6}$ tail and for the estimation of the minimum energies [2].

We generate two P3HT molecules each formed by 8 monomers (16 thiophenes) with periodic boundary conditions along the backbone direction. The equilibrium lattice parameter along the backbone is 7.75 Å [2].

The assembling of the P3HT chains can be driven by two main contributions: the $\pi - \pi$ interaction between the aromatic rings of the backbones of neighboring molecules, promoting the parallel stacking of different chains, and the chain interdigitation, inducing molecules alignment in the same plane [2] (see Figure 2.3).

As for the $\pi - \pi$ binding energy, we consider two polymer chains at varying distance in a face-to-face configuration and we found a minimum at 4 Å (see Figure 2.4). The interactions between backbones are dominated by the thiophene-thiophene interactions calculated above. Additional smaller dispersive and electrostatic contributions due

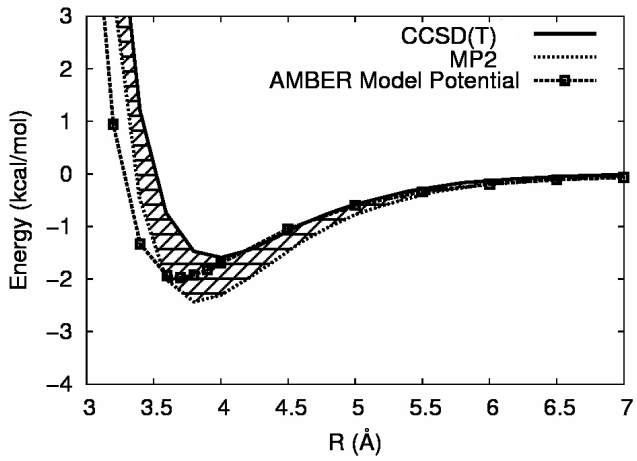


**Figure 2.2.:** *Interaction energy of a thiophene dimer as a function of the thiophenes distance calculated according to MPMD (symbols) CCSD(T) (continuous line) and MP2 (dotted line) methods. (Adapted with permission from J. Phys. Chem. C, 2011, 115 (2), pp 576-581. Copyright 2011 American Chemical Society [2].)*

to the atoms of the alkyl chains increasing the binding energy to 0.3 eV per thiophene.

The second driving force for the assembling is associated to the interdigitation between parallel molecules in an edge-to-edge configuration. We calculate the interaction as a function of distance and we found two minima, one at 13.6 Å and another at 16.0 Å , separated by an energy barrier as high as 0.3 eV (see Figure 2.5).

The molecule-molecule assembling force described above is consistent with the results for cohesion in the bulk crystalline phase [2]. The orthorhombic unit cell of crystalline P3HT with cristallographic vectors lying respectively in the alkyl side chains ($a$), stacking ($b$) and backbone ($c$) directions is represented in Figure 2.6. The bulk energy dependence on the molecules separation can be calculated by performing a series of geometry optimizations by varying the lattice parameters $a$ and $b$ in the range 13.0-16.2 Å and 6.8-10.0 Å (corresponding to a thiophene-thiophene distance of 3.4-5.0 Å). The value of $c$ is kept fixed at 7.75 Å.

In Figure 2.7 it is reported the corresponding color-map of energy as a function of $a$ and $b$. The energy profile along the $\pi - \pi$ direction $b$ shows a larger variation ($\sim$ 0.5 eV/thiophene) and a well defined minimum consistent with

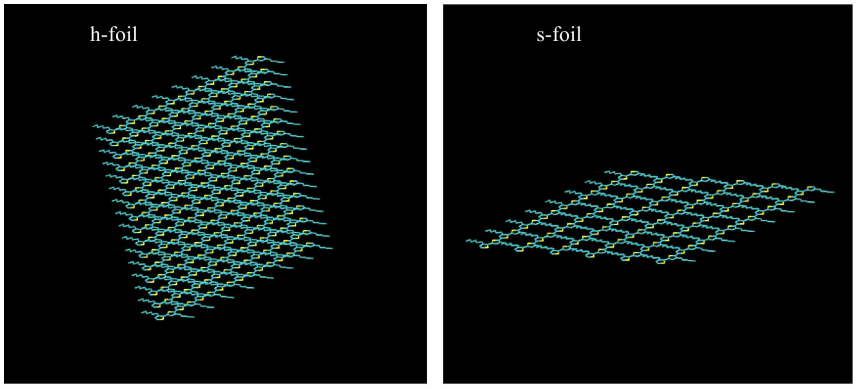


**Figure 2.3.:** *Assembling of P3HT molecules. In the h-mechanism the assembling of single P3HT chains is driven by the $\pi - \pi$ interactions, resulting in the formation of h-foil (left). In the s-mechanism the assembling brings to the formation of s-foils (right).*

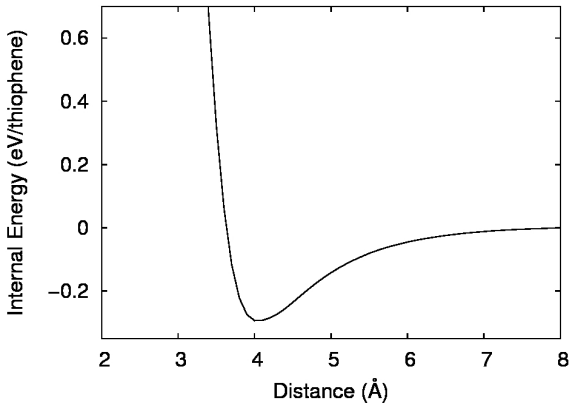


**Figure 2.4.:** *Static interaction between two P3HT chains at different $\pi - \pi$ distances.*

the above results for thiophene-thiophene and polymer-polymer face-to-face interactions. The energy variation along *a* (interdigitation) is sizably smaller (as small as $\sim 0.1$ eV/thiophene), showing a weak interaction between hexyl groups of neighboring chains [2]. Notably, the two minima of Figure 2.7 can be linked to the corresponding minima of the edge-to-edge (Figure 2.5) and face-to-face curves (Figure 2.4).

The $A'$ absolute minimum at distances lower than 14 Å, in Figure 2.7 corresponds to a ideal situation where the polymer chains (in vacuo and at low T) are fully interdigitated. This is unlike to occur in real systems at finite temperature where the thermal fluctuations of hexyl chains

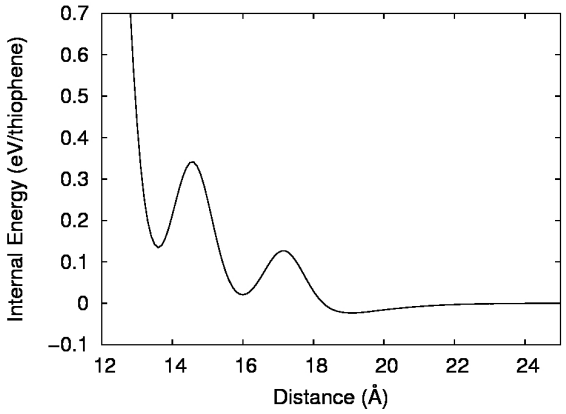


**Figure 2.5.:** *Static interaction between two P3HT chains at different interdigitation distances.*

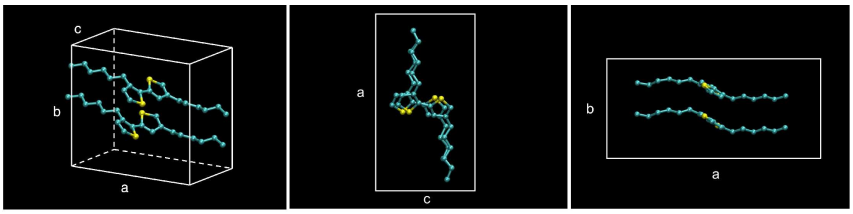


**Figure 2.6.:** *Perspective-view (left), top-view (center) and side-view (right) of P3HT equilibrium structures. The white box represent the othorombic unit cell with the corresponding lattice parameters. (Adapted with permission from J. Phys. Chem. C, 2011, 115 (2), pp 576-581. Copyright 2011 American Chemical Society [2].)*

and other sources of disorder (such as solvents and chemical contaminants) hinder the perfect interdigitation. This give rise to a larger edge-to-edge distance corresponding to minimum $A$ of $a = 15.8$ Å and $b = 8.0$ Å (corresponding to a thiophene-thiophene distance of 4 Å) in Figure 2.7.

The above analysis permits to conclude that the P3HT assembling is mainly driven by the $\pi - \pi$ interaction [2].

## 2.2 P3HT ASSEMBLING AND INTERMOLECULAR FORCES

Due to the fact that in vacuo the ruling interaction between two polymer chains is the $\pi - \pi$ one, it is possible to build two-dimensional P3HT structures formed by chains stacked on top of each other. This structure (here-

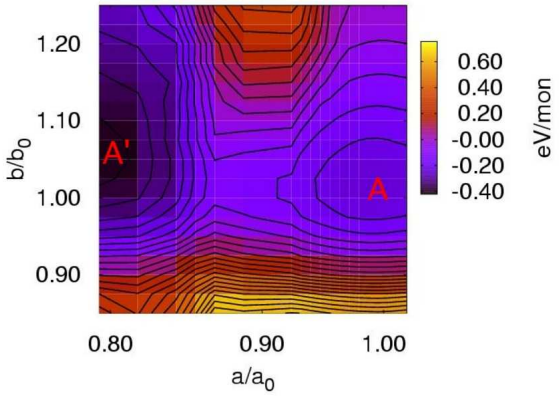


**Figure 2.7.:** *Energy landscapes obtained by MP for the bulk P3HT structure. The lattice parameters are referred to the equilibrium values $a_0$ and $b_0$ while the total energy is referred to the energy of two unbound chains. (Adapted with permission from J. Phys. Chem. C, 2011, 115 (2), pp 576-581. Copyright 2011 American Chemical Society [2].)*

after named h-foils) have hydrophobic surfaces exposing the hexyl chains (see Figure 2.3 left).

Two different foils interact attractively and can spontaneously organize into bilayers [2]. The thiophene rings in the resulting structure turn out to be tilted, as a result of a long-range interaction with the other foil (Figure 2.8 top panels) [2]. In particular, it was found that the thiophene rings belonging to adjacent h-foils formed in a zigzag-like configuration less interdigitated (16.2 Å) with respect to the ideal minimum energy phase. Such a value is in agreement with the experimental results [80].

On the other hand, in presence of a planar surface strongly interacting with the polymer (e.g. with a binding energy for the face-on polymer comparable with the $\pi - \pi$ interaction) it is likely that P3HT molecules will align on the substrate forming s-foils (see Figure 2.3 right) [2]. The polymer is expected to further grow according to a layer-by-layer mechanism as depicted in Figure 2.8 bottom panel .

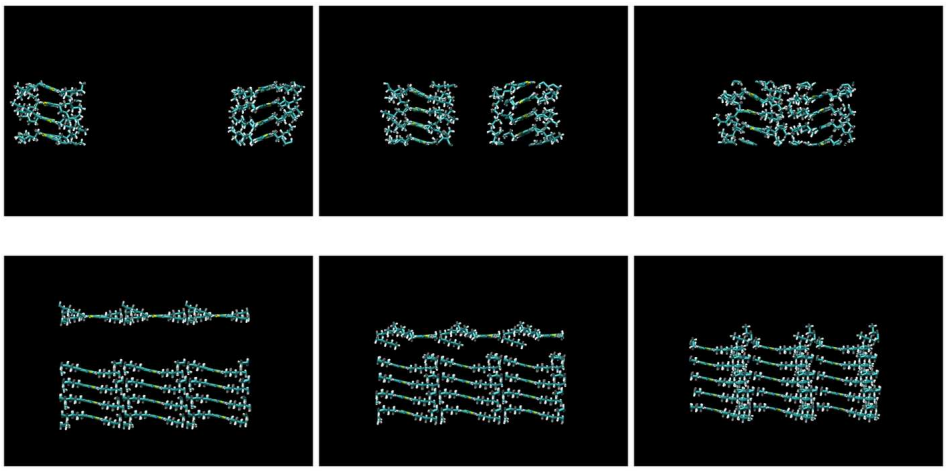

**Figure 2.8.:** *Assembling of P3HT foils. In the h-mechanism (top), two h-foils assemble in a zigzag-like final structure. In the s-mechanism (bottom), one s-foil stacks on top of a P3HT semi bulk in the aligned final structure. (Adapted with permission from J. Phys. Chem. C, 2011, 115 (2), pp 576-581. Copyright 2011 American Chemical Society [2].)*

## 2.3 P3HT CRYSTALLINE BULK PHASES

In the present work, in order to study the crystallinity of the polymer bulk phase, we calculate a functional of the atomic positions, hereafter named $S(q)$:

$$S(\mathbf{q}) = \frac{1}{N} \left| \sum_{j=1}^{N} f_j \cdot e^{-i\mathbf{q}\cdot\mathbf{x}_j} \right| \tag{2.1}$$

where $\mathbf{x}_j$ are the coordinates of the $j$-th atom, $N$ is the number of atoms and $|\mathbf{q}| = 2\pi/\lambda$ is any possible wave vector. By choice, in the calculation of $S(q)$, we take into account a weight $f_j$ proportional to the number of electrons for each atomic species. $S(q)$ is related to the structure factor of the system [85].

$S(q) \sim 0$ when the distribution of atomic positions is disordered (as occurs in liquids), conversely, when atoms are periodically distributed with period $\lambda$, then $S(q) \sim 1$ for wavevectors satisfying the Bragg condition (i.e. $q = 2\pi(n\lambda)^{-1}$).

This calculation of $S(q)$ has been performed for the different atomic models of infinite bulks considered in this work. The first case is reported in Figure 2.9 left and con-

sists in an ideal structure formed by s-foils separated by 4 Å (hereafter named ideal s-crystal). In the middle panel of Figure 2.9 it is reported the case of the perfect crystal relaxed at low temperature. Finally, the same bulk equilibrated at room temperature can be found in the right panel of Figure 2.9.

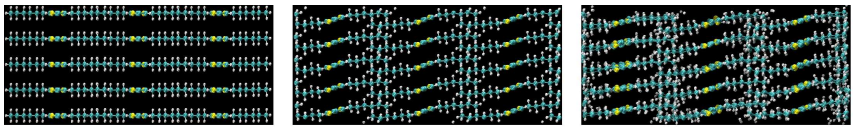

**Figure 2.9.:** *P3HT ideal s-crystal (left), P3HT bulk relaxed at low temperature (center) and P3HT bulk after a room temperature annealing (right).*

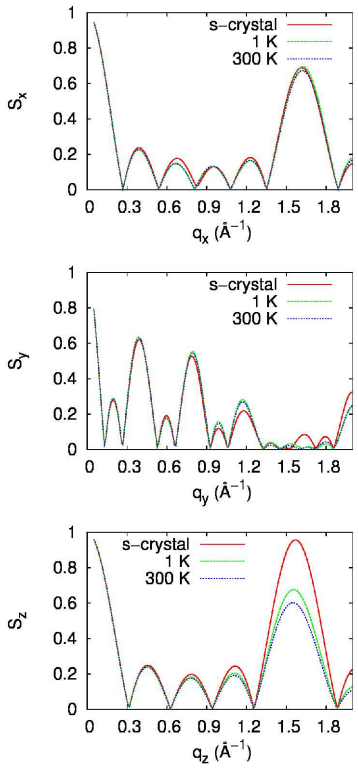


**Figure 2.10.:** *$S(q)$ for an ideal s-crystal and for a bulk relaxed at 1 K and 300 K. The direction $x$ is parallel to the backbone (top panel), the $y$ corresponds to the interdigitation (middle panel) and the $z$ to the $\pi - \pi$ (bottom panel).*

Figure 2.10 shows that the order of the crystalline bulk at low temperature (green) is preserved when heated at room temperature (blue) and only small differences can be

appreciated for the $S_z$ curves in the $\pi - \pi$ direction. The most relevant difference can be found when comparing the crystalline bulks to the ideal s-crystal. The peak at $q_z = 1.62$ Å$^{-1}$ decreases in the crystalline bulks as a result of the tilt of thiophene rings with respect to the $x$ direction.

## 2.4 P3HT SURFACES

The equilibrium P3HT crystal can be cut across the $\pi - \pi$ or the interdigitation directions, obtaining a 010 or 100 surface, respectively. The surfaces equilibrated at 1 K and at room temperatures are shown in Figure 2.11.

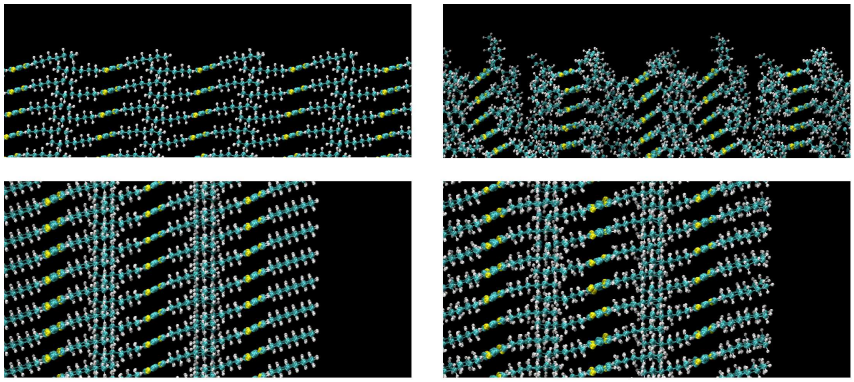

**Figure 2.11.:** *Configuration of a P3HT* 010 *(top) and* 100 *(bottom) surfaces after a low temperature relaxation (left) and a room temperature annealing (right).*

The surface energy in the two cases has been evaluated and it is 0.008 J/m$^2$ larger for the 010 surface. This is consistent with the larger cohesion in the $\pi - \pi$ cut with respect to interdigitation. At low temperature, we note a sizable difference in the order of the two surfaces, resulting in the different $S_z$ peaks (green and red in Figure 2.12 bottom). In particular, the peak of the 010 surface is higher than that of the 100. This depends on the fact that 100 surface (having flexible hexyl terminating groups) gives rise to a shrinking of the underlying $\pi$ channels.

On the other hand, at room temperature the 010 surface (s-foil terminated) gives rise to a sizable microstructure evolution characterized by an increase of disorder (see Figure 2.11 top right). The corresponding order parameter (green curves in Figure 2.12) lowers in all the directions.

Once more, the different behavior can be attributed to the higher excess energy induced by the 010 cut.

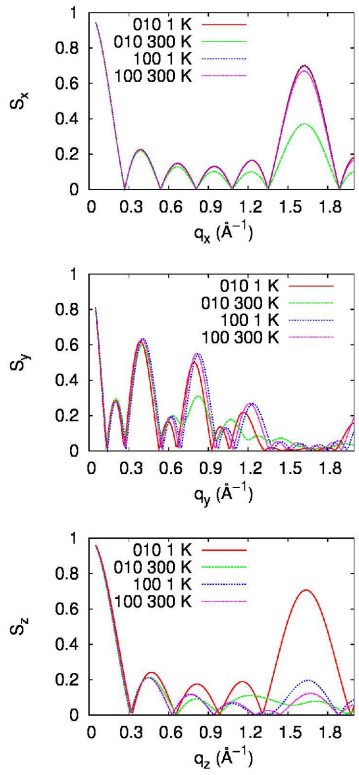


**Figure 2.12.:** *$S(q)$ for* 010 *and* 100 *surfaces relaxed at* 1 *K and at room temperature.*

## 2.5 NANOCRYSTALLINE P3HT

The polymer layers occurring in the hybrid interfaces can derive from the aggregation of nanocrystals previously formed during synthesis. The structure and the properties of a single nanocrystals have to be investigated in order to better understand the polymer morphology in real interfaces and the modifications in the polymer caused by the presence of the inorganic substrate. In particular, the interdigitation between the molecules has an effect on matching the lattice parameters of the substrate, affecting the deposition of the polymer and the order at the interface.

We study P3HT nanocrystals of different dimensions in order to investigate the possible dependence of the interdigitation (that is the distance between h-foils) on the size of polymeric nanoparticles. To this aim, we build a series

of model nanostructures by putting together s-foils and h-foils composed by polymer chains each formed by sixteen thiophenes. The initial interdigitation distance is chosen to be the same of a perfect crystalline bulk (15.8 Å [2]). In Figure 2.13 is reported an example of the system studied.

Table 2.1 (columns 1 and 2) reports the size of the systems chosen for the analysis: the symbol $s$ indicates the number of s-foils (growing in the $z$ direction) while $h$ indicates the number of h-foils (growing in the $y$ direction) (see Figure 2.13). For each nanocrystal we perform a relaxation by annealing the system at low temperature. The distances between the h-foils (i.e. interdigitation) are reported in column 3 of Table 2.1. In some cases we study the nanocrystals resulting by applying the periodic boundary conditions (pbc) in one or two directions, by allowing relaxations in the corresponding cell dimensions.

First of all we note that there exists a non-monotonic dependence of the lattice parameter on the size of the nanocrystals. Table 2.1 shows that for pbc along $h$ and $s$ (an infinite slab of width 16T), the distance between h-foils is the maximum, reaching one of the distances previously identified for the intedigitation of two infinite polymer chains (16 Å).

If pbc are applied only along one direction, the interdigitation distance is smaller (from 13 to 14.6 Å with an exception at 18 Å). Furthermore, whenever the pbc are present, the zigzag-like conformation is observed in the relaxed nanocrystals similarly to the case of the infinite bulk.

As for the finite systems with no pbc, they always give rise to a reduction of the interdigitation distance with respect to the slab, but there is a non-monotonic dependence on the size. Lower values are found for the nanocrystals composed by eight or sixteen s-foils (12.57 Å), while those composed by four s-foils give higher interdigitation distances (up to 16.11 Å). Furthermore, these latter turn out to be the more ordered (see Figure 2.13 compared with Figure 2.15). The increase of the size in the $z$ direction ($s$) is associated to a contemporary twisting of the structure that tends to assume a spherical shape in order to minimize the surface energy (see Figure 2.15).

Figure 2.14 and Figure 2.15 show the initial and final configurations of two P3HT nanocrystals of size $h$x$s$ of 16x16 and 4x16 respectively. In the insets, the structure of the 010

**Table 2.1.:** *Interdigitation distance in a P3HT bulk depending on the number of s- and h-foils.*

| h | s | h-foils distance |
|---|---|---|
| 2 | 4 | 15.32 |
| 2 | 8 | 13.66 |
| 2 | 16 | 13.85 |
| 2 | 8 (pbc) | 13.09 |
| 4 | 4 | 15.70 |
| 4 | 8 | 13.09 |
| 4 | 16 | 12.82 |
| 4 | 8 (pbc) | 14.28 |
| 8 | 4 | 16.11 |
| 8 | 8 | 12.82 |
| 8 | 16 | 12.82 |
| 8 | 8 (pbc) | 14.28 |
| 16 | 4 | 16.11 |
| 16 | 8 | 14.74 |
| 16 | 16 | 12.57 |
| 16 | 8 (pbc) | 14.61 |
| 4 (pbc) | 4 | 17.95 |
| 4 (pbc) | 8 | 13.09 |
| 4 (pbc) | 16 | 12.82 |
| 4 (pbc) | 8 (pbc) | 16.11 |

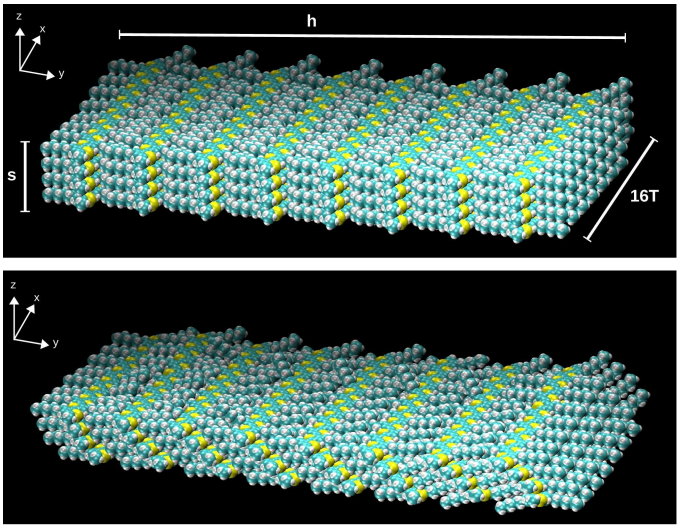


**Figure 2.13.:** *Initial and relaxed configuration of a P3HT 8x4 crystal.*

surfaces are shown together with the actual interdigitation distance decrease. In the same figures the structure factors $S(q)$ along the $y$ direction (the interdigitation direction) are reported before and after the relaxation. The $S_y$ peaks are lower than those of an ideal s-crystal, confirming the increase of disorder and they shift toward higher $q$ values, attesting the reduction in the interdigitation distance.

## 2.6 CONCLUSIONS

The present analysis provides evidence that severe changes of lattice parameters and morphology are expected for finite size polymers nanocrystals. This must be taken into account in the hybrid polymer/ZnO interface when the polymer film on the metal oxide can result from the aggregation of previously formed polymer nanocrystals. This will be widely investigated in the next chapter.

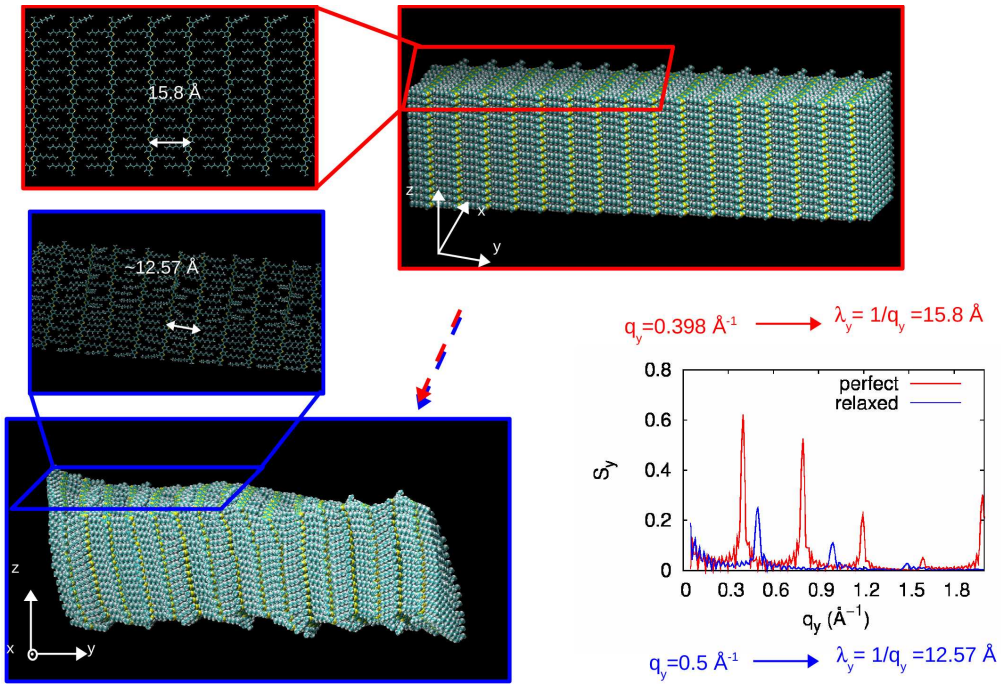


**Figure 2.14.:** *Initial and relaxed configuration of a P3HT 16x16 crystal and corresponding $S(q)$ in the interdigitation direction.*

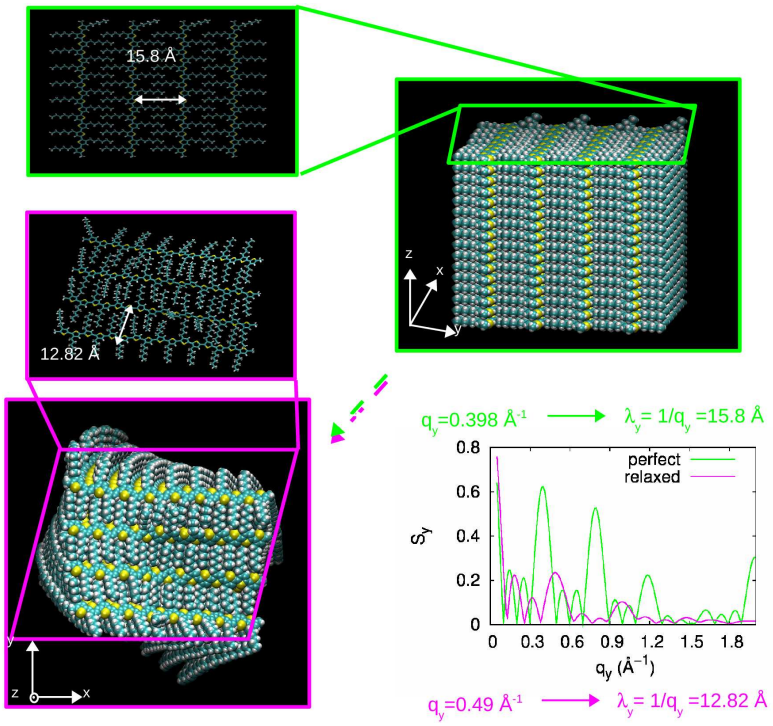


**Figure 2.15.:** *Initial and relaxed configuration of a P3HT 4x16 crystal and corresponding $S(q)$ in the interdigitation direction.*

# 3

# POLYMER/SEMICONDUCTOR INTERFACE

## Contents



## 3.1 HYBRID INTERFACES

In this chapter, the interface between the metaloxide ZnO and the polymer P3HT is investigated by means of atomistic simulations based on model potential molecular dynamics. Such an interface is the core of the hybrid P3HT/ZnO solar cell whose efficiencies are typically too low for practical applications, with a record of 2% [27] in bulk heterojunction architectures. The different behavior of the same polymer P3HT in combination with ZnO or with the organic PCBM (for which relatively high efficiencies of 5% are possible [86]), shows the need of a better understanding of the main physical concepts controlling the interface structure at the atomic scale.

In this chapter, after discussing the most stable and abundant ZnO surface, we set up the force model describing the polymer/ZnO interaction and we generate several models of P3HT/ZnO interfaces. Our goal is to understand the polymer organization at the interface in terms of crystallinity and disorder by including different kinetic and thermodynamic conditions. The implications of morphol-

ogy on the transport properties are investigated as well in terms of effective models.

## 3.2 ZINC OXIDE

Zinc oxide (ZnO) is a wide band gap semiconductor (3.37 eV) [26] that provides very good electron mobility (205 $cm^2\ V^{-1}\ s^{-1}$), it is non-toxic, and it can be grown in a variety of highly crystalline nanostructures [26, 87] which are commonly used as electron acceptors. In combination with organic donors (e.g. conjugated polymers or molecules), ZnO nanostructures have been used to synthesize hybrid bulk heterojunctions. In particular, nanorods have attracted great attention as elongated nanostructures that could contribute to improve the charge transport in the hybrids.

Zinc Oxide crystallizes in two main forms, hexagonal wurtzite and cubic zincblende. The wurtzite structure is most stable at ambient conditions and thus most common. The lattice parameters of the zinc oxide are $a = 3.25$ Å and $c = 5.20$ Å (see Figure 3.1).

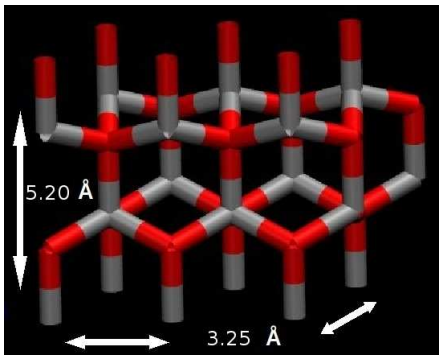


**Figure 3.1.:** *ZnO wurtzite structure.*

The most energetically stable surface of crystalline ZnO is the non-polar $(10\bar{1}0)$ and, hereafter, we will focus on it since it is the most common in ZnO. For example, ZnO typical nanorods used in hybrid bulk heterojunctions [88] exhibit six equivalent $(10\bar{1}0)$ surfaces of lateral size larger than 10 nm.

The atomic scale model of the ideal ZnO surface is generated by cutting a wurtzite ZnO crystal along the $(10\bar{1}0)$ plane and by relaxing it at low temperature. The atomic

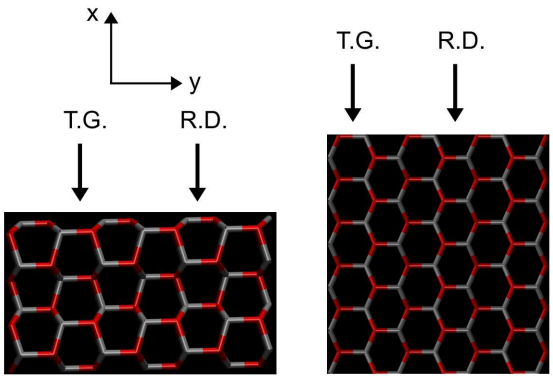


**Figure 3.2.:** *Trench grooves (T.G.) and row of dimers (R.D.) in a portion of ZnO.*

scale model after atomic relaxation based on MPMD is reported in Figure 3.2 The atomic scale structure of the $(10\bar{1}0)$ surface exhibit trench grooves alternated with rows of ZnO dimers (channels), both oriented along the [010] crystallographic direction. Hereafter in this chapter, the $x$ axis is always chosen parallel to this [010] crystallographic direction Figure 3.2. As already discussed in chapter 1, in order to describe the ZnO crystalline surface, we adopt the Buckingham-type potential. This potential describes properly several properties of bulk and nanocrystals such as elastic constants, equilibrium lattice energy, cell parameters, elastic and dielectric constants [70].

## 3.3 ADHESION OF A SINGLE P3HT MOLECULE ON THE ZINC OXIDE SURFACE

The first step in the analysis of the ZnO/P3HT interface is the study of the adhesion of a single polymer molecule on the surface. For this purpose a P3HT molecule composed by 16 monomers is put at different distances from the surface with the thiophene rings parallel to it (face-on alignment) and the backbone parallel to the ZnO dimers.

The basin of interaction between the ZnO and the P3HT is reported in Figure 3.3, where the unrelaxed energy (calculated without allowing atomic relaxation of the polymer due to the surface) is reported as a function of the relative distance between molecule and surface. The minimum of the interaction is found at 3.7 Å and corresponds to

an energy 0.35 eV/thiophene. The interaction vanished at distances larger than 8 Å. By starting from the minimum energy distance and by further relaxing the system we identify the lowest energy configuration of the polymer on the surface with a binding energy as large as 0.73 eV/thiophene. The driving force for this binding energy is due to the attraction beween the negative carbon atoms of the thiophene rings of the polymer and the positive zinc atoms of the surface. The P3HT polymer on the ZnO surface preservs the quasi-planar configuration of the isolated molecule.

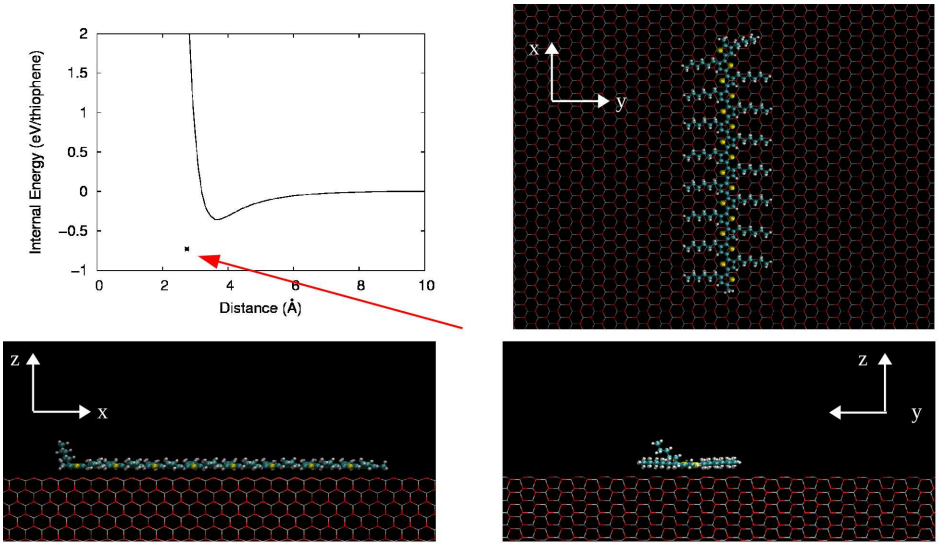


**Figure 3.3.:** *Interaction and adhesion of a P3HT molecule on a ZnO surface.*

## 3.4 P3HT/ZNO INTERFACE

In order to generate models of the P3HT/ZnO interface we consider a planar ZnO surface ideally perfect and we put on it the organic polymer. There are three possible ways to apply boundary conditions to the interface: (i) periodic boundary conditions for both ZnO and polymer; (ii) no periodic conditions at all, i.e. finite size cluster; (iii) mixed periodic-non periodic conditions. The case (i) has the advantage of avoiding free surfaces, but it can introduce artifacts in the polymer assembling since it imposes the same periodicity for both the polymer and the ZnO

surface (that have different lattice parameters). In case (ii) there are surfaces in the ZnO cluster with sizable effects on the crystal slab structure (unless fixing the atomic positions, that is not compatible with finite temperature simulations). In this work, we prefer to adopt the boundary conditions of type (iii) where the interface is obtained by putting a non periodic finite size polymer nanocrystal (up to $10^4$ atoms) on a periodic ZnO surface. In this way the polymer lattice spacing is not constrained by boundary conditions. If the polymer nanocrystal is large enough, the results that are calculated under these boundary conditions can be applied to real polymer/ZnO interfaces.

As for the polymer crystalline structure, it is experimentally known that the polymer is highly sensitive to the synthesis conditions [82]. Accordingly, within the conditions described above, we explore two different ways of generating the hybrid interfaces hereafter named Low Deposition Rate (LDR) and High Deposition Rate (HDR). In the LDR the polymer nanocrystal is assembled on ZnO layer by layer at a low rate while fully relaxing the atomic positions at each step. In the HDR case, the polymer nanocrystal is cut from an ideal infinite ordered bulk and it is merged and relaxed on the ZnO surface. The above two cases are representative of two opposite experimental regimes; the LDR corresponds to the case where the substrate-molecule interaction is the ruling assembling mechanism; in this case the polymer molecules can face on the surface (see section 3.3) forming successive s-foils (see chapter 2). The HDR case corresponds to the physical regime in which the P3HT molecules are likely to aggregate before interacting with the surface; in this situation the polymer-polymer forces controls the assembling of the interface.

In both LDR and HDR, the P3HT nanocrystals are chosen of dimensions 6 nm x 11 nm x 4 nm and are formed by 30 molecules of length 6 nm with backbones oriented along the $x$ direction, in agreement with [89], in which a preferential orientation of the P3HT along the dimer rows of ZnO is found. The size of these nanocrystals is comparable with P3HT crystalline domains in real samples (10-50 nm [2]). Atomic relaxations are always obtained by extensive low temperature annealings followed by conjugated gradients energy optimizations. Temperature effects are also taken

into account by heating and equilibrating the interfaces at room temperature.

## 3.5 P3HT/ZNO INTERFACE: LOW DEPOSITION RATE

In the regime of low deposition rate (LDR) the polymer tend to organize parallel to the substrate forming s-foils [2]. This has been already discussed chapter 2 (see panel *a* of Figure 3.4).

The atomistic models generated during the LDR assembling procedure are reported in Figure 3.4.

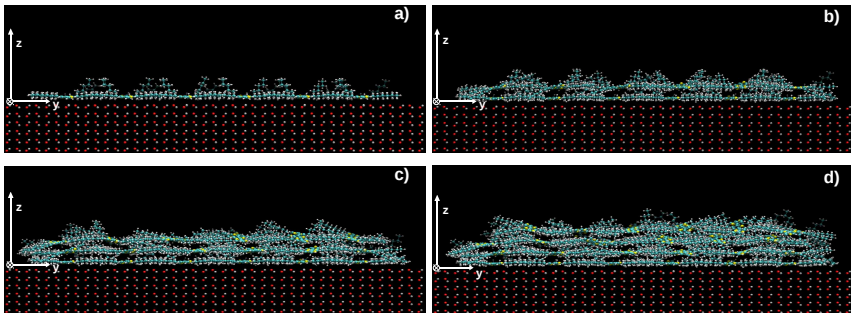


**Figure 3.4.:** *Assembling of P3HT layers on the ZnO surface.*

In each layer (s-foil) deposited, the polymer molecules are aligned with the backbone parallel to rows of Zn-O dimers and the molecule-molecule interdigitation distance is controlled by its matching with the lattice spacing of the ZnO surface, particularly for the first layers. Given the sensitivity of the polymer crystal structure on synthesis conditions, the above mismatch can be important in driving the final structure of the polymer at interface. The experimental interdigitation distance in the P3HT is reported to be 16.8 Å. Since the ZnO surface lattice parameter in the $y$ direction is 5.20 Å, the best matching between the polymer and the ZnO surface is obtained by putting one polymer chain every three rows (interdigitation distance of 15.6 Å corresponds to three times 5.20). For ideally perfect polymer structure, the calculated interdigitation distance in perfect crystals is smaller than the experimental one and it can assume two values (as already discussed in section 2.1): 13.6 Å for high density phase and 15.8 Å for the lower dense phase. Both experimental and high density ideal phase values gives a sizable mismatch with the ZnO

surface. For the low density case a better matching can be obtained. For this reason, in order to favor the order at the interface, we generate our atomistic model by using s-foils with interdigitation distance 15.8 Å.

The s-foil is let to relax on the surface under the attractive interaction with the ZnO substrate. We find that the initial interdigitation distance is affected during the formation of the interface. The initial value is preserved only for the first P3HT layers and the polymer disorder increases with the distance from ZnO (see Figure 3.4 and Figure 3.5).

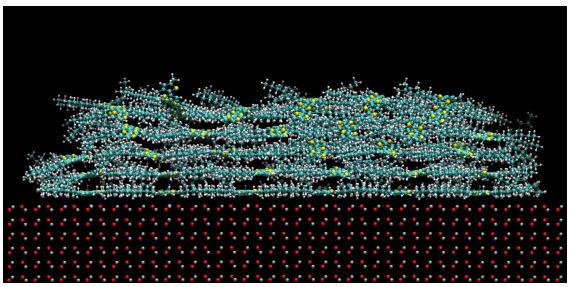

**Figure 3.5.:** *Final configuration of the LDR system at low temperature.*

The above visual analysis is confirmed quantitatively by calculating the structure factor of the polymer in the three $x$, $y$ and $z$ direction. In particular the peak in $y$ and $x$ direction are lowered with respect to the ideal s-crystal (compare Figure 3.6 left and middle with Figure 2.10 top and middle). The lowering of $S_z$ in top-right panel of Figure 3.6 and its broadening, indicates an increasing disorder in the $\pi - \pi$ direction.

The interface has been also studied at room temperature (annealing at 300 K by Nosé-Hoover thermostat). It is found that the first polymer layer remains fixed to the surface because of the strong ZnO-polymer interaction but the disorder induced by thermal fluctuations affects subsequent layers (see Figure 3.7). This is indicated by the lowering of $S_y$ in the bottom-middle panel of Figure 3.6. Moreover, the $S_z$ peak shift to lower $q$ values indicates an increase of the interplanar distance (from 4 to 4.5 Å) induced by temperature.

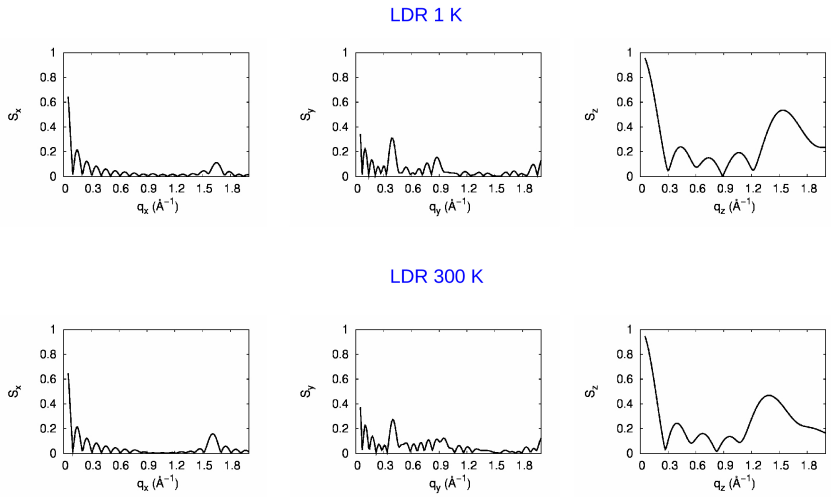


**Figure 3.6.:** *Structure factor in the three crystallographic directions for the LDR interface at low (top) and room temperature (bottom).*

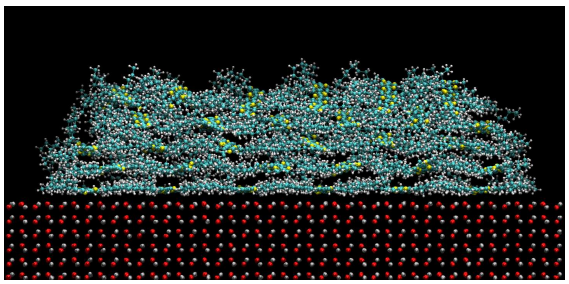

**Figure 3.7.:** *Final configuration of the LDR system at* 300 *K.*

## 3.6 P3HT/ZNO INTERFACE: HIGH DEPOSITION RATE

The HDR interface is generated by putting a previously formed P3HT s-crystal (with same dimension of the LDR final model) at 7 Å of distance from the ZnO surface (see Figure 3.8 upper panel) and relaxing (Figure 3.8 lower panel).

Different HDR interface models are possible depending on the crystallographic polymer plane that interacts with the ZnO surface. We choose in particular the 010 and the 100 planes and we refer to them by 010 HDR and 100 HDR hybrid interfaces, respectively. In the 010 HDR interface, the polymer nanocrystal is deposited on the substrate in the face-on configuration and the $\pi - \pi$ channels are perpendicular to the surface, as in the LDR case (Figure 3.8).

In the 100 HDR interface, the polymer nanocrystal is deposited by exposing the alkyl chains to the ZnO, and the $\pi - \pi$ channels are parallel to the substrate (Figure 3.11).

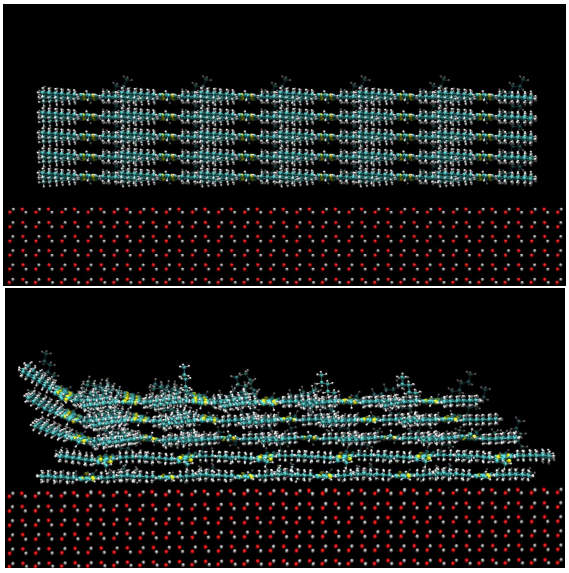

**Figure 3.8.:** 010 *HDR system before (upper panel) and after (lower panel) the relaxation at low temperature.*

After relaxation the $\pi - \pi$ channels of the 010 HDR interface are not anymore perpendicular to the surface (Figure 3.8). Consistently, a very low $S_y$ peak is found (top-middle panel of Figure 3.9). The $S_y$ peak of the polymer shifts accordingly to a smaller interdigitation distance with respect to the s-foil (from 15.8 to 13.6 Å) and corresponds to the dense polymer phase discussed in section 2.1. A general order is found in $x$ and $z$ directions (top-left and top-right panels of Figure 3.9, respectively), where the polymer backbones keep their straightness and the interplanar distance is preserved ($S_z$ is not shifted).

The effect of the temperature in this 010 HDR interface, is to increase the disorder of the system (see Figure 3.10) in the $x$ and $z$ directions (bottom-left and right panels of Figure 3.9). In addition, in the $z$ direction the temperature induces a higher interplanar distance. Interestingly, in the $y$ direction we observe that the order is slightly increased by the annealing (bottom-middle panel of Figure 3.9), standing for a temperature induced crystallization.

The second interface model in the regime of high polymer deposition is the 100 HDR interface where the $\pi$ channels are parallel to the ZnO surface and hexyl chains face

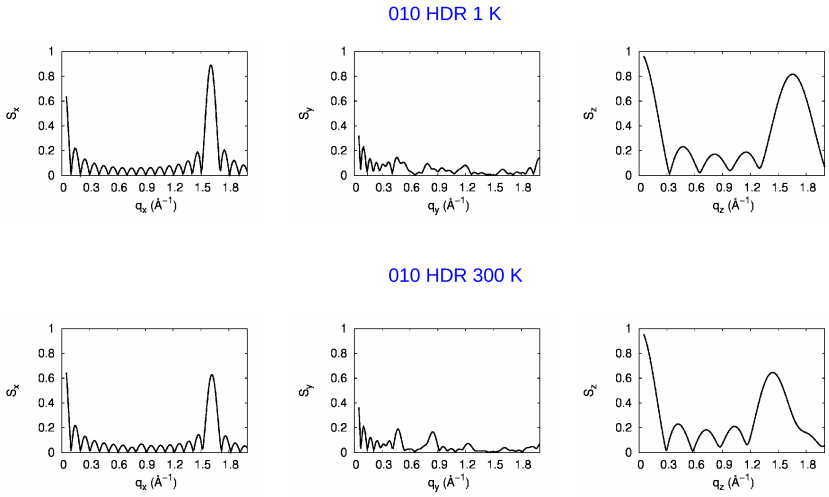


**Figure 3.9.:** *Structure factor in the three crystallographic directions for the* 010 *HDR interface at low and room temperature.*

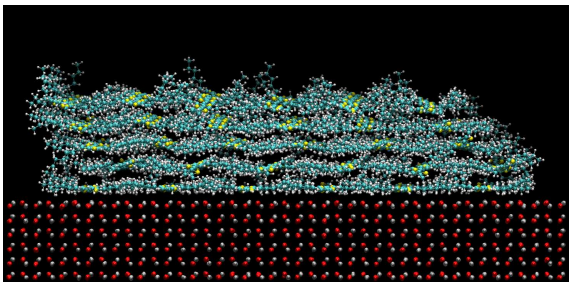

**Figure 3.10.:** *Final configuration of the* 010 *HDR system at* 300 *K.*

the substrate. We found that in this interface model the polymer is more disordered than in the 010 case and tends to bend toward the surface in order to increase the interactions with it (see Figure 3.11).

As shown in top-middle panel of Figure 3.12, the interaction with the substrate causes disorder in the $\pi - \pi$ direction and gives a low peak in $S_y$ structure factor (we recall that in this case the $\pi - \pi$ channels are along $y$, parallel to the ZnO surface). The average $\pi - \pi$ distance is found to increase from 4 to 4.8 Å. On the other hand, sharp peaks are present in $S_z$ (top-right panel of Figure 3.12) standing for a high order in the interdigitation direction. The shift of the $S_z$ peak with respect to the s-crystal shows a strong reduction in the interchain distance, and corresponds to 12.5 Å.

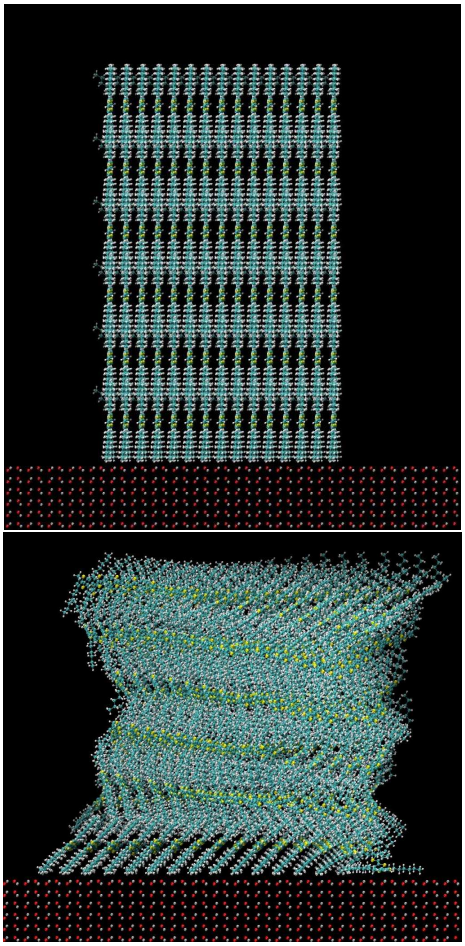

**Figure 3.11.:** 100 *HDR system before (left) and after (right) the relaxation at low temperature.*

At room temperature the 100 HDR interface (Figure 3.13) shows a partially restore of the crystalline order that can be observed in all directions (Figure 3.12 bottom panels). We can further recognize the zigzag-like conformation already observed for P3HT bulks in section 2.2.

The two HDR interface models have been compared in terms of interface energy (the energy of the hybrid interface with respect to separate components divided by the area of the interface) and binding energy. Despite the surface formation energy of the 010 surface is higher than that of the 010 one (by 0.008 $J/m^2$), its higher binding energy with the ZnO with respect to the 100 case (by 0.1 $J/m^2$), bring to a favourable formation of 010/ZnO interfaces with respect to the 100/ZnO systems. This is consistent with the preferential face-on orientation of polymer

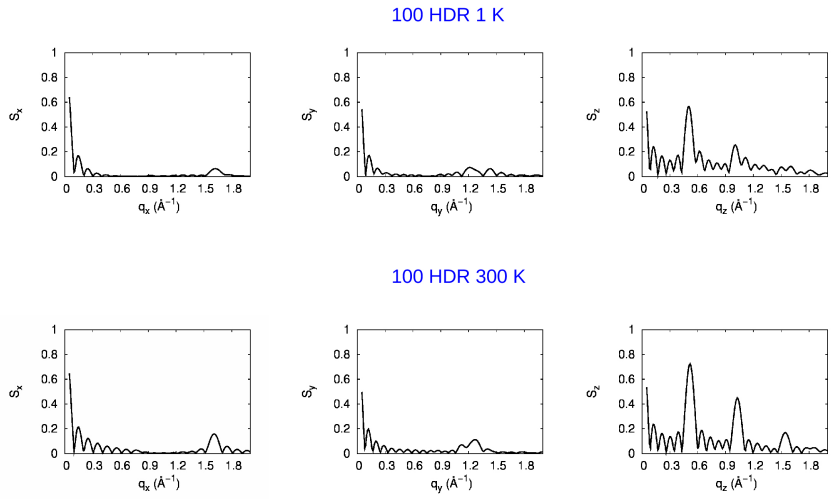


**Figure 3.12.:** *Structure factor in the three crystallographic directions for the* 100 *HDR interface at low and room temperature.*

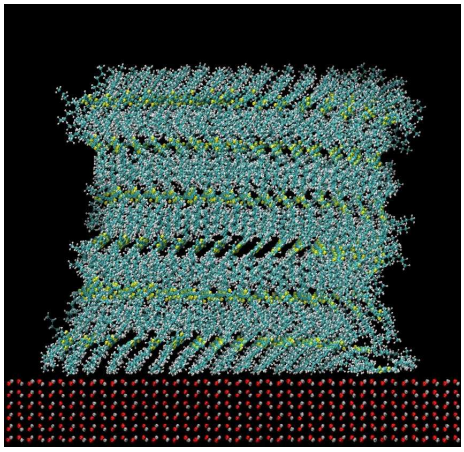

**Figure 3.13.:** *Final configuration of the* 100 *HDR system at* 300 *K.*

molecules on ZnO. In conclusion, present results shows that the 010/ZnO surface is the most likely to occur in P3HT/ZnO systems.

In order to better connect present analysis to experimental data we average the structure factor in the interface plane ($xy$) by calculating the $S_{xy}$ quantity. $S_{xy}$ recalls the Grazing Incident X-ray Diffraction (GIXD) measurement where X rays are diffracted by scattering parallel to the interface.

For the 010 HDR interface, the peaks of the polymer backbone and that of the interdigitation periodicity are still well recognizable in $S_{xy}$ curve ( right panel of Figure 3.14).

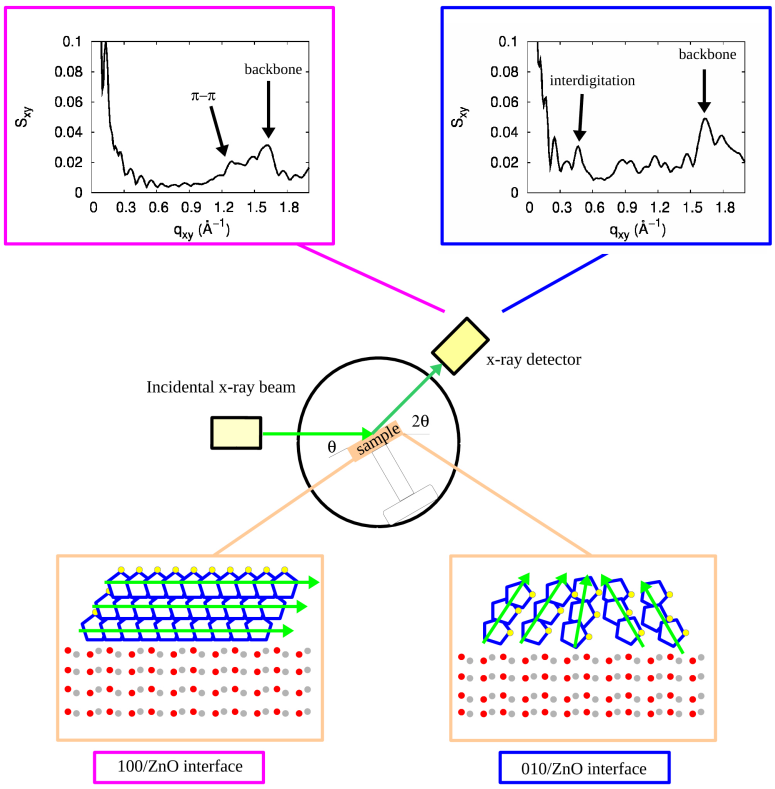


**Figure 3.14.:** *Structure factor in the xy plane for the HDR* 100 *(left) and* 010 *(right) systems.*

For the 100 HDR system (left panel of Figure 3.14) the peaks of backbone and $\pi - \pi$ distance are smaller and broader and the $S_{xy}$ exhibits much less structure in the range 0.3-1.1.

The $S_{xy}$ curve of the 100 HDR case is reminescent to the case of P3HT on glass. In fact, for crystalline polymer on glass a peaked region occurs at 1.6 Å$^{-1}$ close to our $\pi - \pi$ and backbone peaks and a more flat GIXD signal is found at smaller trasferred momentum. The agreement with the 100 polymer surface supports the experimental observation that the polymer $\pi$ channels are parallel to the glass substrate exposing the hexyl chains. In the case of the polymer on ZnO experiments show that the crystallinity peaks are completely lost.

A direct comparison with experiment is difficult because of the poor control of the crystalline surface. Experiments on ZnO gives a P3HT signal that does not correspond to our calculated 100 nor 010 crystalline surfaces. We attribute

such a result to the poor quality of the crystalline ZnO surface and to the strong polymer substrate interaction that induces disorder in the polymer backbones. Further measurements on more controlled ZnO samples would allow for a better comparison of our finding with experiments. However, the P3HT disorder at the inteface is consistent with our findings of polymer disorder induced by the strong polymer/ZnO interaction that favors the 010/ZnO interface.

The morphological features discussed above, are expected to modify the transport properties of the polymer. For example, in the case of a crystalline polymer, if the $\pi - \pi$ channels are orthogonal to the substrate, the carriers can easily move away from the interface before recombining. This corresponds to the most favorable case for photovoltaic efficiency. In the opposite case, when the $\pi - \pi$ channels are parallel to the interface or when the polymer is disordered, the carriers cannot easily move away from the interface. In conclusion, for transport and performances, the order in the direction normal to the interface is a key property. In the next section we will discuss an effective method to evaluate the charge mobility at the interface.

## 3.7 EFFECTIVE MODEL FOR THE TRANSPORT PROPERTIES

The stacking and the transport properties of the systems described above can be studied by using the concept of effective area. The idea is to represent each thiophene ring by an elliptical shape in the plane of the molecule (see inset of Figure 3.15). The projected overlap area $\Theta^{\perp}$ (in the normal $x$-$y$ plane) between pairs of neighboring molecules along $z$ can be then calculated. This quantity is related to the crystalline order of the system and it is small in disordered or amorphous polymer films. In particular, $\Theta^{\perp}$ is maximum when the thiophenes of two neighboring molecules are perfectly aligned and parallel to the $x$-$y$ plane. Conversely, $\Theta^{\perp}$ is smaller when thiophenes are shifted in the $x$ or $y$ direction or when the molecules are tilted with respect to $z$.

By referring to the Marcus theory [90, 91], the mobility $\mu$ in the polymer is given considering the local probability $k_{\alpha\beta}$ that a hole hops between neighboring molecules $\alpha$ and

$\beta$ [92]. $k_{\alpha\beta}$ , for a fixed temperature, is proportional to $J^2_{\alpha\beta}$, where $J_{\alpha\beta}$ is the transfer integral between the molecular electronic orbitals [93]. $J_{\alpha\beta}$ depends on the relative position and orientation of the two molecules. $J_{\alpha\beta}$ can be calculated from DFT for the case of two infinite thiophene chains oriented along $x$ direction and stacked along $z$.

In Figure 3.15 is reported in green the $J_{\alpha\beta}$ dependence on the relative $y$ shift of the two chains with respect to the dependence of the transfer integral $J_0$ calculated at the equilibrium distance $d_0$.

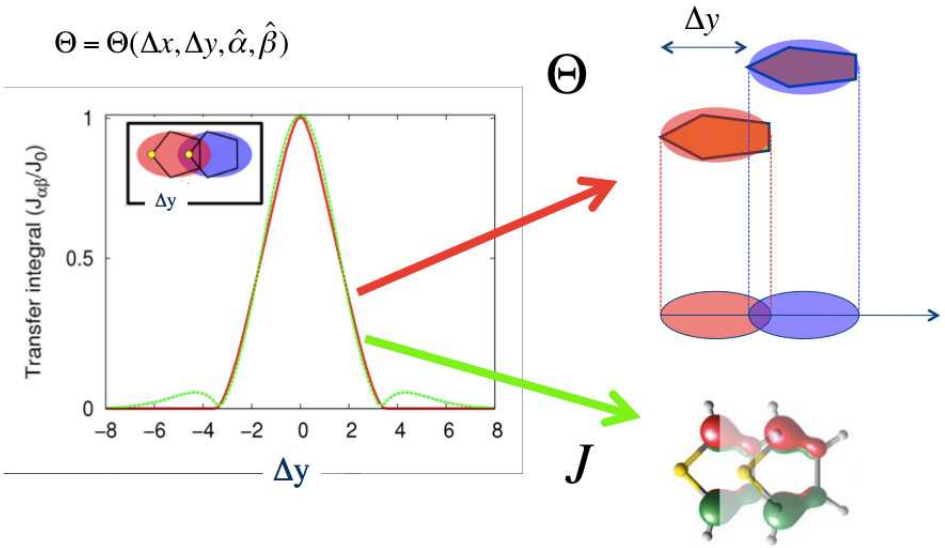


**Figure 3.15.:** *Comparison between the relative transfer integral $J_{\alpha\beta}/J_0$ as computed approximating thiophene rings by ellipses (red line) and first-principles calculations (green line). (Adapted with permission from J. Phys. Chem. C, 2011, 115 (19), pp 9651-9655. Copyright 2011 American Chemical Society [3].)*

The maximum $J_{\alpha\beta}$ is found at zero shift (i.e. maximum overlap area) and by increasing $y$ up to $y = 3.6$ Å it decreases monotonically to zero. In the same figure is reported in red the stacking parameter $\Theta^{\perp}$ calculated by using ellipses with eccentricity $\epsilon = 1.15$, chosen so as to best fit the first-principle calculations. Small differences (few percents) are found only at shifts 4-6 Å, but the overall agreement is good.

As for the $J_{\alpha\beta}$ dependence on the $\pi - \pi$ distance $d$ between the two molecules $J_{\alpha\beta}/J_0 = \exp(-\gamma(d - d_0)/d_0)$ [92]

has been used, where $\gamma$ is a fitting parameter. In conclusion, the geometrical stacking parameter $\Theta^{\perp}$ can be used as a good approximation for the quantum-mechanical $J_{\alpha\beta}$ dependence on $y$ shifts.

By combining the above results, $J_{\alpha\beta}$ can be calculated for any relative position and orientation of the two molecules without quantum-mechanical calculations. The local contribution for the mobility in the direction normal to the interface $\mu^{\perp}$ can be calculated from the knowledge of the overlap $\Theta^{\perp}$:

$$\mu \sim k \qquad k \sim J^2 \qquad J \sim \Theta^{\perp} \tag{3.1}$$

$$\frac{\mu^{\perp}}{\mu_0^{\perp}} = e^{-2\gamma\left(\frac{d-d_0}{d_0}\right)} \left(\frac{\Theta^{\perp}}{\Theta_0^{\perp}}\right)^2 \tag{3.2}$$

where $\mu_0^{\perp}$ and $\Theta_0^{\perp}$ are respectively the mobility and the effective overlap in the perfect P3HT crystal.

Equation 3.2 can be used to calculate the average normal mobility within polymer layers as a function of the distance from the interface, as shown in Figure 3.16 and Figure 3.17, where in the $x$-axis we report the distance from the interface in terms of the s-foils considered for the analysis in that point. As for the HDR interfaces, we choose to focus only on the 010 one due to its more favourable formation energy with respect to the 100 one. In this way, we can compare the results of two 010-like interfaces (the LDR and the HDR).

As for the low temperature cases, in the LDR model (in red in Figure 3.16) the effective mobility turns out to be about one half that of a perfect s-crystal (represented in blue) for the first two layers. Starting from the third layer the mobility strongly decreases due to the mismatch between the layers and, eventually, drops to zero. In the HDR case (in green in Figure 3.16), the behavior is opposite. In fact, the strong tilt of the $\pi - \pi$ channels in the first layers reduces the mobility, which is, though, partially recovered for the last two ones.

Figure 3.17 shows taht the effect of temperature (300 K) for both the two models is to further reduce the mobility, but preserving the overall behavior found at 1 K.

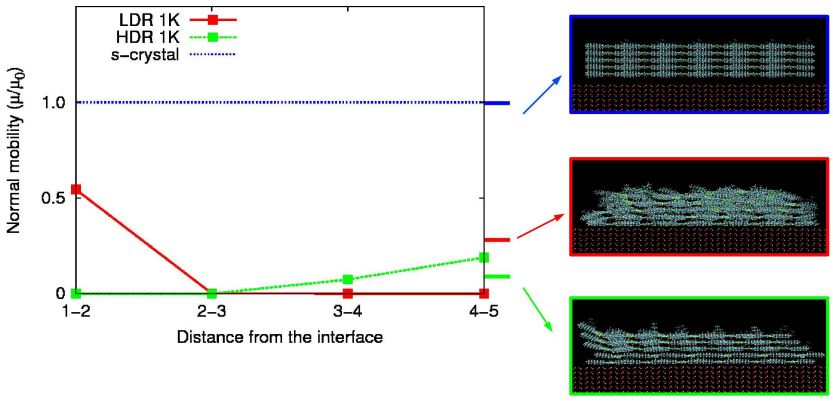


**Figure 3.16.:** *Normal mobility obtained at* 1 *K by approximating the thiophene rings with ellipses of eccentricity* $\epsilon = 1.15$.

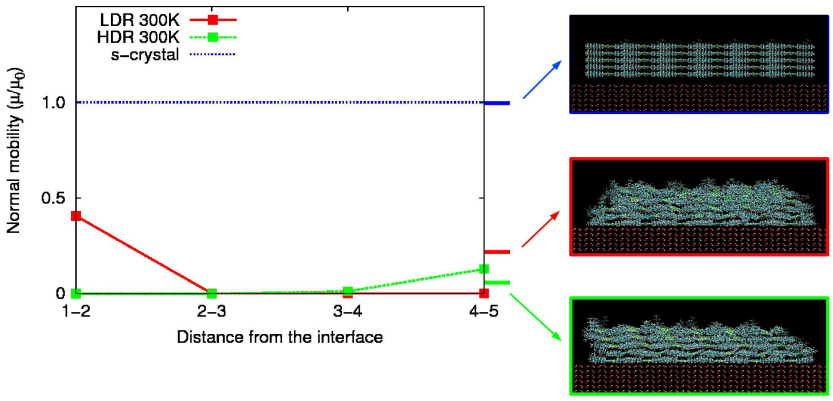


**Figure 3.17.:** *Normal mobility obtained at* 300 *K by approximating the thiophene rings with ellipses of eccentricity* $\epsilon = 1.15$.

## 3.8 CONCLUSIONS

In conclusion, the polymer crystal is highly affected at the interface with ZnO. The 010/ZnO interface is found to be the most favorable, with polymer thiophenes facing the ZnO surface due to the high molecule/surface interaction. Due to disorder at the interface, polymer chains are likely misaligned close to the ZnO surface thus reducing the normal carrier mobility in the first layers. Holes that are generated at the interface are not able to diffuse through the polymer and, as a consequence, they likely recombine with electrons. Similarly, excitons photogenerated within the polymer cannot easily move to the interface in order to be separated.

It is important to remember that the present models have been obtained under ideal conditions. We expect that thermal fluctuations, or the presence of the solvent or other chemical impurities, can further reduce the order at the interface. The possible presence of residual solvent at the interface will be investigate in chapter 5.

Some ideas and results of this chapter are adapted with permission from J. Phys. Chem. C, 2011, 115 (19), pp 9651-9655. Copyright 2011 American Chemical Society [3].

# 4

# TERNARY ZNO/ZNPC/P3HT SYSTEM

## Contents



The use of interlayers between the inorganic and the organic components of hybrid interfaces has great potential in order to engineer photovoltaic properties. Several attemps have been made in this direction, as already rewied in section 1.2. Such interlayers can reduce the charge recombination, enlarge the light absorbed spectrum and increase the compatibility between the polymer and the substrate [44, 45, 46, 47].

In this chapter we study the anchoring, energetics and assembling of a particular kind of phthalocyanine, the zinc phthalocyanine (ZnPc), on the ZnO surface. We choose ZnPcs for their tendency to aggregate on metal oxides [94] forming self-assembled monolayers strongly bound to the surface. This property allows the use of these molecules as interlayer in hybrid systems without using anchoring groups that can modify the properties of the interface.

The ternary system ZnO/ZnPc/P3HT is investigated from the morphological point of view together with the analysis of its electronic and optical properties.

## 4.1 SELF ASSEMBLING OF ZNPCS ON ZNO SURFACE

### 4.1.1 *Interaction of a single ZnPc with the ZnO surface*

The first step in our work is to create the ZnO/ZnPcs interface by MPMD. To this aim, we study first of all the attraction of a single ZnPc molecule on the ZnO surface.

Since its electronic properties will be studied at DFT level, we choose to use a ZnO surface coming from an *ab initio* optimization of a crystal slab formed by six atomic layers of bulk ZnO parallel to the $(10\bar{1}0)$ plane, and we do non relax the atoms positions during classical molecular dynamics simulations. The DFT surface, reproduce in a better way some features of the $10\bar{1}0$ ZnO wurtzite structure such as the upward shift of the oxygens in the ZnO surface dimers. The details of the theoretical method to treat this surface are reported in section A.3.

The interaction between the ZnO surface and a ZnPc molecule relaxed on it, is reported in Figure 4.1 as a function of the relative distance between molecule and surface. The bound state is characterized by the molecule at 1.96 Å from the surface with a binding energy of 2.2 eV. The molecule is slightly rotated with respect to the ZnO dimers and not perfectly planar.

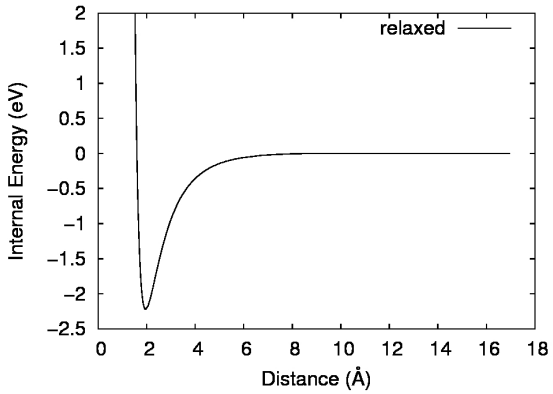


**Figure 4.1.:** *Interaction between a ZnPc molecule and the ZnO surface as a function of the distance.*

The lack of planarity in the molecule is due to the coulombic interaction between the central Zn atom of the molecule and the oxygen of the surface [4] and can be observed by relaxing the system by both DFT (Figure 4.2 left) or

MPMD (Figure 4.2 right) methods. The interaction between the molecule and the substrate vanishes at distances larger than about 8 Å. These results are in agreement with the literature [4].

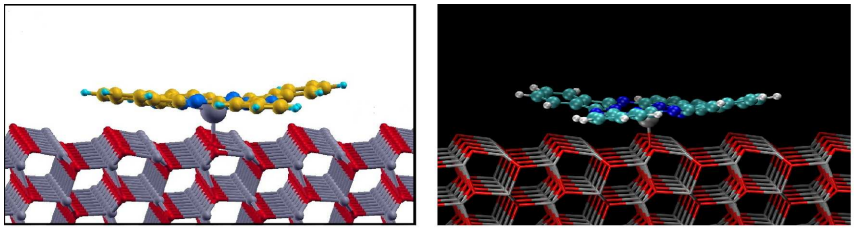

**Figure 4.2.:** *Comparison between the structure of a ZnPc molecule relaxed on the ZnO surface by performing DFT (left) or MPMD (right) calculations. (Adapted with permission from J. Phys. Chem. C, 2012, 116 (29), pp 15439-15448. Copyright 2011 American Chemical Society [4].)*

### 4.1.2 *Aggregation of ZnPc on ZnO*

The photophysics of ZnO functionalized by ZnPcs is affected by temperature, molecular concentration, and the ZnO surface morphology [94, 95, 96] and these effects are related to the tendency of Pcs to aggregate at the interface [96]. Aggregation can occur during the synthesis [97] or due to thermally activated molecule diffusion on the surface [4]. Furthermore, ZnPcs aggregates have electrochemical, spectroscopic, photophysical, and conductive properties different from those of the corresponding monomers.

Two kinds of aggregates have been identified accordingly to their optical absorption properties.

- In the J-type aggregates the molecules are parallel in a head-to-tail (HT) alignment along the [010] crystallographic direction as in Figure 4.3 left.
- The H-type aggregates, where the molecules give rise to a parallel configuration, can be further divided into two groups [94]:
  - face-to-face aligment (FF), as in Figure 4.3 middle;
  - slipped cofacial alignment (SC) as in Figure 4.3 right.

J-type aggregates give rise to red shift transitions in the absorption spectra with respect to the monomer [97], while H-types are associated with a shift toward the blue.

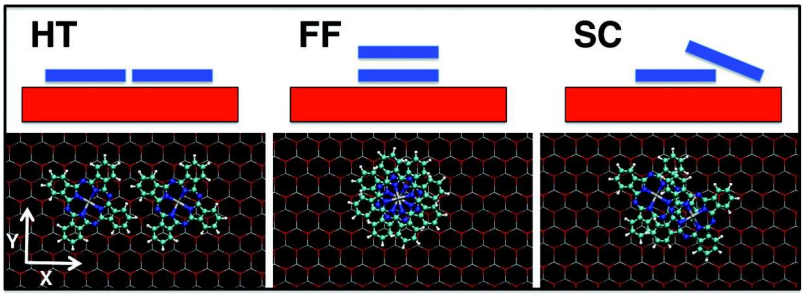


**Figure 4.3.:** *Modality of aggregation of ZnPcs on ZnO. Left: head-to-tail configuration; middle: face-to-face configuration; right: slipped cofacial configuration (Adapted with permission from ACS Nano, 2011, 5 (12), pp 9639-9647. Copyright 2011 American Chemical Society.)*

J-type aggregates turn out to be more energetically stable with respect to a face-to-face aggregation [94], due to the molecule-substrate adhesion (2.2 eV) larger than the molecule-molecule binding (1.6 eV) [94]. Therefore, the adsorption of ZnPc molecules on the ZnO surface is more likely to occur with respect to their stacking, and the formation of ZnPcs monolayers is energetically favored [94].

At room temperature the lifetime of dimers and small molecular stripes is as short as a few microseconds [94]. However, at high coverages, the aggregation involves more than 50% of molecules [94] and there are portions of ZnO that are fully covered by ZnPcs.

By assuming a fully coverage of ZnO by ZnPcs, we want to study the formation of a molecular monolayer of ZnPcs. Accordingly, we start from the single relaxed molecule (Figure 4.4, top left panel) on the ZnO surface. We create and relax a ZnPcs dimer, by putting a second molecule shifted along the [010] direction (Figure 4.4, top right panel) at a distance of $\sim 13$ Å ($4a$, where $a = 3.25$ is the ZnO lattice constant along this direction), providing the most stable configuration [94].

The relaxed dimer, can be used as building block for the ZnPcs stripes (Figure 4.4, top left panel) that, repeated periodically along the trench grooves of the ZnO, give rise

eventually to a "carpet" of ZnPcs (Figure 4.4, bottom right panel).

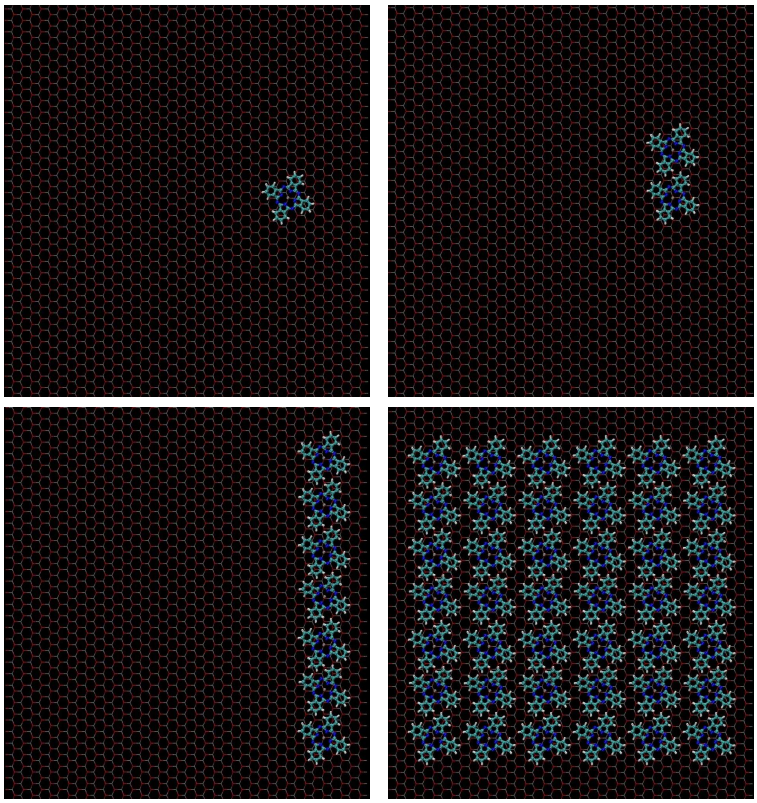

**Figure 4.4.:** *Building of a layer of ZnPcs on the ZnO surface starting from a single relaxed molecule.*

## 4.2 POLYMER INTERACTION WITH ZNPCS FUNCTIONALIZED ZINC OXIDE

Once the ZnO surface fully covered by ZnPcs is obtained, the further step is to investigate the interaction with a single polymer molecule. We want to study how the ZnPcs affects the interaction with the substrate. For this purpose we used a oligomer composed by 8 thiophenes (see Figure 4.5 left). We investigated the interaction between the polymer and the ZnO/ZnPcs surface by calculating the attraction basin reported in Figure 4.5 top right, where the energy is calculated as a function of the relative distance between the polymer and the surface.

At each distance from the substrate the energy was minimized with respect to different orientations of the molecule.

The calculated energy curve exhibits a minimum for polymer-substrate distance of about 3 Å and an interaction range of about 1 nm. By fully optimizing the minimum energy configuration we obtain the lowest energy structure of the P3HT/ZnPc/ZnO interface in which the polymer lies along the ⟨010⟩ direction above a ZnPcs stripe (see Figure 4.5). By annealing the system for 1 ns the interface is preserved, with the ZnPcs interlayer still between the polymer and the metaloxide and no diffusion of the polymer on the ZnPcs is observed. This is consistent with the strong binding of the ZnPc with ZnO that is larger than the P3HT/ZnO interaction.

Furthermore, the calculated value for the P3HT/ZnPcs interaction is comparable to the P3HT/ZnO (0.7 eV/thiophene) and much larger than the P3HT/P3HT interaction (0.1 eV/thiophene[2]). This suggests that the parallel geometry of the polymer is favored with respect to other polymer organizations at the interface, similar in the case of P3HT on the ZnO bare surface.

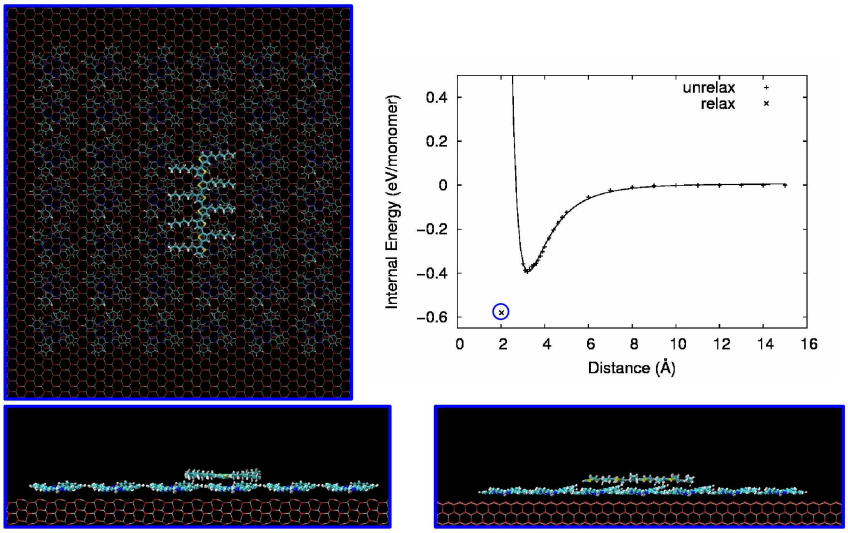


**Figure 4.5.:** *Attraction basin between the ZnO/ZnPcs interface and the P3HT oligomer and final configuration of the ternary system after the relaxation.*

## 4.3 ELECTRONIC AND OPTICAL PROPERTIES OF THE SYSTEM

### 4.3.1 *Electronic level alignment*

In this section we report a review of the electronic and optical properties of the generated ternary ZnO/ZnPc/P3HT, as in [98]. The morphology and structural properties of the system found resulting by MPMD, have been used as starting point for a DFT+U optimization. The methods used are described in section A.3.

The system studied by DFT is composed by a smaller P3HT oligomer (four thiophenes) and a portion of the previously described ZnO/ZnPc surface in properly periodic boundary conditions.

In Figure 4.6 the electronic calculations are summarized. As for the the ZnPc/ZnO and P3HT/ZnO binary systems, both are able to separate the $e - h$ pair with the electron tranferred on the metal oxide and the hole localized in the organic molecule. This behavior is confirmed by the occurence of charge transfer as a result of the interaction between the ZnPc and the substrate, found by studing the electronic ground states of a ZnPc/ZnO systems [99].

The charge transfer induces a polarization of the interface lowering the HOMO and the LUMO of the molecule with respect to the non interacting cases (compare the columns A and B and G and H in Figure 4.6). Furthermore, in the ZnPc case, a splitting of the LUMO orbitals and a mixing with the ZnO conduction band can be observed [100, 99], resulting in a favourable injection of electrons in the substrate.

The electronic properties of the ZnPc/ZnO and P3HT/ZnO systems can be further investigated by performing a open-shell Kohn-Sham (ROKS) calculation [101]. By this calculation we can obtain an approximate description of the lowest excited state of the systems by keeping fixed the occupation of the Kohn-Sham levels, in order to force the hole in the HOMO and the electron in the LUMO [99]. The results are shown in columns C (for the ZnPc/ZnO system) and F (for the P3HT/ZnO system) in Figure 4.6), and confirm the presence of the electrons within the ZnO conduction band minimum while the holes are in the ZnPc or P3HT layers.

This strong polarization of the donor-acceptor interface results in a further lowering of the HOMO and LUMO levels for the ZnPc and the P3HT [100].

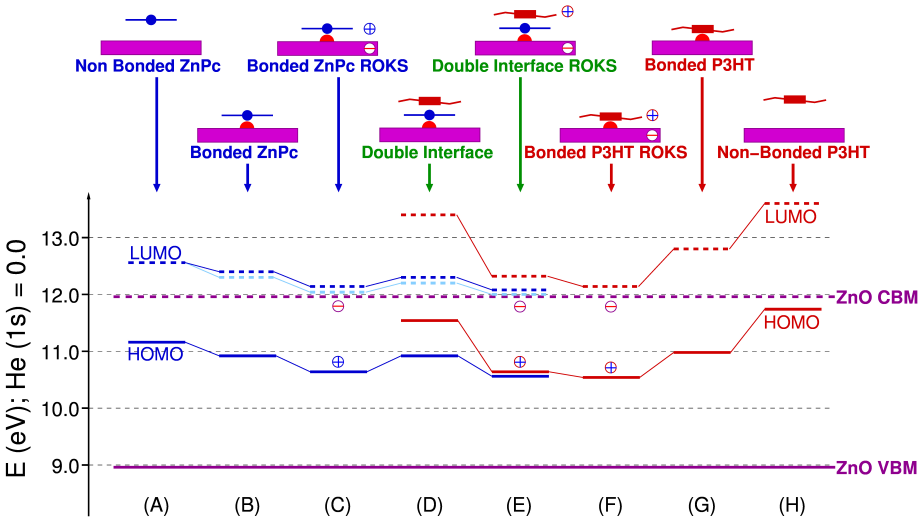


**Figure 4.6.:** *Electronic eigenvalues calculated at the* Γ *point in the case of: (A) ZnPc molecule non bonded to the ZnO surface; (B) ZnPc/ZnO interface (ground state); (C) ZnPc/ZnO interface (ROKS excited state); (D) P3HT/ZnPc/ZnO double interface (ground state); (E) P3HT/ZnPc/ZnO double interface (ROKS excited state); (F) P3HT/ZnO interface (ROKS excited state); P3HT/ZnO interface (ground state); P3HT oligomer non bonded to the ZnO surface. The electronic eigenvalues have been aligned by using the* 1*s level of a He atom inserted as a reference in all the supercells. CBM and VBM labels indicate the ZnO conduction band minimum and valence band maximum, respectively.*

When a layer of ZnPc is put between the ZnO and the P3HT, it produces a favourable alignment of the electronic ground state levels of the ternary system (see column D in Figure 4.6).

In detail, the P3HT HOMO represents the highest occupied electronic level of the ternary system, with the ZnPc HOMO placed below. The ZnO conduction band minimum represents the lowest unoccupied electronic level, followed by the ZnPc and P3HT LUMO, both falling within the ZnO conduction band.

The position of the P3HT HOMO an LUMO (column D in Figure 4.6), only slightly lower than that of the non inter-

acting oligomer (column H in Figure 4.6), indicates that the presence of the ZnPc layer, hinders the P3HT/ZnO charge recombination. The tendency of the electrons to drop into the ZnO conduction band minimum while the holes remain in the P3HT can be further confirmed by ROKS calculations (column E in Figure 4.6).

The previous analysis can be summarized as follows:

- The e-h pairs can be generated both in the ZnPc molecules and in the P3HT oligomers thanks to their comparably high absorption coefficients.
- Due to the existence of strongly mixed ZnO/ZnPc levels, the electrons reach easily the ZnO conduction band. The ZnPc HOMO is lowered (Figure 4.6, column C) but its potential energy difference with the P3HT HOMO is raised (Figure 4.6, column D), favouring the injection of the hole into the P3HT.
- The injection is supported also by the close "face-to-face" proximity of the organic moieties.
- The presence of the ZnPc interlayer causes higher potential energy of an excited electron in the P3HT LUMO (Figure 4.6, colum G) with respect to the P3HT/ZnO system (Figure 4.6, colum D). This results again in a better injection of electrons into the ZnO conduction band through the ZnPc layer.
- On the other hand, the hole transfer from the P3HT layer to the ZnPc layer is not likely to occur due to the lowering of the P3HT HOMO (Figure 4.6, colum E).

### 4.3.2 *Charge densities and recombination*

As widely discussed in chapter 1, one of the major limitations to the efficiency of hybrid interfaces is the recombination between the charges. In the ternary system here studied, the ZnPc layer act as an electronic spacer that hinders the e-h recombination. This assertion is shown in Figure 4.7, where the electrons and holes charge density (calculated by using the ROKS method) of the P3HT/ZnO and P3HT/ZnPc/ZnO systems are reported in panels C, D

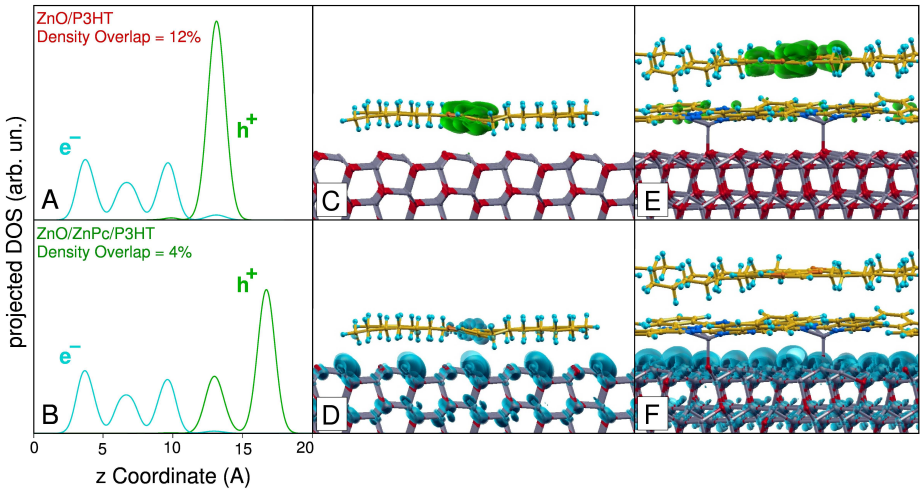


**Figure 4.7.:** *Photogenerated electron and hole displacements in the cases of binary P3HT/ZnO and ternary P3HT/ZnPc/ZnO interfaces. A (B): z-projections of the e and h charge densities in the case of a P3HT/ZnO (P3HT/ZnPc/ZnO double) interface; C and D (E and F): Electronic density plots of singly occupied ROKS orbitals, see the text, containing a photogenerated hole and electron, respectively, in the case of a P3HT/ZnO (P3HT/ZnPc/ZnO double) interface. Charge densities related to holes (electrons) are sampled at* 0.0005 (0.0001) *e/a.u.*$^3$.

and E, F. The projections of the same densities along the z axis are reported in panels A and B. In the case of the binary system, a 12% overlap between the electron and hole charge densities has been found. This overlap is mainly due to the partial electrons delocalisation on the P3HT backbone (light blue isosurface in Figure 4.7 D), while the holes are almost fully confined in the P3HT backbone (green isosurface in Figure 4.7 C). In the case of the ternary system, the overlap is reduced to 4%, due to a major localization of the electrons on the ZnO surface (light blue isosurface in Figure 4.7 F), while the holes are mainly present in the P3HT backbone, with a smaller contribution of the ZnPc layer (green isosurface in Figure 4.7 E).

### 4.3.3 *Absorption spectra*

As anticipated, an important characteristic of the ternary system under consideration are its peculiar optical proper-

ties. The absorption spectrum of the ZnPc in the gas phase is characterized by the Q band and Soret band, common to almost all phthalocyanine and porphyrin molecules, falling in the red part of the visible region (1.9 eV) and in the near UV region (3.6 eV), respectively [102].

These absorption peaks are well reproduced by TDDFPT calculations (Figure 4.8 A) and are subjected to a relevant red shift (1.7 eV for the Q band and 3.1 eV for the Soret band) when the ZnPc molecules are on the ZnO surface [99] (Figure 4.8 B). As for the P3HT, long chains in general are characterized by a strong absorption of visible light around 1.9-2.0 eV [103]. The P3HT oligomer here described presents a peak at 2.3 eV (Figure 4.8 E), which is red shifted at 2.1 eV when the P3HT interacts directly with the ZnO (Figure 4.8 D), but is found almost untouched in the ternary system (Figure 4.8 C). Therefore, the resulting optical spectrum of the ternary system (Figure 4.8 C) is characterized by three strong absorption peaks spanning all the visible light range suggesting an optimal utilization of the solar light.

## 4.4 CONCLUSIONS

In conclusion, in this chapter we have described the properties of a hybrid ternary system in which the hybrid P3HT/ZnO interface is functionalized by a optically active self-assembled organic interlayer formed by macrocyclic ZnPc molecules. We have seen that the ZnPc molecules on ZnO, results in a stable and ordered self-assembled monolayer. This molecular layer act as an active electronic spacer between polymer and the metal oxide, potentially hindering the electron-hole recombination process. Finally, the strong optical absorption of the ZnPc and P3HT, indicates a optimal sensitization of the ZnO substrate across all the visible light range.

This system is an example of a novel architecture that can be designed by a multiscale predictive modeling whose performances are currently under experimental investigation.

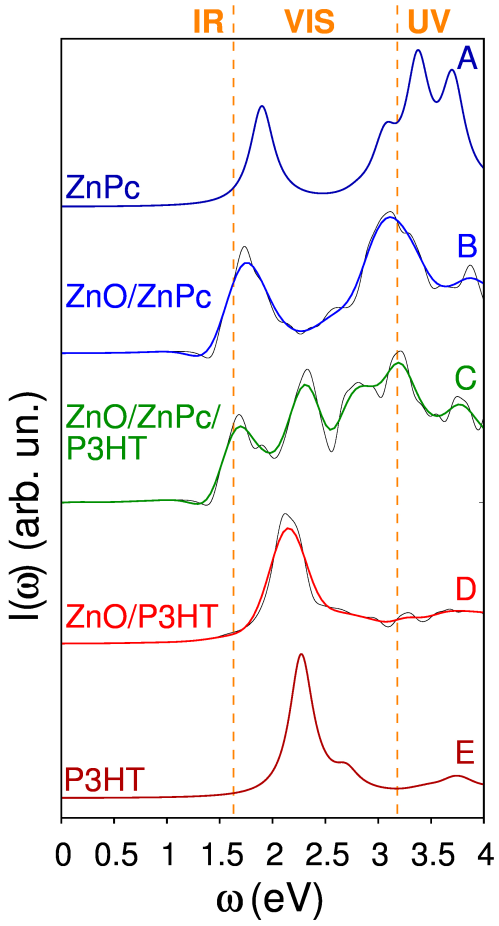


**Figure 4.8.:** *TDDFPT absorption spectra of: (A) an isolated gas-phase ZnPc molecule; (B) a ZnPc/ZnO interface; (C) a P3HT/ZnPc/ZnO double interface; (D) a P3HT/ZnO interface; (E) an isolated gas-phase P3HT oligomer. (B), (C) and (D) spectra involves the contribution of ZnO surface slabs underlying the ZnPc molecules. Such a contribution has been subtracted out from the spectra and the resulting thin black lines have been smoothed by using spline functions [5].*

# 5

# INTERACTION BETWEEN TETRAHYDROFURAN SOLVENT AND ZINC OXIDE

## Contents



## 5.1 ROLE OF THE SOLVENT IN THE SYNTHESIS OF HYBRIDS

Organic self-assembled interlayers on the electron acceptor metal oxides, can derive not only by intentional modifications (as in the case of ZnPc described in the previous chapter), but can be originated during the synthesis process.

In most cases hybrids formed by ZnO and a polymer are synthesized from solutions by dissolving the semiconductor nanostructures and the organic components into suitable solvents without the need of expensive vacuum conditions. For example, by spin-coating [104] a drop of solution containing ZnO nanorods and a conjugate polymer (such as P3HT) can be centrifugated over a substrate in air conditions (see Figure 5.1). After solvent evaporation a thin film of organic-inorganic material is deposited.

The final microstructure and the photoconversion efficiency of the corresponding hybrid strongly depend on the processing conditions. In particular, the type of solvent adopted can cause a large change (up to two orders of magnitude) in the efficiency [56].

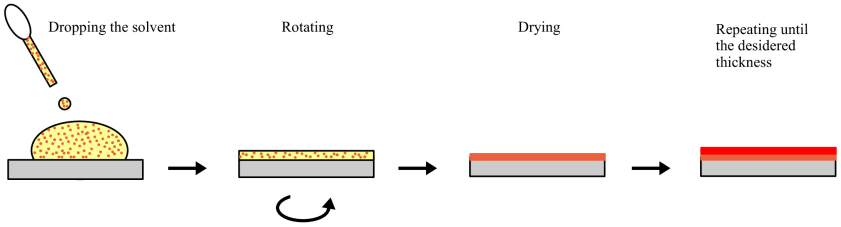


**Figure 5.1.:** *Spin-coating process. A drop of solution is placed on the substrate, which is then rotated at high speed in order to spread the fluid. Rotation is continued until the desired thickness of the film is achieved.*

Some residual solvent molecules can bind to ZnO and persist even after the syntesis process at the organic/inorganic interface. Such contaminations of the ZnO/organic interface can possibly affect the binding between the components, the interface morphology and the stability [53]; furthermore they can generate dipoles (in case of polar solvent) that eventually affect the charge separation process.

Among the solvents commonly used in combination with ZnO there are xylene, dichlorobenzene, chlorobenzene, tetrahydrofuran and chloroform. In particular, tetrahydrofuran (THF) is commonly used in the production of hybrid ZnO-based solar cells due to its low freezing point and the ability to solvate both polar and nonpolar compounds [105]. Each THF molecule consists of one oxygen and four carbon atoms (each saturated by two hydrogens as in Figure 5.2) and it exists in different isoenergetic planar and non planar configurations (e.g. twisted or envelope) [106].

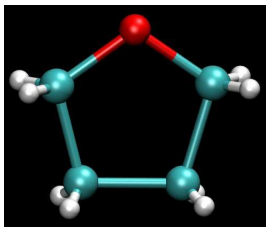

**Figure 5.2.:** *Molecule of THF in the planar configuration.*

At room temperature THF is liquid, with molecules weakly interacting through Coulombic and dispersive forces.

## 5.2 SOLVENT THF INTERACTION WITH ZNO

### 5.2.1 *Interaction between the THF molecule and the ZnO surface*

In order to investigate the THF-ZnO interaction, a single THF molecule on a ZnO surface is studied by a combination of MPMD and DFT. In particular, MPMD is used to carefully explore the space of configurations and to find the stable molecule geometry on the surface. DFT is used in order to validate and refine the MPMD result.

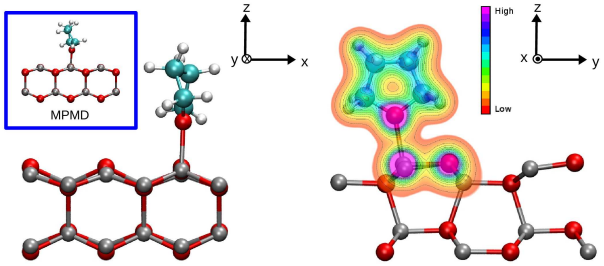


**Figure 5.3.:** *Left: Final configuration of a single THF molecule on a ZnO $(10\bar{1}0)$ surface, obtained by using DFT techniques and MPMD (inset). Right: Another perspective of the final configuration of the system, obtained by DFT calculations. Charge density isosurfaces on the (100) plane have been superimposed to the atomic configuration. (Adapted with permission from J. Phys. Chem. C, 2012, 116 (23), pp 12644-12648. Copyright 2012 American Chemical Society [6].)*

Starting from the THF molecule in different initial positions and orientations over the surface (with the carbon-oxygen ring parallel and perpendicular to it) the atomic positions are relaxed by performing MPMD simulations at low temperature followed by atomic relaxations based on the conjugate gradient method. In all cases the oxygen atom of THF binds to a zinc atom on the surface. In the lowest energy configuration, the molecule turns out to be quasi vertical with respect to the surface (see Figure 5.3, inset left panel), its plane being perpendicular to the [100] crystallographic direction. The Zn-O distance is 1.88 Å and the calculated adhesion energy is found to be as large as 1.12 eV. The interaction between the THF molecule and the ZnO as a funcion of the distance is represented in Figure 5.4.

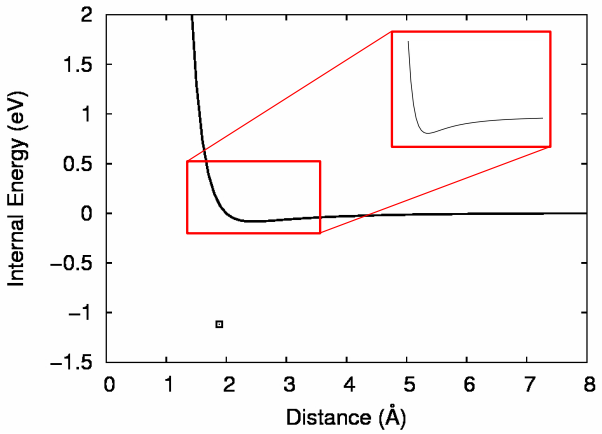


**Figure 5.4.:** *Interaction between a THF molecule and the ZnO surface.*

This molecule-surface binding is very strong as proved by 10 ns-long room temperature MPMD simulations: although several different quasi-isoenergetic configurations are indeed explored (with the molecule quasi vertical as shown in Figure 5.5 left and center or, parallel to the surface as shown in Figure 5.5 right), desorption is never observed.

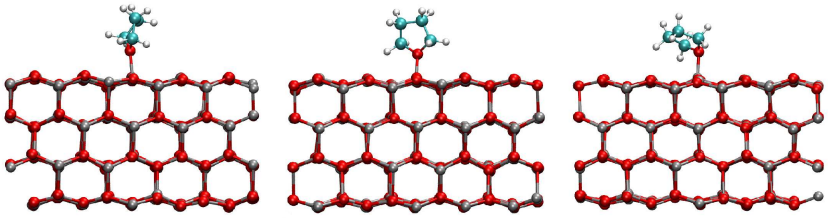

**Figure 5.5.:** *Some stable configurations of a THF molecule on the ZnO surface. (Adapted with permission from J. Phys. Chem. C, 2012, 116 (23), pp 12644-12648. Copyright 2012 American Chemical Society [6].)*

In order to validate the MPMD result, the minimum energy molecule-surface configuration (inset Figure 5.3 left) is further relaxed at DFT level (Figure 5.3 left) by using the Quantum-ESPRESSO [107] code. The method used is described in section A.3.

A Zn-O bond of length 2.1 Å due to the electrostatic interaction between the positively charged Zn and the negative oxygen of THF and a partial electronic density overlap, can be observed after the relaxation ( Figure 5.3 right

panel). Both MPMD and DFT calculation show that the molecule prefers the twist geometry with its plane slightly tilted with respect to the vertical (see Figure 5.3 left and inset). The adhesion energy, calculated by including the Grimme correction [108], is as large as 0.97 eV in nice agreement with the MPMD result (see above). This large ZnO/THF interaction turns out to be larger than both P3HT/P3HT cohesive energy (0.1 eV/thiophene) [2] and ZnO/P3HT interaction (0.7 eV/thiophene) (see chapter 3).

### 5.2.2 *Interaction between the THF liquid solvent and ZnO surface at room temperature*

In this section we consider the interaction between a THF liquid solvent and the ZnO surface at room temperature. In order to obtain a realistic model of the liquid solvent, a simple cubic crystal formed by 216 THF molecules is melted at high temperature. The liquid is then cooled down to room temperature and equilibrated in the constant-pressure, constant-temperature (NPT) ensemble at ambient conditions by using a Nosé-Hoover barostat and thermostat. The equilibrium density of the final liquid is found to be 0.879 $g/cm^3$, in agreement with previous theoretical results [106] and close to the experimental value 0.884 $g/cm^3$ [109]. A portion of this liquid is cut and merged to ZnO and the resulting solid-liquid system is equilibrated at room temperature for 0.2 ns in a simulation cell as large as 45x65x92 Å (see Figure 5.6). After few picoseconds can be observed the formation of an ordered (and hereafter stable) monolayer of THF molecules wetting the ZnO surface. Most of the molecules in the layer are stuck on the substrate as in the single molecule case, with the oxygen of THF bound to the zinc atom on the surface, suggesting that part of the THF molecules efficiently bind to ZnO during synthesis in solution.

#### 5.2.2.1 *ZnO/THF density profile*

In order to characterize the interface and its local structure, the simulated system is divided into slices along $z$ direction, setting $z = 0$ Å at the ZnO surface. For each slice is calculated the density $\rho$, obtaining the density pro-

file $\rho(z)$ reported in Figure 5.6. Far from the interface, at $z < 0$ Å and at $z > 5$ Å, $\rho(z)$ is constant and similar to the value of the ZnO crystal ($\rho_{ZnO} = 5.6$ g/cm$^3$) and that of the THF liquid ($\rho_{THF}$), respectively. The ZnO/THF interface, defined as the regions where $d\rho/dz \neq 0$, turns out to be as thin as 1 nm and it consists of the two regions labeled $C$ and $L'$ in Figure 5.6. $C$ region corresponds to the crystalline THF layer wetting the ZnO surface. $L'$ has width 0.5 nm and it corresponds to region where the liquid density is smaller than $\rho_{THF}$. A visual inspection of the molecular distribution in $L'$ shows that there is an empty space separating the wetting layer from the remaining liquid. In conclusion, the interface gives rise to a sharp transition in the THF density corresponding to an order/disorder discontinuity in the molecules distribution.

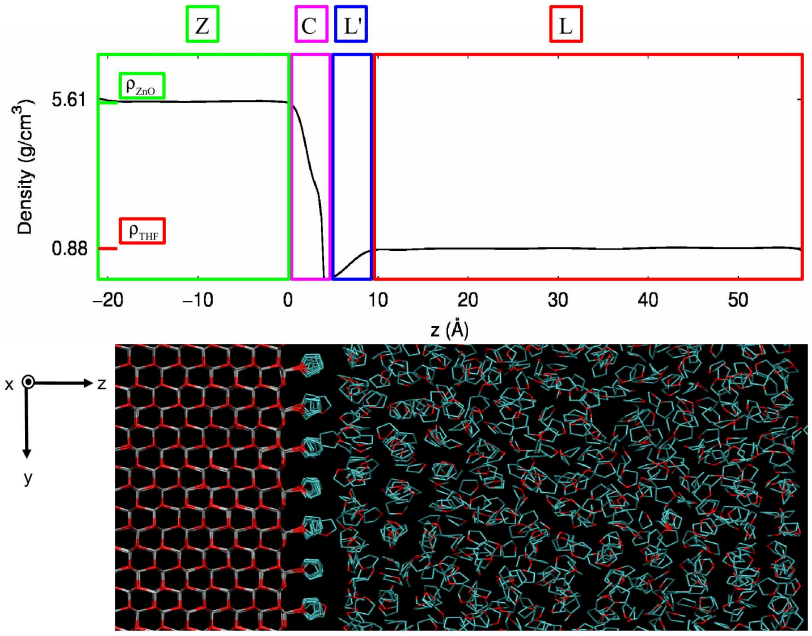


**Figure 5.6.:** *Density profile of ZnO-THF system with respect to the axys perpendicular to the surface. (For clearness in the picture we do not represent the hydrogens of THF.) (Adapted with permission from J. Phys. Chem. C, 2012, 116 (23), pp 12644-12648. Copyright 2012 American Chemical Society [6].)*

The interface between a Van der Waals liquid and a hard wall (i.e. solid a surface) has been previously studied [110]. Density fluctuations within the liquid phase are expected depending on its $\rho^*$ bulk packing density. $\rho^*$ is defined as

$\rho^* = \rho_{THF}\kappa^3$, where $\rho_{THF}$ is the liquid density, and $\kappa$ is the Van der Waals diameter of the liquid molecules. Liquids that are characterized by high bulk packing density ($\rho^* > 0.8$) show a densified region next to the substrate, followed by an oscillating exponentially decaying density profile. This is the case, for example, of cyclohexane on silicon surface, where a densified close-packed liquid layer is found at $z \sim 0.5$ nm [110]. Away from this layer a low density region of width $\sim 2$ nm follows.

The present THF/ZnO case is consistent with the above picture. The region $C$ identified in our investigation corresponds to the densified one ( i.e. wetting layer) and $L'$ to the low density region. At variance with the cyclohexane case we do not observe sizable exponential fluctuations and we attribute this behavior to the actual bonding between the molecules and the hard substrate. The THF molecules have the same orientation on the ZnO hard surface and gives rise to a softer surface composed by methylenic groups (-$CH_2$) that does not induces fluctuations on the remaining liquid.

#### 5.2.2.2 *ZnO/THF structure factors*

To further investigate the order of the system in each slice, we calculate the average structure factor (defined in chapter 2) of the oxygen atoms along the $x$ and the $y$ directions. Accordingly, in order to investigate the local crystallinity, the structure factor as a function of $\lambda = 2\pi/q$ is calculated by repeating the calculations in different regions of the system. As for the region $C$, containing the wetting THF layer, there are peaks at $\lambda = 3.25$ Å and $\lambda = 5.20$ Å for $S(\lambda)$ along the $x$ and $y$ directions, respectively. These $\lambda$ values correspond to the lattice periodicity of our ZnO surface, showing a crystalline order in the wetting layer induced by the ZnO surface. By considering the slice just above the wetting layer (region $L'$), the order is lost and a flat low-value $S(\lambda)$ profile is found (see Figure 5.7, right). The differences in the $S(\lambda)$ profiles along $x$ and $y$ directions are not sizable and it can be concluded that, except for the wetting layer, there is no order in THF even close to the interface. This analysis further confirms that, in terms of structure, the THF/ZnO interface is sharp.

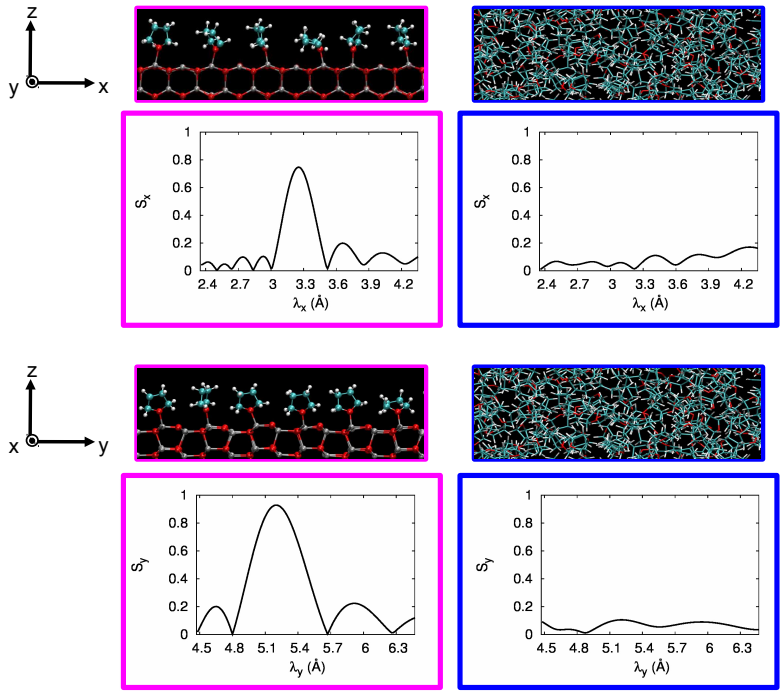


**Figure 5.7.:** *Structure factor in the x (top) and y (bottom) direction for the wetting layer C (left) and the liquid THF close to the surface L′(right). (Adapted with permission from J. Phys. Chem. C, 2012, 116 (23), pp 12644-12648. Copyright 2012 American Chemical Society [6].)*

#### 5.2.2.3 *ZnO/THF energetics*

The next analysis involves the energetics of the ZnO/THF system by calculating the adhesion energy within the system. To this aim is considered a plane (hereafter labeled as $A/B$) that divides the system into two parts, $A$ and $B$, and the work ($w$) necessary to rigidly separate them at increasing distance $z$ is calculated. At infinite distance, this work is by definition the adhesion energy $\gamma_{A/B}$ of the two parts $A$ e $B$. In the case where a molecule is cut by the plane, the whole molecule is attributed to the part ($A$ or $B$) containing its oxygen. The calculated $\gamma_{A/B}$ is directly related to energies of the generated surfaces ($\sigma_A$ and $\sigma_B$); in particular, $\gamma_{A/B} = \sigma_A + \sigma_B$. We consider three cuts (see Figure 5.6): (i) $L/L$, separating two halves of the bulk liquid; (ii) $C/L'$, separating the crystalline layer $C$ from the neighboring liquid THF layer ($L'$); (iii) $Z/C$, separating the ZnO crystalline surface ($Z$) from the wetting layer ($C$).

The $L/L$ work of separation ($w_{L/L}$) as a function of the distance is reported as red curve in Figure 5.8 and it is normalized to the asymptotic value. This work varies until the two semi-bulks are interacting. At distances larger than the interaction range ($z_0 \sim 7$ Å) the work reaches the asymptotic value $\gamma_{L/L}$. Because of the statistic distribution of molecules in the liquid phase, $\gamma_{L/L}$ is found to slightly depend on the position of the cut. For this reason we averaged the results over different cuts and we find $\gamma_{L/L} \sim 0.112$ J/m$^2$. This value is calculated without relaxing the atomic positions after the cut and it corresponds to the unrelaxed adhesion energy. If we relax the surfaces we find the relaxed adhesion energy $\gamma_{L/L}$ ($\sim 0.059$ J/m$^2$). This value corresponds to a surface tension of THF $\sigma_L = 0.030$ N/m and it can be compared with the experimental value 0.027 N/m [111].

As for the $C/L'$ (black curve of Figure 5.8), is found that $\gamma_{C/L'}$ is about 20% lower than $\gamma_{L/L}$. This means that the wetting layer locally reduces the adhesion of the liquid. In fact, as a result of the crystallinity of the W layer, all its molecules expose their hydrophobic methylene groups $CH_2$ to the liquid and the electrostatic interactions with oxygens are reduced in average. Finally, considering the $Z/C$ cut, the Zn-O bonds are broken during the separation process and $\gamma_{Z/C}$ turns out to be $\sim 0.64$ J/m$^2$, i.e. one order of magnitude higher than both $\gamma_{L/L}$ and $\gamma_{C/L'}$.

## 5.3 CONCLUSIONS

In conclusion, we have characterized the THF/ZnO interaction, finding that the strong interaction between the solvent and the surface causes the presence of a wetting crystalline (i.e. ordered) monolayer that likely persists after the drying of the solvent at room temperature. The interface between the wetting layer and ZnO is sharp in terms of density and local crystallinity and it lowers the liquid/liquid interaction close to the wetting layer. Accordingly to this analysis THF is likely present in hybrids after evaporation during the syntesis processes.

The present investigation shows the relevance of the thermodynamic molecular processes occurring at the hybrid in-

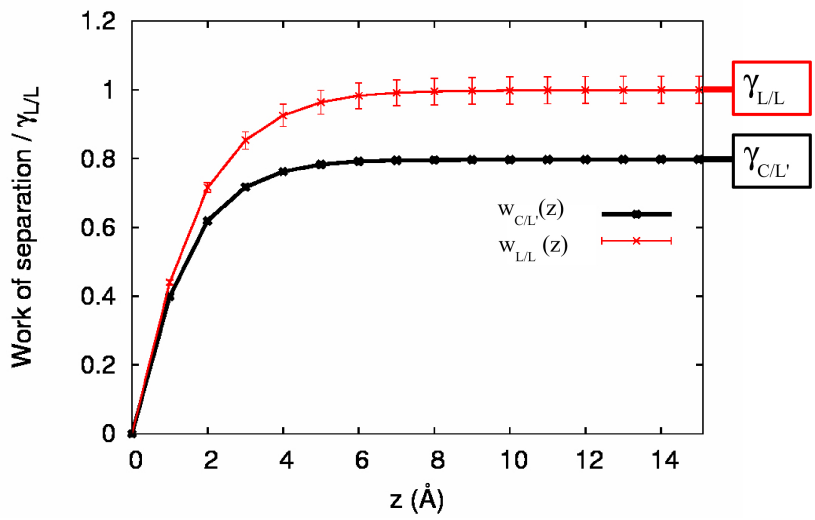


**Figure 5.8.:** *Work of separation for C/L′ (black) and L/L (red) cases. The y axis is normalized with respect to $\gamma_{L/L}$. (Adapted with permission from J. Phys. Chem. C, 2012, 116 (23), pp 12644-12648. Copyright 2012 American Chemical Society [6].)*

terface during the synthesis process. These processes must be taken into account in the modeling of real systems.

The ideas and results of this chapter are adapted with permission from J. Phys. Chem. C, 2012, 116 (23), pp 12644-12648. Copyright 2012 American Chemical Society [6].

# CONCLUSIONS

In this thesis, we have investigated the hybrid interface composed by the ZnO metal oxide and the P3HT polymer.

The physical properties of the hybrid interface have been investigated starting from the P3HT alone, going through the metal oxide/polymer interface and concluding with a ternary system where the surface was functionalized by using optically active molecules.

An additional investigation of the role of the solvent (seen as an optically inactive self-assembled layer) on the ZnO surface has been provided as well.

The results obtained highlight the importance of the structure and morphology of the polymer at the interface, that can depend on the size of the polymer nanocrystals synthesized and on the different deposition regimes. Furthermore the morphology of the binary system has been found depending on the mechanism and kinetics of assembling of the polymer on the surface. Both the model studied have highlighted the intrinsic disorder created at the interface between the polymer and the metal oxide as a result of the specific interactions between the P3HT and the ZnO and their crystal structure.

The correlation between the P3HT crystallinity and (calculated by the structure factor analysis) and the transport properties (in particular the hole mobility), has been calculated by means of an effective method based on geometrical considerations on the polymer order.

As for the hybrid ternary systems, we provided evidence that the use of optically active organic ZnPc molecules induces the formation of a stable self-assembled monolayer on the ZnO. This monolayer acts as an active electronic spacer between polymer and the metal oxide, hindering the electron-hole recombination process and allowing to obtain light absorption across all the visible spectrum, so improving PV properties of P3HT/ZnO systems.

The results presented in this thesis contribute to the understanding of the atomic scale morphology of hybrid polymer/metal oxide interfaces, only partially explored in pre-

vious literature. Present results suggest theoretical novel strategies for the improvement of hybrid systems, particularly focusing on the role of self-assembled interlayers.

# A

# MOLECULAR DYNAMICS

## A.1 MOLECULAR DYNAMICS

Molecular dynamics (MD) is a computational technique that allows to calculate the atomic trajectories of a molecular system by numerical integration of Newton's equation of motion, for a specific interatomic potential [112, 57, 58, 59].

In principle the dynamic of a system requires a quantum-mechanical treatment of constituents and the solution of the time dependent Schrödinger equation, that is possible only for extremely simple systems. Therefore, the application of approximations turns out to be essential.

The first approximation used, is that of Born-Oppenheimer [113], that takes into account the heaviness of the nuclear mass with respect to the electronic one. The motion of the nuclei and the electrons can therefore be separated and the electronic and nuclear problems can be solved with independent wavefunctions.

The second approximation is to neglet the quantomechanical effects on the atoms, considering them as classical particles. In these conditions the Newton's equation of motion $\mathbf{F} = m\mathbf{a} = -\nabla V$ can be solved by calculating the forces as gradients of the potential energy function, that depends on the atomic coordinates.

### A.1.1 *Verlet algorithm*

Even in the classical approach, due to the complicated nature of the systems, typically there is no analytical solution to their equations of motion and they must be solved numerically. In particular, in the Verlet algorithm [114] the basic idea is to write two third-order Taylor expansions for the positions $\mathbf{r}(t)$, one forward and one backward in time:

$$\mathbf{r}(t+\Delta t) = \mathbf{r}(t) + \mathbf{v}(t)\Delta t + .....(t)\Delta t^2 + (1/6)\mathbf{b}(t)\Delta t^3 + O(\Delta t^4) \tag{A.1}$$

$$\mathbf{r}(t-\Delta t) = \mathbf{r}(t) - \mathbf{v}(t)\Delta t + .....(t)\Delta t^2 - (1/6)\mathbf{b}(t)\Delta t^3 + O(\Delta t^4) \tag{A.2}$$

Adding the two expressions the position at later time is obtained:

$$\mathbf{r}(t+\Delta t) = 2\mathbf{r}(t) - \mathbf{r}(t-\Delta t) + \mathbf{a}(t)\Delta t^2 + O(\Delta t^4) \tag{A.3}$$

where $\mathbf{a}(t)$ is the force divided by the mass:

$$\mathbf{a}(t) = -(1/m)\nabla V\left(\mathbf{r}(t)\right) \tag{A.4}$$

Velocities are not directly generated. One could compute the velocities from the positions by using:

$$\mathbf{v}(t) = \frac{\mathbf{r}(t+\Delta t) - \mathbf{r}(t-\Delta t)}{2\Delta t} + O(\Delta t^2) \tag{A.5}$$

The error associated to this expression is of order $\Delta t^2$ rather than $\Delta t^4$.

A more used and efficient method for the integration of the equation of motion is the Velocity Verlet algorithm [115]. In this case the positions are calculate at time $t + \Delta t$:

$$\mathbf{r}(t+\Delta t) = \mathbf{r}(t) + \mathbf{v}(t)\Delta t + \frac{1}{2}\mathbf{a}(t)\Delta t^2 \tag{A.6}$$

The velocities are calculated at one half timestep $t + \frac{\Delta t}{2}$:

$$\mathbf{v}(t+\frac{\Delta t}{2}) = \mathbf{v}(t) + \frac{1}{2}\mathbf{a}(t)\Delta t \tag{A.7}$$

Forces and accelerations are computated at $t + \Delta t$:

$$\mathbf{a}(t+\Delta t) = -(\frac{1}{m})\nabla V\left(\mathbf{r}(t+\Delta t)\right) \tag{A.8}$$

At last, we obtain the velocity at the time $t + \Delta t$:

$$\mathbf{v}(t+\Delta t) = \mathbf{v}(t+\frac{\Delta t}{2}) + \frac{1}{2}\mathbf{a}(t+\Delta t)\Delta t \tag{A.9}$$

The Velocity Verlet algorithm has the advantage to be stable and to allow the use of relatively large timesteps (1 fs for most of the calculations in this thesis), requiring a lower computational time.

### A.1.2 *The thermodynamic ensembles*

The correct numerical integration of the Newton's equation of motion must provide the conservation of the total energy of the system (potential plus kinetic energy). If the system is composed by a constant number of particles $N$, it has a constant volume $V$ and a constant energy $E$, the statistical system (ensemble) is called microcanonical (NVE).

If the simulation requires constant temperature o pressure, different ensembles can be used. In a canonical ensemble (NVT) the temperature is fixed by coupling the system with a thermal bath (the energy fluctuating around the average value). In a NPT ensemble also the pressure is kept constant by using a suitable barostat.

### A.1.3 *Temperature control*

Since, tipically, the stability and the control of the temperature is a key issue in a simulation, is important to find a method to control it. The temperature of the system can be related to the microscopic quantity of the system by the equipartition energy theorem

$$\frac{1}{2}\sum_{i}^{N} m_i v_i^2 = \frac{1}{2} N_f k_B T \tag{A.10}$$

The temperature $T$ can be expressed as function of the atomic velocities

$$T = \frac{1}{N_f k_B T}\sum_{i}^{N} m_i v_i^2 \tag{A.11}$$

where $N$ is the number of atoms, $N_f$ is the number of degrees of freedom, $k_B$ is the Boltzmann constant and $m_i$ and $v_i$ are the mass and the velocity of the atom $i$. For a molecule composed by $N$ atoms the total degrees of freedom are $N_f = 3N - N_b$ where $N_b$ is the number of the bonds.

A rough method to control the temperature in a MD simulation is given by the velocity rescaling method. If the temperature at the time $t$ is $T(t)$, it is possible to drive the system to a target temperature $T_0$ by rescaling the veloc-

ities by a factor $\lambda$. The associated temperature change is calculated as:

$$\Delta T = \frac{1}{2}\sum_{i=1} 2\frac{m_i(\lambda v_i)^2}{Nk_B} - \frac{1}{2}\sum_{i=1} 2\frac{m_i v_i^2}{Nk_B} \tag{A.12}$$

$$\Delta T = (\lambda^2 - 1)T(t) \tag{A.13}$$

$$\lambda = \sqrt{T_0/T(t)} \tag{A.14}$$

Unfortunally, with this method the fluctuations of the kinetic energy of the system are suppressed and the trajectories produced are not consistent with the canonical ensemble.

A better method to control the temperature is the Berendsen approach [116] that consists in coupling the system with an external heat bath at fixed temperature $T_0$. The velocities are scaled accordingly to the following equation:

$$\frac{dT(t)}{dt} = \frac{T_0 - T(t)}{\tau} \tag{A.15}$$

where $\tau$ is a time constant. The temperature change after one timestep is

$$\Delta T = \frac{\delta t}{\tau}(T_0 - T(t)) \tag{A.16}$$

where $\delta t$ is the integration step. Putting the Equation A.13 in the Equation A.16 it is found:

$$(\lambda^2 - 1)T(t) = \frac{\delta t}{\tau}((T_0 - T(t)) \tag{A.17}$$

Finally, the scaling factor $\lambda^2$ is:

$$\lambda = \sqrt{1 + \frac{\delta t}{\tau}(\frac{T_0}{T(t)} - 1)} \tag{A.18}$$

The correct choice of $\tau$ is very important. In fact, the limit $\tau = \delta t$ brings back the velocity rescaling method while for $\tau \to \infty$ the dynamics will sample the microcanonical ensemble and the Berendsen approach would be ineffective.

Finally, $\tau$ too small produces unrealistical low temperature fluctuations. A typical and efficient choice for $\tau$ is $\sim 100\delta t$.

The Nosé Hoover [117, 118] approach is an improvement of the Berendsen method in which an extra degree of freedom $s$ is introduced. This new variable is associated with a "mass" $Q$ that determines the coupling between the bath and the real system controlling the temperature fluctuations.

### A.1.4 *Periodic Boundary Conditions (PBC)*

In order to minimize the number of atoms in a simulation and to avoid surface effects, the Periodic Boundary Conditions (PBC) can be introduced. They allow to simulate a finite system in a cell periodically repeated in the three directions of the space. Each particle interact with the other particles in the cell and with the others in the image cells within the cutoff distance, thus simulating an infinite system.

## A.2 THE FORCE FIELD

The critical requirement for MD is the choice of a suitable potential that well describes the physical properties of the material of interest. Model Potential Molecular Dynamics (MPMD) makes use of empirical potentials, whose parameters, obtained by experiments or ab initio calculations, are fitted to reproduce the physical properties of the system considered.

Among the more common force fields there are AMBER [60], CHARMM [119], Gromos [120] and OPLS [25].

In this work the calculation for the organic components have been performed by using the AMBER (Assisted Model Building Refinement) force field, particular suitable for the study of organic materiasl. The Amber force field considers two kind of interactions: the bonded and the non-bonded [60].

### A.2.1 *Bonded interaction*

The bondend interactions involved three contributions [60]:

$$U_{bonded} = U_{bonds} + U_{angles} + U_{dihedrals} \tag{A.19}$$

$U_{bonds} = \sum \frac{1}{2} K_b (r - r_0)^2$ describes the energy between covalently bonded atoms. $K_b$ is the constant of the force, $r_0$ is the equilibrium distance between two atoms and $r$ is the lenght of the bond (Figure A.2 top left).

$U_{angle} = \sum \frac{1}{2} K_a (\theta - \theta_0)^2$ describes the energy due to the deformation of the angle formed by the three particles. $K_a$ is the constant of the force and $\theta_0$ is the equilibrium angle between the atoms and $r$ is the lenght of the bond (Figure A.2 top right).

$U_{dihedral} = \sum \frac{1}{2} V_\phi (1 + cos(n\phi - \phi_0)$ represents the potential due to the torsion angles. The energy is linked at the rotation around a bond. $V_\phi$ is a constant that defines the rotation barrier around the bond, $\phi_0$ is the equilibrium dihedral angle and $n$ is the multiplicity of the torsions (Figure A.2 bottom).

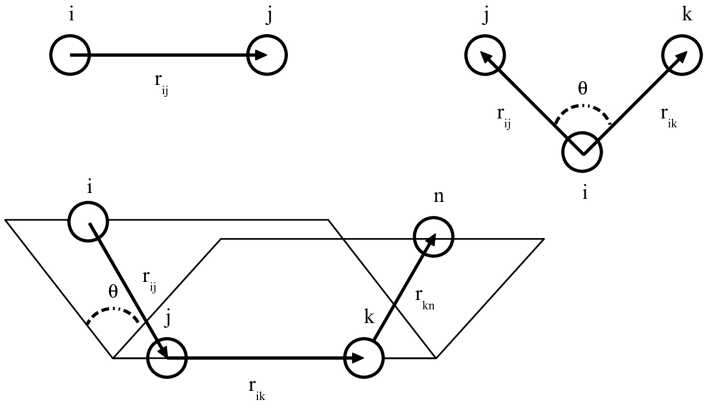


**Figure A.1.:** *Bonding (top left), angular (top right) and dihedral (bottom) interaction between two, three and four atoms.*

### A.2.2 *Non-bonded interaction*

The non-bonded interaction involves the atoms not chemically bonded or separated by three o more bonds. It is the sum between the Coulombic attraction and the van der

Waals interaction modelled on the Lennard-Jones potential [121] :

$$U_{non-bonded} = U_{vdW} + U_{Coul} = \sum 4\epsilon_{ij}\left(\frac{\sigma_{ij}}{r_{ij}}^{12} - \frac{\sigma_{ij}}{r_{ij}}^{6}\right) + \sum \frac{q_i q_j}{4\pi\epsilon_0 r_{ij}} \tag{A.20}$$

where $\epsilon$ is the depth of the potential well, $\sigma$ is the finite distance at which the inter-particle potential is zero and $r_{ij}$ is the distance between the particles. The repulsive term describes the Pauli repulsion at short ranges due to overlapping electron orbitals, while the attractive long-range term describes the attraction at long ranges (dispersion force).

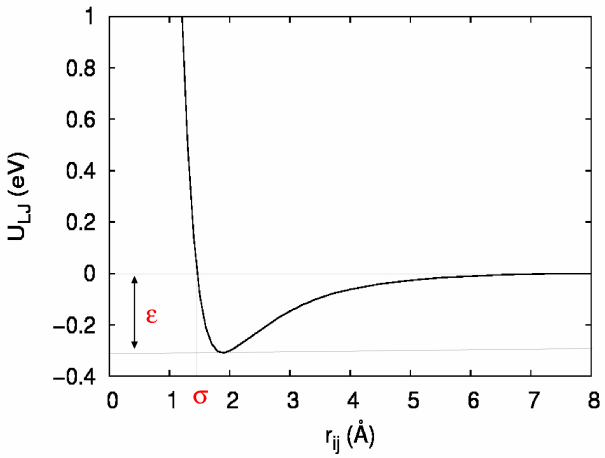


**Figure A.2.:** *Example of Lennard-Jones type potential for two atoms.*

The interaction between the metal oxide are calculated by using the Buckingam potential [62, 70]:

$$U_{buck} = A\exp\left(-\frac{r_{ij}}{B}\right) - \frac{C}{r_{ij}^6} \tag{A.21}$$

where $A$, $B$ and $C$ are parameters fitted in order to reproduce experimental data.

The non-bonded interaction are the more computationally expensive, with the time calculation proportional to the square of the number of atoms, $N^2$, than to $N$ as in the case of the bonded contributions.

An efficient method to spare computational time is represented by the Ewald sum [122]. In this method each point charge is surrounded by a charge distribution of the same

magnitude and opposite sign that spreads out radially from the point charge up to a cutoff distance with a Gaussian distribution. The interaction is separated in two contribution: the short-range, representing the screening interaction between neighboring charges, is calculated in the real space, while the long-range, representing the cancelling charge distribution of the same sign as the original charge, is calculated in the reciprocal Fourier space where the convergence is faster [58]. By using the Ewald summation, the computational workload scales as $N \log(N)$ instead than as $N^2$.

## A.3 METHODS

In this section we describe the specific technicalities used in the symulations of the present thesis.

The MPMD calculation performed in chapter 2, chapter 3 and chapter 4 have been performed by using the DL_POLY code [123], while in chapter 5 we used the Lammps code [124]. Some of the trajectories are analyzed by using the VMD molecular visualization program [125].

The protocol for the relaxation of the systems consists in low temperature annealings (0.1 ns at 1K) followed by atomic forces relaxations based on standard conjugated gradients algorithm [126]. The calculations at room temperature have been performed by using the NVT or the NPT ensemble, in particular the Nosé-Hoover thermostat and barostat [117, 118].

Interactions within ZnO have been described as the sum of Coulomb and a Buckingham-type two-body potential [70, 127]. As for P3HT, the THF and the ZnPC we adopted the AMBER force field [60], including both bonding and nonbonding contributions. For hybrid interactions, we used a sum of Coulomb and Lennard-Jones contributions [42]. The velocity Verlet algorithm [115] with a time step of 1.0 fs has been used to solve the equations of motion. The atomic partial charges has been calculated according to the standard AM1-BCC method [128]. A mesh Ewald algorithm [122] has been used for the long-range electrostatic forces and the Van der Waals interactions have been cutoff at 9.5 Å.

In chapter 3, first-principles calculations for the transport properties have been performed within Density Functional Theory (DFT) level. The estimate of the electronic coupling for cofacial dimers has been obtained using the so-called "energy splitting in dimer" method [93]. In this method the transfer integral for holes can be computed evaluating the energy difference between the orbitals resulting from the overlap of the highest occupied molecular orbitals of the two interacting molecules: $J_{\alpha\beta} = (\epsilon_{HOMO} - \epsilon_{HOMO-1})/2$, where $\epsilon_{HOMO}$ and $\epsilon_{HOMO-1}$ are the energies of the two highest occupied molecular orbitals of the dimer. We used the gradient-corrected PBE density-functional [129] together with a plane-wave basis set and ultrasoft pseudopotentials as implemented in the CPMD [130] program package; to account for dispersion interactions we used the empirical dispersion correction proposed by Grimme [108], that adds a Van der Waals-type term scaling as $R^{-6}$ into the total energy of the system.

As for the *ab initio* methods used in chapter 4, DFT+U calculations have been performed by using the Quantum-ESPRESSO package[107]. Total energies have been calculated by using ultrasoft pseudopotentials[131], by expanding Kohn-Sham eigenfunctions on a plane-wave basis set. The cutoff has been set at 35 Ry on the plane waves and at 280 Ry on the electronic density. The electronic properties of the ZnO/P3HT system, of the ZnO/ZnPc system, and of the double-interface ZnO/ZnPc/P3HT system have been investigated by analyzing the electronic eigenvalues calculated at the $\Gamma$ point. The exchange-correlation functional has been obtained by adding an *ab initio* non-local van der Waals correlation contribution[132, 133] to the semilocal gradient-corrected PBE functional[129]. An Hubbard U correction [134, 135] has been applied to the Zn $3d$ and O $2p$ atomic shells, thus allowing for an optimal position of ZnO band edges with respect to the molecule and polymer HOMO-LUMO levels. A P3HT oligomer, formed by four monomers has been used to simulate the properties of the polymer. Finally, optical absorption spectra ranging from the near-IR to the near-UV regions have been calculated by using a recent approach to the solution of the Bethe-Salpeter equation within the framework of time-dependent density matrix perturbation theory (TDDFPT) [136, 137].

In chapter 5, the interaction between the single THF molecule and the ZnO surface at DFT level have been perfomed by using the Quantum-ESPRESSO [107] code. We used Vanderbilt ultrasoft pseudopotentials with the Perdew-Burke-Ernzerhof (PBE) version of the generalized gradient approximation (GGA) exchange-correlation functional [129] . Kohn-Sham eigenfunctions have been expanded on a plane-wave basis set by using cutoffs of 30 Ry on the plane waves and of 300 Ry on the electronic density. The Grimme [108] correction has been used to include the effects of dispersion interactions. In addition to the 13 atoms of the THF, the surface cell contained a 3x2 slab formed by 4 atomic layers of ZnO (48 atoms) and 30 Å of empty space. The electronic properties of the system have been investigated by analyzing the electronic eigenvalues calculated at the Γ point.

# BIBLIOGRAPHY


[1] http://www.orgworld.de/. (Cited on pages xi and 5.)

[2] C. Melis, L. Colombo, and A. Mattoni, "Self-assembling of poly(3-hexylthiophene)," *The Journal of Physical Chemistry C*, vol. 115, no. 2, pp. 576–581, 2011. (Cited on pages xi, xii, 15, 16, 17, 18, 19, 20, 21, 25, 33, 34, 52, and 63.)

[3] M. I. Saba, C. Melis, L. Colombo, G. Malloci, and A. Mattoni, "Polymer crystallinity and transport properties at the poly(3-hexylthiophene)/zinc oxide interface," *The Journal of Physical Chemistry C*, vol. 115, no. 19, pp. 9651–9655, 2011. (Cited on pages xiv, 43, and 46.)

[4] C. Melis, L. Colombo, and A. Mattoni, "Adhesion and diffusion of zinc-phthalocyanines on the zno $(10\bar{1}0)$ surface," *The Journal of Physical Chemistry C*, vol. 115, no. 37, pp. 18208–18212, 2011. (Cited on pages xiv, 11, 48, and 49.)

[5] C. H. Reinsch, "Smoothing by spline functions," *Num. Math.*, vol. 10, pp. 177–183, 1967. (Cited on pages xvi and 58.)

[6] M. I. Saba, V. Calzia, C. Melis, L. Colombo, and A. Mattoni, "Atomistic investigation of the solid–liquid interface between the crystalline zinc oxide surface and the liquid tetrahydrofuran solvent," *The Journal of Physical Chemistry C*, vol. 116, no. 23, pp. 12644–12648, 2012. (Cited on pages xvi, xvii, 11, 61, 62, 64, 66, and 68.)

[7] M. A. Green, K. Emery, Y. Hishikawa, W. Warta, and E. D. Dunlop, "Solar cell efficiency tables (version 39)," *Progress in Photovoltaics: Research and Applications*, vol. 20, no. 1, pp. 12–20, 2012. (Cited on page 1.)

[8] M. Wright and A. Uddin, "Organic-inorganic hybrid solar cells: A comparative review," *Solar Energy Ma-*

*terials and Solar Cells*, vol. 107, no. 0, pp. 87–111, 2012. (Cited on pages 1 and 2.)

[9] H. Hoppe and N. S. Sariciftci, "Organic solar cells: An overview," *Journal of Materials Research*, vol. 19, pp. 1924–1945, 6 2004. (Cited on page 1.)

[10] R. Janssen, *Introduction to polymer solar cells*. Eindhoven University of Technology, The Netherlands, 2007. (Cited on pages 1, 3, 4, and 8.)

[11] M. Pope and C. E. Swenberg, *Electronic processes in organic crystals and polymers*. Oxford University Press, 1999. (Cited on page 1.)

[12] C. Deibel and V. Dyakonov, "Polymer-fullerene bulk heterojunction solar cells," *Rep. Prog. Phys.*, vol. 73, p. 096401, 2010. (Cited on pages 2, 3, and 4.)

[13] K. M. Coakley, B. S. Srinivasan, J. M. Ziebarth, C. Goh, Y. Liu, and M. D. McGehee, "Enhanced hole mobility in regioregular polythiophene infiltrated in straight nanopores," *Advanced Functional Materials*, vol. 15, no. 12, pp. 1927–1932, 2005. (Cited on page 2.)

[14] F. C. Krebs, "Fabrication and processing of polymer solar cells: A review of printing and coating techniques," *Solar Energy Materials and Solar Cells*, vol. 93, no. 4, pp. 394 – 412, 2009. (Cited on page 2.)

[15] T. T. Larsen-Olsen, B. Andreasen, T. R. Andersen, A. P. Böttiger, E. Bundgaard, K. Norrman, J. W. Andreasen, M. Jørgensen, and F. C. Krebs, "Simultaneous multilayer formation of the polymer solar cell stack using roll-to-roll double slot-die coating from water," *Solar Energy Materials and Solar Cells*, vol. 97, no. 0, pp. 22 – 27, 2012. (Cited on page 2.)

[16] J. D. Servaites, M. A. Ratner, and T. J. Marks, "Organic solar cells: A new look at traditional models," *Energy Environ. Sci.*, vol. 4, pp. 4410–4422, 2011. (Cited on page 2.)

[17] R. Smalley, "Discovering the fullerenes," *Rev. Mod. Phys.*, vol. 69, no. 3, p. 723, 1997. (Cited on page 2.)

[18] H. Spanggaard and F. C. Krebs, "A brief history of the development of organic and polymeric photovoltaics," *Solar Energy Materials and Solar Cells*, vol. 83, pp. 125–146, 2004. (Cited on page 2.)

[19] L. Groenendaal, F. Jonas, D. Freitag, H. Pielartzik, and J. R. Reynolds, "Poly(3,4-ethylenedioxythiophene) and its derivatives: Past, present, and future," *Advanced Materials*, vol. 12, no. 7, pp. 481–494, 2000. (Cited on page 2.)

[20] Z. Su, L. Wang, Y. Li, H. Zhao, B. Chu, and W. Li, "Ultraviolet-ozone-treated pedot:pss as anode buffer layer for organic solar cells," *Nanoscale Research Letters*, vol. 7, no. 1, p. 465, 2012. (Cited on page 2.)

[21] T. J. Savenije, *Organic Solar Cells*. Delft University of Technology. (Cited on pages 2, 5, 6, and 7.)

[22] J. M. Szarko, J. Guo, B. S. Rolczynski, and L. X. Chen, "Current trends in the optimization of low band gap polymers in bulk heterojunction photovoltaic devices," *J. Mater. Chem.*, vol. 21, pp. 7849–7857, 2011. (Cited on page 5.)

[23] Z. He, C. Zhong, X. Huang, W.-Y. Wong, H. Wu, L. Chen, S. Su, and Y. Cao, "Simultaneous enhancement of open-circuit voltage, short-circuit current density, and fill factor in polymer solar cells," *Advanced Materials*, vol. 23, no. 40, pp. 4636–4643, 2011. (Cited on page 5.)

[24] http://www.heliatek.com/. (Cited on page 5.)

[25] W. L. Jorgensen and J. Tirado-Rives, "The opls [optimized potentials for liquid simulations] potential functions for proteins, energy minimizations for crystals of cyclic peptides and crambin," *Journal of the American Chemical Society*, vol. 110, no. 6, pp. 1657–1666, 1988. (Cited on pages 6 and 75.)

[26] U. Özgür, Y. I. Alivov, C. Liu, A. Teke, M. A. Reshchikov, S. Doğan, V. Avrutin, S.-J. Cho, and H. Morkoç, "A comprehensive review of zno materials and devices," *Journal of Applied Physics*, vol. 98, no. 4, p. 041301, 2005. (Cited on pages 6 and 30.)

[27] S. D. Oosterhout, M. Wienk, S. S. van Bavel, R. Thiedmann, L. J. A. Koster, J. Gilot, J. Loos, V. Schmidt, and R. A. J. Janssen, "The effect of three-dimensional morphology on the efficiency oh hybrid polymer solar cells," *Nature Materials*, vol. 8, pp. 818–824, 2009. (Cited on pages 6 and 29.)

[28] B. O'Regan and B. Grätzel, "A low-cost, high-efficiency solar cell based on dye-sensitized colloidal tio2 films," *Nature*, vol. 353, pp. 737–740, 1991. (Cited on page 6.)

[29] M. Grätzel, "Dye-sensitized solar cells," *Journal of Photochemistry and Photobiology C: Photochemistry Reviews*, vol. 4, no. 2, pp. 145–153, 2003. (Cited on page 6.)

[30] F. Fabregat-Santiago, J. Bisquert, L. Cevey, P. Chen, M. Wang, S. M. Zakeeruddin, and M. Grätzel, "Electron transport and recombination in solid-state dye solar cell with spiro-ometad as hole conductor," *J. Am. Chem. Soc.*, vol. 131, pp. 558–562, 2009. (Cited on page 6.)

[31] B. E. Hardin, H. J. Snaith, and M. D. Mcgehee, "The renaissance of dye-sensitized solar cells," *Nature Photon*, vol. 6, pp. 162–169, 2012. (Cited on pages 6 and 7.)

[32] J. Burschka, A. Dualeh, F. Kessler, E. Baranoff, N.-L. Cevey-Ha, C. Yi, M. K. Nazeeruddin, and M. Grätzel, "Tris(2-(1h-pyrazol-1-yl)pyridine)cobalt(iii) as p-type dopant for organic semiconductors and its application in highly efficient solid-state dye-sensitized solar cells," *J. Am. Chem. Soc.* (Cited on page 6.)

[33] A. Yella, H.-W. Lee, H. N. Tsao, C. Yi, A. K. Chandiran, M. Nazeeruddin, E. W.-G. Diau, C.-Y. Yeh, S. M. Zakeeruddin, and M. Grätzel, "Porphyrin-sensitized solar cells with cobalt (ii/iii)–based redox electrolyte exceed 12 percent efficiency," *Science*, vol. 334, p. 629, 2011. (Cited on page 7.)

[34] M. G. Waltera, A. B. Rudineb, and C. C. Wamserb, "Porphyrins and phthalocyanines in solar photo-

voltaic cells," *J. Porphyrins Phthalocyanines*, 2010. (Cited on page 7.)

[35] T. C. Li, M. S. Góes, F. Fabregat-Santiago, J. Bisquert, P. R. Bueno, C. Prasittichai, J. T. Hupp, and T. J. Marks, "Surface passivation of nanoporous tio2 via atomic layer deposition of zro2 for solid-state dye-sensitized solar cell applications," *J. Phys. Chem. C*, vol. 113, pp. 18385–18390, 2009. (Cited on page 7.)

[36] M. T. Lloyd, R. P. Prasankumar, M. B. Sinclair, A. C. Mayer, D. C. Olson, and J. W. P. Hsu, "Impact of interfacial polymer morphology on photoexcitation dynamics and device performance in p3ht/zno heterojunctions," *J. Mater. Chem.*, vol. 19, pp. 4609–4614, 2009. (Cited on pages 8 and 9.)

[37] J. W. Hsu and M. T. Lloyd, "Organic/inorganic hybrids for solar energy generation," *MRS Bulletin*, vol. 35, pp. 422–428. (Cited on page 8.)

[38] F. C. Spano, "Modeling disorder in polymer aggregates: The optical spectroscopy of regioregular poly(3-hexylthiophene) thin films," *The Journal of Chemical Physics*, vol. 122, no. 23, p. 234701, 2005. (Cited on page 8.)

[39] J. Veres, S. Ogier, G. Lloyd, and D. de Leeuw, "Gate insulators in organic field-effect transistors," *Chemistry of Materials*, vol. 16, no. 23, pp. 4543–4555, 2004. (Cited on page 8.)

[40] R. Kline, M. McGehee, and M. Toney, "Highly oriented crystals at the binterface in polythiophene thin-film transistors," *Nat. Mater*, vol. 5, pp. 222–228, 2006. (Cited on page 8.)

[41] P. Reiss, E. Couderc, J. De Girolamo, and A. Pron, "Conjugated polymers/semiconductor nanocrystals hybrid materials-preparation, electrical transport properties and applications," *Nanoscale*, vol. 3, pp. 446–489, 2011. (Cited on page 8.)

[42] C. Melis, A. Mattoni, and L. Colombo, "Atomistic investigation of poly(3-hexylthiophene) adhesion on

nanostructured titania," *The Journal of Physical Chemistry C*, vol. 114, no. 8, pp. 3401–3406, 2010. (Cited on pages 8, 9, and 78.)

[43] A. Mang, K. Reimann, and S. Rübenacke, "Band gaps, crystal-field splitting, spin-orbit coupling, and exciton binding energies in zno under hydrostatic pressure," *Solid State Communications*, vol. 94, no. 4, pp. 251–254, 1995. (Cited on page 9.)

[44] Y.-Y. Lin, T.-H. Chu, S.-S. Li, C.-H. Chuang, C.-H. Chang, W.-F. Su, C.-P. Chang, M.-W. Chu, and C.-W. Chen, "Interfacial nanostructperformance of polymer/tio2 nanorod bulk heterojunction solar cells," *J. Am. Chem. Soc.*, vol. 131, no. 10, pp. 3644–3649, 2009. (Cited on pages 9 and 47.)

[45] Z. Li, X. Zhang, and G. Lu, "Dipole-assisted charge separation in organic–inorganic hybrid photovoltaic heterojunctions: Insight from first-principles simulations," *The Journal of Physical Chemistry C*, vol. 116, no. 18, pp. 9845–9851, 2012. (Cited on pages 9, 10, and 47.)

[46] C. Goh, S. R. Scully, and M. D. McGehee, "Effects of molecular interface modification in hybrid organic-inorganic photovoltaic cells," *J. Appl. Phys.*, vol. 101, no. 11, p. 114503, 2007. (Cited on pages 9, 10, and 47.)

[47] E. V. Canesi, M. Binda, A. Abate, S. Guarnera, L. Moretti, V. D'Innocenzo, R. Sai Santosh Kumar, C. Bertarelli, A. Abrusci, H. Snaith, A. Calloni, A. Brambilla, F. Ciccacci, S. Aghion, F. Moia, R. Ferragut, C. Melis, G. Malloci, A. Mattoni, G. Lanzani, and A. Petrozza, "The effect of selective interactions at the interface of polymer-oxide hybrid solar cells," *Energy Environ. Sci.*, vol. 5, pp. 9068–9076, 2012. (Cited on pages 9, 10, and 47.)

[48] F. Risplendi, G. Cicero, G. Mallia, and N. M. Harrison, "A quantum-mechanical study of the adsorption of prototype dye molecules on rutile-tio2(110): a comparison between catechol and isonicotinic acid," *Phys. Chem. Chem. Phys.*, vol. 15, pp. 235–243, 2013. (Cited on page 10.)

[49] R. Mosurkal, J.-A. He, K. Yang, L. A. Samuelson, and J. Kumar, "Organic photosensitizers with catechol groups for dye-sensitized photovoltaics," *Journal of Photochemistry and Photobiology A: Chemistry*, vol. 168, no. 3, pp. 191 – 196, 2004. (Cited on page 10.)

[50] C. R. Rice, M. D. Ward, M. K. Nazeeruddin, and M. Grätzel, "Catechol as an efficient anchoring group for attachment of ruthenium-polypyridine photosensitisers to solar cells based on nanocrystalline tio2 films," *New J. Chem.*, vol. 24, pp. 651–652, 2000. (Cited on page 10.)

[51] P. Persson, R. Bergström, and S. Lunell, "Quantum chemical study of photoinjection processes in dye-sensitized tio2 nanoparticles," *The Journal of Physical Chemistry B*, vol. 104, no. 44, pp. 10348–10351, 2000. (Cited on page 10.)

[52] W. R. Duncan and O. V. Prezhdo, "Electronic structure and spectra of catechol and alizarin in the gas phase and attached to titanium," *The Journal of Physical Chemistry B*, vol. 109, no. 1, pp. 365–373, 2005. (Cited on page 10.)

[53] J. A. Chang, J. H. Rhee, S. H. Im, Y. H. Lee, H.-j. Kim, S. I. Seok, M. K. Nazeeruddin, and M. Grätzel, "High-performance nanostructured inorganic - organic heterojunction solar cells," *Nano Lett.*, vol. 10, no. 7, pp. 2609–2612, 2010. (Cited on pages 10 and 60.)

[54] A. W. Hains, Z. Liang, M. A. Woodhouse, and B. A. Gregg, "Molecular semiconductors in organic photovoltaic cells," *Chemical Reviews*, vol. 110, no. 11, pp. 6689–6735, 2010. (Cited on pages 10 and 11.)

[55] S.-J. Moon, E. Baranoff, S. M. Zakeeruddin, C.-Y. Yeh, E. W.-G. Diau, M. Grätzel, and K. Sivula, "Enhanced light harvesting in mesoporous tio2/p3ht hybrid solar cells using a porphyrin dye," *Chem. Commun.*, vol. 47, p. 8244, Jan 2011. (Cited on page 11.)

[56] C. Kwong, A. Djurišić, P. Chui, K. Cheng, and W. Chan, "Influence of solvent on film

morphology and device performance of poly(3-hexylthiophene):tio$_2$ nanocomposite solar cells," *Chemical Physics Letters*, vol. 384, no. 4–6, pp. 372–375, 2004. (Cited on pages 11 and 59.)

[57] D. Frenkel and B. Smith, *Understanding Molecular Simulation*. Academic Press, 2001. (Cited on pages 12 and 71.)

[58] M. P. Allen and D. J. Tildesley, *Computer Simulation of Liquids*. Clarendon Press, Oxford, 1988. (Cited on pages 12, 71, and 78.)

[59] A. R. Leach, *Molecular Modelling: Principles and Applications*. Prentice Hall, 2001. (Cited on pages 12 and 71.)

[60] J. W. Ponder and D. A. Case, "Force fields for protein simulations," vol. 66, pp. 27–85, 2003. (Cited on pages 12, 75, 76, and 78.)

[61] D. Raymand, A. C. van Duin, M. Baudin, and K. Hermansson, "A reactive force field (reaxff) for zinc oxide," *Surface Science*, vol. 602, no. 5, pp. 1020 – 1031, 2008. (Cited on pages 12 and 13.)

[62] R. A. Buckingham, "The classical equation of state of gaseous helium, neon and argon," *Proceedings of the Royal Society of London. Series A, Mathematical and Physical Sciences*, vol. 168, no. 933, pp. pp. 264–283, 1938. (Cited on pages 12 and 77.)

[63] D. J. Binks and R. W. Grimes, "Incorporation of monovalent ions in zno and their influence on varistor degradation," *Journal of the American Ceramic Society*, vol. 76, no. 9, pp. 2370–2372, 1993. (Cited on page 12.)

[64] A. A. Sokol, S. T. Bromley, S. A. French, C. R. A. Catlow, and P. Sherwood, "Hybrid qm/mm embedding approach for the treatment of states in ionic materials," *International Journal of Quantum Chemistry*, vol. 99, no. 5, pp. 695–712, 2004. (Cited on page 12.)

[65] B. G. Dick and A. W. Overhauser, "Theory of the dielectric constants of alkali halide crystals," *Phys. Rev.*, vol. 112, pp. 90–103, Oct 1958. (Cited on page 12.)

[66] M. Kubo, Y. Oumi, H. Takaba, A. Chatterjee, A. Miyamoto, M. Kawasaki, M. Yoshimoto, and H. Koinuma, "Homoepitaxial growth mechanism of zno(0001): Molecular-dynamics simulations," *Phys. Rev. B*, vol. 61, pp. 16187–16192, Jun 2000. (Cited on page 12.)

[67] P. Erhart, N. Juslin, O. Goy, K. Nordlund, R. Müller, and K. Albe, "Analytic bond-order potential for atomistic simulations of zinc oxide," *Journal of Physics: Condensed Matter*, vol. 18, no. 29, p. 6585, 2006. (Cited on page 12.)

[68] A. C. T. van Duin, S. Dasgupta, F. Lorant, and W. A. Goddard, "Reaxff: A reactive force field for hydrocarbons," *The Journal of Physical Chemistry A*, vol. 105, no. 41, pp. 9396–9409, 2001. (Cited on page 13.)

[69] A. C. T. van Duin, A. Strachan, S. Stewman, Q. Zhang, X. Xu, and W. A. Goddard, "Reaxffsio reactive force field for silicon and silicon oxide systems," *The Journal of Physical Chemistry A*, vol. 107, no. 19, pp. 3803–3811, 2003. (Cited on page 13.)

[70] A. J. Kulkarni, M. Zhou, and F. J. Ke, "Orientation and size dependence of the elastic properties of zinc oxide nanobelts," *Nanotechnology*, vol. 16, no. 12, p. 2749, 2005. (Cited on pages 13, 31, 77, and 78.)

[71] A. J. Kulkarni, M. Zhou, K. Sarasamak, and S. Limpijumnong, "Novel phase transformation in zno nanowires under tensile loading," *Phys. Rev. Lett.*, vol. 97, p. 105502, Sep 2006. (Cited on page 13.)

[72] W. Kohn and L. J. Sham, "Self-consistent equations including exchange and correlation effects," *Phys. Rev.*, vol. 140, pp. A1133–A1138, Nov 1965. (Cited on page 13.)

[73] J. P. Perdew, J. A. Chevary, S. H. Vosko, K. A. Jackson, M. R. Pederson, D. J. Singh, and C. Fiolhais, "Atoms, molecules, solids, and surfaces: Applications of the generalized gradient approximation for exchange and correlation," *Phys. Rev. B*, vol. 46, pp. 6671–6687, Sep 1992. (Cited on page 13.)

[74] J. P. Perdew, "Density functional theory and the band gap problem," *International Journal of Quantum Chemistry*, vol. 28, no. S19, pp. 497–523, 1985. (Cited on page 13.)

[75] V. I. Anisimov, J. Zaanen, and O. K. Andersen, "Band theory and mott insulators: Hubbard *U* instead of stoner *I*," *Phys. Rev. B*, vol. 44, pp. 943–954, Jul 1991. (Cited on page 13.)

[76] V. I. Anisimov, I. V. Solovyev, M. A. Korotin, M. T. Czyżyk, and G. A. Sawatzky, "Density-functional theory and nio photoemission spectra," *Phys. Rev. B*, vol. 48, pp. 16929–16934, Dec 1993. (Cited on page 13.)

[77] A. D. Becke, "Density-functional exchange-energy approximation with correct asymptotic behavior," *Phys. Rev. A*, vol. 38, pp. 3098–3100, Sep 1988. (Cited on page 13.)

[78] C. Lee, W. Yang, and R. G. Parr, "Development of the colle-salvetti correlation-energy formula into a functional of the electron density," *Phys. Rev. B*, vol. 37, pp. 785–789, Jan 1988. (Cited on page 13.)

[79] A. Marrocchi, D. Lanari, A. Facchetti, and L. Vaccaro, "Poly(3-hexylthiophene): synthetic methodologies and properties in bulk heterojunction solar cells," *Energy Environ. Sci.*, vol. 5, pp. 8457–8474, 2012. (Cited on page 15.)

[80] T. J. Prosa, M. J. Winokur, J. Moulton, P. Smith, and A. J. Heeger, "X-ray structural studies of poly(3-alkylthiophenes): an example of an inverse comb," *Macromolecules*, vol. 25, no. 17, pp. 4364–4372, 1992. (Cited on pages 15 and 20.)

[81] S. V. Meille, V. Romita, T. Caronna, A. J. Lovinger, M. Catellani, and L. Belobrzeckaja, "Influence of molecular weight and regioregularity on the polymorphic behavior of poly(3-decylthiophenes)," *Macromolecules*, vol. 30, no. 25, pp. 7898–7905, 1997. (Cited on page 15.)

[82] K. Zhao, L. Xue, J. Liu, X. Gao, S. Wu, Y. Han, and Y. Geng, "A new method to improve poly(3-hexyl thiophene) (p3ht) crystalline behavior: Decreasing chains entanglement to promote orderâĹŠdisorder transformation in solution," *Langmuir*, vol. 26, no. 1, pp. 471–477, 2010. (Cited on pages 15 and 33.)

[83] S. Dag and L.-W. Wang, "Packing structure of poly(3-hexylthiophene) crystal: Ab initio and molecular dynamics studies," *The Journal of Physical Chemistry B*, vol. 114, no. 18, pp. 5997–6000, 2010. (Cited on page 16.)

[84] S.Tsuzuki, K. Honda, and R. Azumi, "Model chemistry calculations of thiophene dimer interactions: Origin of $\pi$-stacking," *J. Am. Chem. Soc.*, vol. 124, pp. 12200–12209, 2002. (Cited on page 16.)

[85] M. D. Graef and M. E. McHenry, *Structure of Materials: An Introduction to Crystallography, Diffraction and Symmetry*. Cambridge University Press, 2012. (Cited on page 21.)

[86] W. Cai, X. Gong, and Y. Cao, "Polymer solar cells: Recent development and possible routes for improvement in the performance," *Solar Energy Materials and Solar Cells*, vol. 94, no. 2, pp. 114–127, 2010. (Cited on page 29.)

[87] Z. L. Wang, "Zinc oxide nanostructures: growth, properties and applications," *Journal of Physics: Condensed Matter*, vol. 16, no. 25, p. R829, 2004. (Cited on page 30.)

[88] A. J. Said, G. Poize, C. Martini, D. Ferry, W. Marine, S. Giorgio, F. Fages, J. Hocq, J. Bouclé, J. Nelson, J. R. Durrant, and J. Ackermann, "Hybrid bulk heterojunction solar cells based on p3ht and porphyrin-modified zno nanorods," *The Journal of Physical Chemistry C*, vol. 114, no. 25, pp. 11273–11278, 2010. (Cited on page 30.)

[89] S. Dag and L.-W. Wang, "Modeling of nanoscale morphology of regioregular poly(3-hexylthiophene) on

a zno $(10\bar{1}0)$ surface," *Nano Letters*, vol. 8, no. 12, pp. 4185–4190, 2008. (Cited on page 33.)

[90] R. A. Marcus, "Electron transfer reactions in chemistry. theory and experiment," *Rev. Mod. Phys.*, vol. 65, pp. 599–610, 1993. (Cited on page 42.)

[91] V. Rühle, J. Kirkpatrick, and D. Andrienko, "A multiscale description of charge transport in conjugated oligomers," *The Journal of Chemical Physics*, vol. 132, no. 13, p. 134103, 2010. (Cited on page 42.)

[92] Y.-K. Lan, C. H. Yang, and H.-C. Yang, "Theoretical investigations of electronic structure and charge transport properties in polythiophene-based organic field-effect transistors," *Polymer International*, vol. 59, no. 1, pp. 16–21, 2010. (Cited on page 43.)

[93] S. A. McClure, J. M. Buriak, and G. A. DiLabio, "Transport properties of thiophenes: Insights from density-functional theory modeling using dispersion-correcting potentials," *The Journal of Physical Chemistry C*, vol. 114, no. 24, pp. 10952–10961, 2010. (Cited on pages 43 and 79.)

[94] C. Melis, P. Raiteri, L. Colombo, and A. Mattoni, "Self-assembling of zinc phthalocyanines on zno $(10\bar{1}0)$ surface through multiple time scales," *ACS Nano*, vol. 5, no. 12, pp. 9639–9647, 2011. (Cited on pages 47, 49, and 50.)

[95] C. Ingrosso, A. Petrella, P. Cosma, M. L. Curri, M. Striccoli, and A. Agostiano, "Hybrid junctions of zinc(ii) and magnesium(ii) phthalocyanine with wide-band-gap semiconductor nano-oxides: Spectroscopic and photoelectrochemical characterization," *The Journal of Physical Chemistry B*, vol. 110, no. 48, pp. 24424–24432, 2006. (Cited on page 49.)

[96] C. Ingrosso, A. Petrella, M. Curri, M. Striccoli, P. Cosma, P. Cozzoli, and A. Agostiano, "Photoelectrochemical properties of hybrid junctions based on zinc phthalocyanine and semiconducting colloidal nanocrystals," *Electrochimica Acta*, vol. 51, no. 24, pp. 5120 – 5124, 2006. (Cited on page 49.)

[97] X.-F. Zhang, Q. Xi, and J. Zhao, "Fluorescent and triplet state photoactive j-type phthalocyanine nano assemblies: controlled formation and photosensitizing properties," *J. Mater. Chem.*, vol. 20, pp. 6726–6733, 2010. (Cited on pages 49 and 50.)

[98] G. Mattioli, M. I. Saba, P. Alippi, F. Filippone, P. Giannozzi, G. Malloci, C. Melis, A. A. Bonapasta, and A. Mattoni, "Double-interface architecture for panchromatic hybrid photovoltaics," *Submitted for publication*, 2013. (Cited on page 53.)

[99] G. Mattioli, C. Melis, G. Malloci, F. Filippone, P. Alippi, P. Giannozzi, A. Mattoni, and A. Amore Bonapasta, "Zinc oxide-zinc phthalocyanine interface for hybrid solar cells," *J. Phys. Chem. C*, vol. 116, no. 29, pp. 15439–15448, 2012. (Cited on pages 53 and 57.)

[100] G. Mattioli, F. Filippone, P. Alippi, P. Giannozzi, and A. A. Bonapasta, "A hybrid zinc phthalocyanine/zinc oxide system for photovoltaic devices: a dft and tddfpt theoretical investigation," *J. Mater. Chem.*, vol. 22, pp. 440–446, 2012. (Cited on pages 53 and 54.)

[101] I. Frank, J. Hutter, D. Marx, and M. Parrinello, "Molecular dynamics in low-spin excited states," *The Journal of Chemical Physics*, vol. 108, no. 10, pp. 4060–4069, 1998. (Cited on page 53.)

[102] L. Edwards and M. Gouterman, "Porphyrins. XV. Vapor Absorption Spectra and Stability: Phthalocyanines," *J. Mol. Spectr.*, vol. 33, pp. 292–310, 1970. (Cited on page 57.)

[103] R. McCullough and P. Ewbank, *Handbook of Conducting Polymers*. Marcel Dekker, New York, 1998. (Cited on page 57.)

[104] G. R. Strobl, *The Physics of Polymers: Concepts for Understanding Their Structures and Behavior*. Springer Verlag, 2007. (Cited on page 59.)

[105] D. T. Bowron, J. L. Finney, and A. K. Soper, "The structure of liquid tetrahydrofuran," *Journal of the*

*American Chemical Society*, vol. 128, no. 15, pp. 5119–5126, 2006. (Cited on page 60.)

[106] S. Girard and F. Müller-Plathe, "Molecular dynamics simulation of liquid tetrahydrofuran: on the uniqueness of force fields," *Molecular Physics*, vol. 101, no. 6, pp. 779–787, 2003. (Cited on pages 60 and 63.)

[107] P. Giannozzi, S. Baroni, N. Bonini, M. Calandra, R. Car, C. Cavazzoni, D. Ceresoli, G. L. Chiarotti, M. Cococcioni, I. Dabo, A. D. Corso, S. de Gironcoli, S. Fabris, G. Fratesi, R. Gebauer, U. Gerstmann, C. Gougoussis, A. Kokalj, M. Lazzeri, L. Martin-Samos, N. Marzari, F. Mauri, R. Mazzarello, S. Paolini, A. Pasquarello, L. Paulatto, C. Sbraccia, S. Scandolo, G. Sclauzero, A. P. Seitsonen, A. Smogunov, P. Umari, and R. M. Wentzcovitch, "Quantum espresso: a modular and open-source software project for quantum simulations of materials," *Journal of Physics: Condensed Matter*, vol. 21, no. 39, pp. 395502–395521, 2009. (Cited on pages 62, 79, and 80.)

[108] S. Grimme, "Semiempirical gga-type density functional constructed with a long-range dispersion correction," *Journal of Computational Chemistry*, vol. 27, no. 15, pp. 1787–1799, 2006. (Cited on pages 63, 79, and 80.)

[109] Y. Marcus, *The Properties of Solvents*. Chichester: Wiley, 1998. (Cited on page 63.)

[110] A. K. Doerr, M. Tolan, J.-P. Schlomka, and W. Press, "Evidence for density anomalies of liquids at the solid/liquid interface," *Europhys. Lett.*, vol. 52, no. 3, pp. 330–336, 2000. (Cited on pages 64 and 65.)

[111] C. Pan, G. Ouyang, J. Lin, Y. Rao, X. Zhen, G. Lu, and Z. Huang, "Excess molar volumes and surface tensions of 1,2,4-trimethylbenzene and 1,3,5-trimethylbenzene with 1-butanol, 2-methyl-1-propanol, 2-butanol, and 2-methyl-2-propanol at 298.15 k," *Journal of Chemical & Engineering Data*, vol. 49, no. 6, pp. 1744–1747, 2004. (Cited on page 67.)

[112] J. Li, "Basic molecular dynamics," in *Handbook of Materials Modeling* (S. Yip, ed.), pp. 565–588, Springer Netherlands, 2005. (Cited on page 71.)

[113] M. Born and R. Oppenheimer, "Zur quantentheorie der molekeln," *Annalen der Physik*, vol. 389, no. 20, pp. 457–484, 1927. (Cited on page 71.)

[114] L. Verlet, "Computer experiments on classical fluids. i. thermodynamical properties of lennard-jones molecules," *Phys. Rev.*, vol. 159, pp. 98–103, Jul 1967. (Cited on page 71.)

[115] W. C. Swope, H. C. Andersen, P. H. Berens, and K. R. Wilson, "A computer simulation method for the calculation of equilibrium constants for the formation of physical clusters of molecules: Application to small water clusters," *The Journal of Chemical Physics*, vol. 76, no. 1, pp. 637–649, 1982. (Cited on pages 72 and 78.)

[116] H. J. C. Berendsen, J. P. M. Postma, W. F. van Gunsteren, A. DiNola, and J. R. Haak, "Molecular dynamics with coupling to an external bath," *The Journal of Chemical Physics*, vol. 81, no. 8, pp. 3684–3690, 1984. (Cited on page 74.)

[117] S. Nosé, "A unified formulation of the constant temperature molecular dynamics methods," *The Journal of Chemical Physics*, vol. 81, no. 1, pp. 511–519, 1984. (Cited on pages 75 and 78.)

[118] W. G. Hoover, "Canonical dynamics: Equilibrium phase-space distributions," *Phys. Rev. A*, vol. 31, pp. 1695–1697, Mar 1985. (Cited on pages 75 and 78.)

[119] B. R. Brooks, C. L. Brooks, A. D. Mackerell, L. Nilsson, R. J. Petrella, B. Roux, Y. Won, G. Archontis, C. Bartels, S. Boresch, A. Caflisch, L. Caves, Q. Cui, A. R. Dinner, M. Feig, S. Fischer, J. Gao, M. Hodoscek, W. Im, K. Kuczera, T. Lazaridis, J. Ma, V. Ovchinnikov, E. Paci, R. W. Pastor, C. B. Post, J. Z. Pu, M. Schaefer, B. Tidor, R. M. Venable, H. L. Woodcock, X. Wu, W. Yang, D. M. York, and M. Karplus, "Charmm: The biomolecular simulation program,"

*Journal of Computational Chemistry*, vol. 30, no. 10, pp. 1545–1614, 2009. (Cited on page 75.)

[120] N. Schmid, A. Eichenberger, A. Choutko, S. Riniker, M. Winger, A. Mark, and W. Gunsteren, "Definition and testing of the gromos force-field versions 54a7 and 54b7," *European Biophysics Journal*, vol. 40, pp. 843–856, 2011. (Cited on page 75.)

[121] J. E. Jones, "On the determination of molecular fields. ii. from the equation of state of a gas," *Proceedings of the Royal Society of London. Series A*, vol. 106, no. 738, pp. 463–477, 1924. (Cited on page 77.)

[122] U. Essmann, L. Perera, M. L. Berkowitz, T. Darden, H. Lee, and L. G. Pedersen, "A smooth particle mesh ewald method," *The Journal of Chemical Physics*, vol. 103, no. 19, pp. 8577–8593, 1995. (Cited on pages 77 and 78.)

[123] I. T. Todorov, W. Smith, K. Trachenko, and M. T. Dove, "Dl_poly_3: new dimensions in molecular dynamics simulations via massive parallelism," *J. Mater. Chem.*, vol. 16, pp. 1911–1918, 2006. (Cited on page 78.)

[124] S. Plimpton, "Fast parallel algorithms for short-range molecular dynamics," *Journal of Computational Physics*, vol. 117, no. 1, pp. 1–19, 1995. (Cited on page 78.)

[125] W. Humphrey, A. Dalke, and K. Schulten, "VMD – Visual Molecular Dynamics," *Journal of Molecular Graphics*, vol. 14, pp. 33–38, 1996. (Cited on page 78.)

[126] M. R. Hestenes and E. Stiefel, "Methods of Conjugate Gradients for Solving Linear Systems," *Journal of Research of the National Bureau of Standards*, vol. 49, pp. 409–436, Dec. 1952. (Cited on page 78.)

[127] M. Matsui and M. Akaogi, "Molecular dynamics simulation of the structural and physical properties of the four polymorphs of tio2," *Molecular Simulation*, vol. 6, no. 4-6, pp. 239–244, 1991. (Cited on page 78.)

[128] A. Jakalian, B. L. Bush, D. B. Jack, and C. I. Bayly, "Fast, efficient generation of high-quality atomic charges. am1-bcc model: I. method," *Journal of Computational Chemistry*, vol. 21, no. 2, pp. 132–146, 2000. (Cited on page 78.)

[129] J. P. Perdew, K. Burke, and M. Ernzerhof, "Generalized gradient approximation made simple," *Phys. Rev. Lett.*, vol. 77, pp. 3865–3868, Oct 1996. (Cited on pages 79 and 80.)

[130] CPMD V3.9 Copyright IBM Corp 1990-2001, Copyright MPI für Festkörperforshung Stuttgart 1997-2001. (Cited on page 79.)

[131] D. Vanderbilt, "Soft self-consistent pseudopotentials in a generalized eigenvalue formalism," *Phys. Rev. B*, vol. 41, pp. 7892–7895, 1990. (Cited on page 79.)

[132] M. Dion, H. Rydberg, E. Schröder, D. C. Langreth, and B. I. Lundqvist, "Van der waals density functional for general geometries," *Phys. Rev. Lett.*, vol. 92, p. 246401, 2004. (Cited on page 79.)

[133] G. Roman-Perez and J. M. Soler, "Efficient implementation of a van der waals density functional: Application to double-wall carbon nanotubes," *Phys. Rev. Lett.*, vol. 103, p. 096102, 2009. (Cited on page 79.)

[134] V. I. Anisimov, F. Aryasetiawan, and A. I. Liechtenstein, "First-principles calculations of the electronic structure and spectra of strongly correlated systems: the lda+ u method," *J. Phys.: Condens. Matter*, vol. 9, pp. 767–808, 1997. (Cited on page 79.)

[135] M. Cococcioni and S. de Gironcoli, "Linear response approach to the calculation of the effective interaction parameters in the LDA+U method," *Phys. Rev. B*, vol. 71, p. 035105, 2005. (Cited on page 79.)

[136] D. Rocca, D. Lu, and G. Galli, "Ab initio calculations of optical absorption spectra: Solution of the Bethe-Salpeter equation within density matrix perturbation theory," *J. Chem. Phys.*, vol. 133, p. 164109, 2010. (Cited on page 79.)

[137] O. B. Malcioglu, R. Gebauer, D. Rocca, and S. Baroni, "turbotddft - a code for the simulation of molecular spectra using the liouville-lanczos approach to time-dependent density-functional perturbation theory," *Comput. Phys. Commun.*, vol. 182, pp. 1744–1754, 2011. (Cited on page 79.)

## COLOPHON

This document was typeset using the typographical look-and-feel classicthesis developed by André Miede. The style was inspired by Robert Bringhurst's seminal book on typography *"The Elements of Typographic Style"*. classicthesis is available for both LaTeX and :

http://code.google.com/p/classicthesis/

Happy users of classicthesis usually send a real postcard to the author, a collection of postcards received so far is featured here:

http://postcards.miede.de/